UNIVERSITY OF CALIFORNIA SAN DIEGO

Investigation of Reactive Oxides and Radical Dynamics by Photoelectron-Photofragment Coincidence Spectroscopy

A dissertation submitted in partial satisfaction of the requirements for the degree Doctor of Philosophy

in

Chemistry

by

Katharine G. Lunny

Committee in charge:

Professor Robert E. Continetti, Chair
Professor Olivia A. Graeve
Professor Thomas Hermann
Professor Kimberly A. Prather
Professor Amitabha Sinha

2019

The Dissertation of Katharine G. Lunny is approved and it is acceptable in quality and form for publication on microfilm and electronically:

_____

_____

_____

_____

_____

Chair

University of California San Diego

2019

DEDICATION

To my parents, and my sister

TABLE OF CONTENTS

LIST OF FIGURES

LIST OF TABLES

ACKNOWLEDGEMENTS

There have been so many people over the years that have helped and supported me throughout my graduate career. My advisor, Bob Continetti, has been a steadfast source of guidance and I appreciate everything that he has done for me. He has pushed me to grow as a scientist, and while I often made faces, I know that he has always done what is best for me. I need to thank the entire Continetti lab over my years in grad school. Without their support, I wouldn't be where I am today. Amelia Ray, Rico Otto, Brian Adamson, Michelle Mezher, Katherine Nadler and Ashley Shin were all amazing resources and were always willing to lend help or advice. Morgan Miller and I have spent many years together, and I appreciate his friendship, as well as his help with computers. Austin Parsons, Eleanor Castracane and Pyeongeun Kim are all fun additions to the lab, and I wish them success in the coming years.

I appreciate all of the advice that Jemma Gibbard has given me over our time together. Her ability to answer questions on a project she isn't directly involved in has been invaluable and our road trip with Yanice Benitez is one of my favorite memories. I'm glad we didn't become Death Valley victims. Ben B. Shen taught me so much during our time together. I'll always appreciate how easy it was to make him laugh, and how willing he was to get fish tacos on Tuesdays. Other than the machine, the real constant throughout my time in grad school has been Yanice Benitez. Her patient demeanor and friendship over the years has always kept me grounded. I'd also like to thank our project scientist Joseph Taulane, for always having a quick smile, and often a box of doughnuts.

I also need to thank all of the collaborators I've worked with over the past few years. Yishai Albeck has always been great for pushing me to defend my results, and I am

a better scientist for it. Daniel Strasser has always been an excellent resource for advice and feedback. I appreciate the calculations that John Stanton has done, and his quick responses to emails. I'd also like to thank Carmen Alfaro for being a great asset when I need administrative help and everyone in the machine shop, particularly Bob, who was always ready to help with emergencies and jokes to ease stressful visits. I'd also like to thank Mike Godkin from Clark-MXR for his patience with our laser questions, as well as his ability to fix the laser for us twice. I also need to thank all of the professors throughout my career for their support and guidance, including my committee, as well as all of my chemistry professors from Saint Anselm College. Most notably, I'd like to thank my undergrad advisor, Dr. Nicole Eyet. Her continued support and mentorship have helped me immensely throughout my time in grad school.

I need to thank all of my friends that I've made throughout my time in grad school who have helped to keep me sane. Pragya Sidhwani has been an amazing roommate over the last five years, and our nacho nights with Ryan Lannan, Yanice Benitez and Peanut have always been filled with laughter. I've enjoyed not watching Harry Potter movies together over the years. Kevin Cao has always been a source of advice and fun. I look forward to trying to secretly pick up the bill when we're together in Berkeley. I can't thank Sophia de Alba and Xavi enough for being a great reminder of life outside of grad school, and I've enjoyed the excessive sushi we've eaten together. Linhan Shen has always been a source of adventure, and the trips we've gone on have been some of my favorite California memories.

I need to thank my close friends for continuing to put up with me throughout my time in grad school. My phone calls with Caitlyn Jarvis always made me laugh and

remember that our long distance friendship is truly the envy of everyone. Emily Kent has always been steadfast in her support even if she doesn't understand any of the science I'm doing. I appreciate her constant messages, and her jokes always remind me to not take life too seriously. Staci Herman continued to be my hype man, and I'm so glad that we've been able to commiserate about grad school together, even if we're at different schools. I will never be able to thank John Pham enough for everything he has done for me over the past few years. From the late night food drop offs while I was collecting data, to just sitting beside me encouraging me while I write, I couldn't ask for a better supporter. I'm sure he has learned far more about physical chemistry (but mostly C_2O_2) than he ever wanted to.

Finally, I need to thank my family. My parents have truly been my number one supporters throughout this entire experience. Our 3:30 pm phone calls became well known in the lab, and I always appreciated being able to take a walk in the sunshine and remember that life was more than just what was going on in lab that day. Thank you for everything you have done for me so that I could get to this point. I also can't express the gratitude I feel towards my sister, Elizabeth. Thanks for letting me escape to Pasadena when I need a weekend full of food and Teen Mom. Being in grad school together, and understanding each other's issues as well as celebrating the successes has been a truly unique experience. I wouldn't want to go through it with anyone else.

Chapters three and five are adapted from the following publications, in which the dissertation author is the primary author and the dissertation advisor is the corresponding author. Lunny, K. G., Benitez, Y., Albeck, Y. Strasser, D., Stanton, J. F., Continetti, R. E.; "Spectroscopy of Ethylenedione and Ethynediolide: A Reinvestigation", *Angewandte Chemie International Edition*, 2018, 57, 5394. Albeck, Y.*, Lunny, K. G.*, Benitez, Y.,

Shin, A. J., Strasser, D., Continetti. R. E., "Resonance-Mediated Below-Threshold Delayed Photoemission and Non-Franck-Condon Photodissociation of Cold Oxyallyl Anions", *Angewandte Chemie International Edition,* 2019, 58, 5312.

Chapter four is being prepared for publication, in which the dissertation author is the primary author and the dissertation advisor is the corresponding author. Lunny, K. G., Albeck, Y., Benitez, Y., Strasser, D., Continetti. R. E., "Dissociative Photodetachment of the Oxyallyl Anion in the Near Ultraviolet via Triplet-Singlet Intersystem Crossing"

Chapter six is being prepared for publication, in which the dissertation author is the primary author and the dissertation advisor is the corresponding author. Lunny, K. G., Benitez, Y., Albeck, Y., Strasser, D., Continetti. R. E., "Photodynamics of $N_2O_2^-$ in the Near UV: Photodissociation and Autodetachment of NO^-"

Chapter seven is being prepared for publication, in which the dissertation author is the primary author and the dissertation advisor is the corresponding author. Lunny, K. G., Albeck, Y., Benitez, Y., Strasser, D., Stanton, J. F., Continetti, R. E., "Photodissociation of the Peroxynitrite Anion"

VITA

2014 Bachelor of Arts, Saint Anselm College

2014-2019 Research Assistant, University of California, San Diego

2016 Master of Science, University of California, San Diego

2019 Doctor of Philosophy, University of California, San Diego

PUBLICATIONS

Lunny, K. G., Albeck, Y., Benitez, Y., Strasser, D., Continetti. R. E., "Dissociative Photodetachment of the Oxyallyl Anion in the Near Ultraviolet via Triplet-Singlet Intersystem Crossing", *In preparation.*

Lunny, K. G., Benitez, Y., Albeck, Y., Strasser, D., Continetti. R. E., "Photodynamics of $N_2O_2^-$ in the Near UV: Photodissociation and Autodetachment of NO^-", *In preparation.*

Lunny, K. G., Albeck, Y., Benitez, Y., Strasser, D., Stanton, J. F., Continetti, R. E., "Photodissociation of the Peroxynitrite Anion", *In preparation.*

Benitez, Y.; Lu, D.; Lunny, K. G.; Li, J.; Guo, H.; Continetti, R. E.; "Photoelectron-Photofragment Coincidence Studies on the Dissociation Dynamics of the OH-CH_4 Complex", *Journal of Physical Chemistry, A.*, 2019, 123, 23, 4825; https://doi.org/10.1021/acs.jpca.9b02441

Shen, B. B.; Lunny, K. G.; Benitez, Y.; Continetti, R. E.; "Photoelectron-Photofragment Coincidence Spectroscopy with Ions Prepared in a Cryogenic Octopole Accumulation Trap: Collisional Excitation and Buffer Gas Cooling", *Frontiers in Chemistry*, 2019, 7, 295; https://doi.org/10.3389/fchem.2019.00295

Albeck, Y., Lunny, K. G., Benitez, Y., Shin, A. J., Strasser, D., Continetti. R. E., "Resonance-Mediated Below-Threshold Delayed Photoemission and Non-Franck-Condon Photodissociation of Cold Oxyallyl Anions", *Angewandte Chemie International Edition,* 2019, 58, 5312; https://doi.org/10.1002/anie.201900386

Lunny, K. G., Benitez, Y., Albeck, Y. Strasser, D., Stanton, J. F., Continetti, R. E.; "Spectroscopy of Ethylenedione and Ethynediolide: A Reinvestigation", *Angewandte Chemie International Edition,* 2018, 57, 5394; https://doi.org/10.1002/anie.201801848

Shen, B. B.; Benitez, Y.; Lunny, K. G.; Continetti, R. E.; "Internal Energy Dependence of the Photodissociation Dynamics of O_3^- Using Cryogenic Photoelectron-Photofragment Coincidence Spectroscopy", *The Journal of Chemical Physics,* 2017, 147, 094307; http://dx.doi.org/10.1063/1.4986500

ABSTRACT OF THE DISSERTATION

Investigation of Reactive Oxides and Radical Dynamics by Photoelectron-Photofragment Coincidence Spectroscopy

by

Katharine G. Lunny

Doctor of Philosophy in Chemistry

University of California San Diego, 2019

Professor Robert E. Continetti, Chair

Carbon, hydrogen, oxygen, and nitrogen are the most common elements necessary for life and in combination create a multitude of molecules. These include highly reactive species with complicated electronic structures, such as oxygenated hydrocarbon radicals and nitrogen oxides. These short-lived species can be important in atmospheric and combustion processes, but difficult to characterize due to their transient nature. Photoelectron-photofragment coincidence spectroscopy is a technique designed to study

short-lived species thought photodetachment of the corresponding stable anion and measure the energy partitioning within the neutral species.

The oxyallyl anion was photodetached to the nearly degenerate states, $^3B_2$ and $^1A_1$ as well the $^3B_1$ excited state, which were correlated to predominately stable C_3H_4O neutral. The photoelectron spectrum of the oxyallyl diradical and the acetone enolate radical, C_3H_5O, are the correct assignment for the C_2O_2 and HC_2O_2 photoelectron spectra reported in the literature. The oxyallyl diradical was observed to have a minor dissociation channel, at both $E_{h\nu}$ = 3.20 eV and 1.60 eV. At $E_{h\nu}$ = 3.20 eV, photodetachment to the $^1A_1$ state is accessible, and results in dissociation to CO + C_2H_4. Dissociation was also observed from the triplet states, occurring after intersystem crossing. This system is further complicated by the observation of dipole bound states. The $^1A_1$ state has a zwitterionic character resulting in observation of photodetachment ~0.3 eV below threshold. A stable neutral was the result of delayed photoemission during cyclization, as well as dissociative photodetachment resulting from a two photon process were observed.

The complicated electronic structure of nitrogen oxides, N_2O_2 and NO_3 exhibit photodissociation pathways due the several neutral dissociation channels accessible at $E_{h\nu}$ = 3.20 eV. For N_2O_2, photodissociation resulted in vibrationally excited NO anions which undergoes autodetachment, as well as photodissociation of NO^- (ν=0). Photodissociation was also observed to result in N_2O + O^- which undergoes sequential photodetachment. The peroxynitrite anion, a high energy isomer of the nitrate anion, was also observed to produce similar photodissociation pathways. Vibrationally excited NO^- followed by autodetachment was observed, as well as the observation of sequential photodetachment of O_2^- via a two-photon process.

Chapter 1: Introduction and Background

1.1. Background

Some of the first experiments conducted to determine the origin of life on early Earth used carbon, nitrogen, oxygen and hydrogen in the gas phase with an electrical discharge.[1, 2] This combination of atoms was observed to produce a variety of organic molecules important for life.[1, 2] Understanding how the four most common elements in the universe interact to form molecules gives insight into not only the early chemistry of Earth, but how these molecules could form and create life in other parts of the universe.[3] The variety of molecules that can be formed have multiple applications, some of which have significant impact on the chemistry of Earth's atmosphere.[4, 5] Many of the most basic molecules can be formed with these atoms, including water and methane, but more exotic and highly reactive species can also be formed. These include oxygenated hydrocarbon radicals, which are molecules with an unpaired electron, as well as various combinations of nitrogen oxides.

In order to understand how and why these molecules are important to greater questions, it is imperative that these systems are fully understood energetically. This includes different ways that energy can be partitioned into a system. Some common mechanisms that can be observed are the energy it takes to remove an electron, known as the electron affinity, the energy required to break bonds, known as the dissociation energy and how energy is partitioned into vibrational or rotational excitation in these systems. Each of these mechanisms can be observed using various spectroscopic techniques.

Without a complete understanding of these simple molecules, their impact on larger mechanisms can't be fully understood.

While the goal is to experimentally measure these mechanisms, very often theoretical calculations are able to give insight into the dynamics that are occurring. Potential energy surfaces are a way of representing the various degrees of freedom within a molecule and how they interact energetically. While theoretical modeling has become significantly more reliable in recent years with advances in computing power, larger systems with more degrees of freedom remain exponentially more difficult to model. The degrees of freedom within a system is defined as 3N-6 where N is the number of atoms. Theory calculations can be used to model these systems and to calculate the energetics of different mechanisms molecules can undergo, however experimental values need to exist for comparison to determine if the theoretical models are accurate. By experimentally measuring points on the potential energy surface, especially states that are more difficult to model such as transition states, theory can be guided towards approximations in order to model larger systems accurately, and in turn help to interpret experimental results. Many techniques can be used to study the different reaction dynamics that can occur for these systems, but studying intermediate states can be the most challenging, since they are inherently unstable. In order to overcome this, experiments such photoelectron spectroscopy and photodissociation spectroscopy have been created. These involve creating stable precursors that can produce the species of interest after interaction with a laser.

Photoelectron-photofragment coincidence spectroscopy is a technique that is able to measure the vertical detachment energy of an electron from a stable precursor anion as

well as the dissociation dynamics of the resulting neutral.[6] This allows for transient species to be studied, such as exotic radicals and systems with multiple dissociation pathways. The addition of a cryogenic octopole accumulation trap has allowed for a larger range of exotic anions to be created.[7] While previously, only anions that were formed in the coldest part of a supersonic expansion could be studied using PPC spectroscopy, now hotter portions of the expansion can be cooled and stabilized. This includes stabilizing less common isomers of nitrogen oxides, such as the trans N_2O_2 anion, which has not been studied as much as its C_{2v} counterpart and the peroxynitrite anion, a higher energy isomer of the D_{3h} nitrate anion. Not only can isomers of more well studied molecules be stabilized, radicals such as the oxyallyl radical anion and the acetone enolate anion that are known to exist can be created in new and unexpected preparation methods.

1.1.1. Oxygenated Hydrocarbon Radicals

Radicals are a class of molecules that have an unpaired electron. This often means that radicals are highly reactive and have very short lifetimes. Diradicals can also exist, which are intermediates with two unpaired electrons that often have complicated electronic structures.[8] In a system that is a perfect diradical, two degenerate molecular orbitals exist, however the complexity of the electronic structure can be increased by slight modifications to this degeneracy.[9] In hydrocarbon radicals, this degeneracy can be modified by the addition of oxygen, which are produced in the atmosphere through reactions of hydroxyl radicals with hydrocarbons, or reactions of carbonyls with molecular oxygen.[10, 11] Oxygenated hydrocarbon radicals have a critical role in the atmosphere, where they can undergo reactions with nitric oxide (NO) form NO_2, an oxidation that is most often seen in

the presence of ozone.[12, 13] For these systems that are highly reactive intermediates, it is fundamentally important to understand how they decompose, or isomerize.

1.1.2. Nitrogen Oxides

Nitrogen oxides are any species containing nitrogen and oxygen. These can have relevance to various mechanisms, from biological to atmospheric processes.[4, 5, 14, 15] In the atmosphere, nitrogen oxides such as NO and NO_2 are important contributors to ozone production in the troposphere.[4] Because of this, it is important to study the relative energetics of these states, as well as their vibrational and rotational excitation. In biological processes, nitrogen oxides can be toxic in some cases. Understanding the reactions that surround less common nitrogen oxides that are produced within cells are critical to understanding their roles in larger processes.[14]

1.2. Photoelectron Spectroscopy

Photoelectron spectroscopy is a technique that studies neutral surfaces that might otherwise be inaccessible, through photodetachment of a stable anion. This technique is dependent on the photoelectric effect where an electron is emitted when light is shined onto a surface.[16] In photoelectron spectroscopy, these electrons are collected, and can be characterized based on the orbital that the electron is removed from. When this technique is used in the gas phase, the different velocities of the electrons can indicate different electronic states that exist for the neutral, as well as information about vibrational excitation on the neutral surface. The intensity of vibrational transitions is based on the Franck-Condon factor for the anion and neutral surface which can be expressed as[17]:

$$q_{v'v''} = |\int \psi_{v'}\psi_{v''}\, dr\,|^2 \tag{1.1}$$

The Franck-Condon principle exists due to the Born-Oppenheimer approximation assumption that within a wavefunction, the electronic and nuclear components can be separated.[18] This results in the detachment of the electron on a significantly faster timescale (on the order of femtoseconds) than the rearrangement of geometry of the molecule. A vertical transition to the neutral surface means that the relative intensities of the vibrational excitation of the neutral will depend on the relative overlap with the anion.[19] This can result in the observation of states that are inaccessible using other forms of spectroscopy.[20]

A diagram representing a typical photoelectron spectroscopy experiment is shown in Figure 1.1. Because a stable neutral is being accessed within the Franck-Condon region, a vibrational progression is observed in the photoelectron spectrum shown. The relation between the energy partitioning in this example is:

$$eKE = E_{h\nu} - AEA - E_{vib} - E_{rot} \tag{1.2}$$

Where eKE is the electron kinetic energy, $E_{h\nu}$ is the photon energy, AEA is the adiabatic electron affinity, E_{vib} is the vibrational energy of the neutral product, while E_{rot} is the rotational excitation of the resulting neutral. This relation will also sometimes be referred to in term of electron binding energy, which is represented as:

$$eBE = E_{h\nu} - eKE \tag{1.3}$$

While photoelectron spectroscopy often is used to measure the electron affinity of a molecule, it can also give information about structure of both the anion and neutral surfaces. Using the experimental information gained from this technique, theoretical

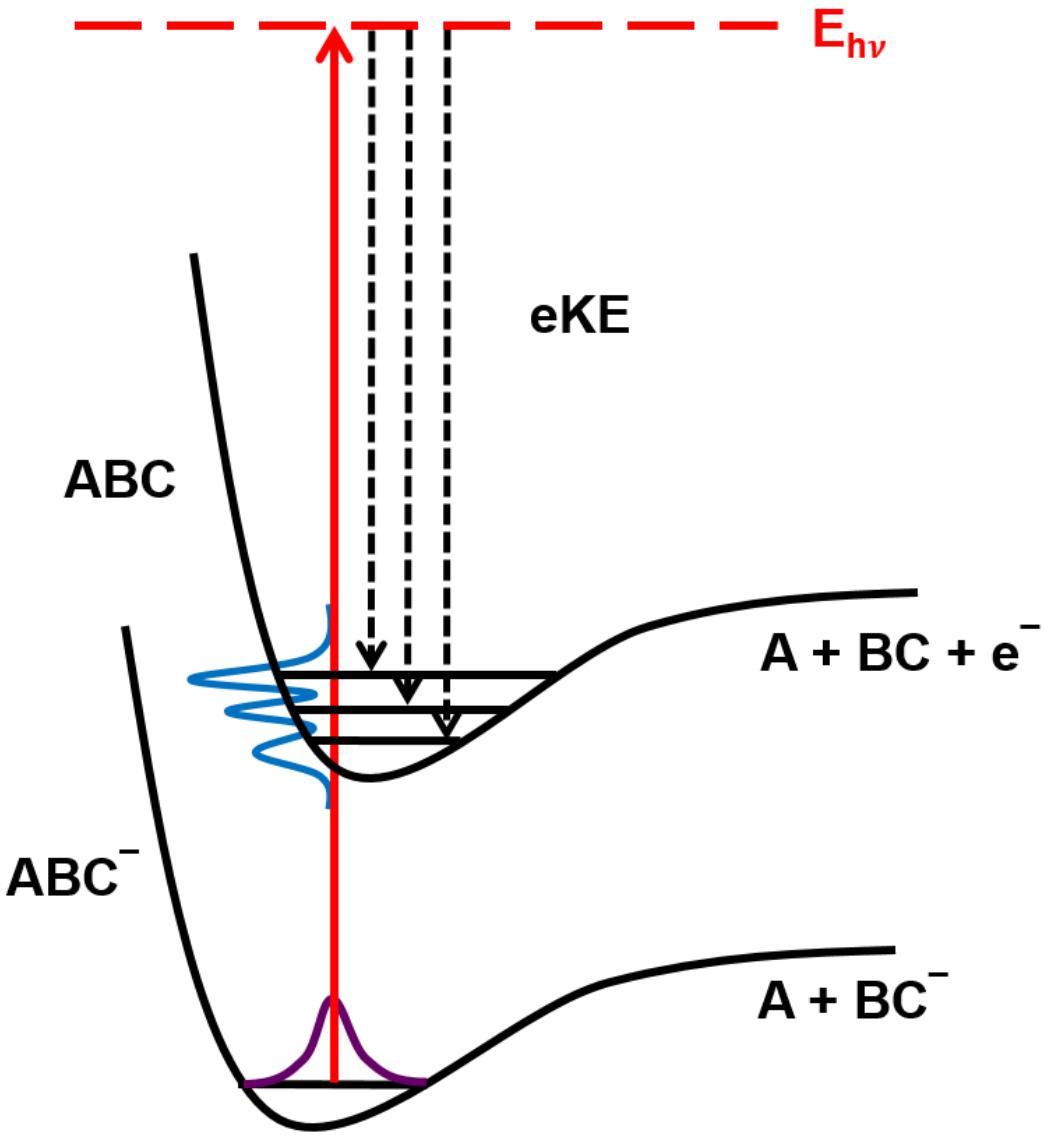

Figure 1.1. Photoelectron spectroscopy diagram. The red arrow represents a photon absorbed by the system, resulting in electrons departing with varying kinetic energies. The relative population of the vibrational states is shown by the blue trace.

models of the potential energy surfaces can be produced. This is particularly of use when utilized to study systems that are difficult to observe using other spectroscopic techniques. One example of this are radicals, which are short lived species that are highly reactive. Photoelectron spectroscopy can also give some information about the lifetimes of neutral states that are metastable, however cannot determine the dynamics of the neutral products that reults.[21, 22]

The resolution of a typical photoelectron spectroscopy experiment allows for the observation of vibrational progressions but cannot resolve rotational transitions. This has been improved over the years using velocity map imaging (VMI), as well as tunable laser systems.[23] When these two advances are combined, zero electron kinetic energy (ZEKE) spectroscopy allows for a significant improvement in resolution, but comes at the price of difficult experiments.[24-27] In order to balance the benefits of better resolution with the difficulty of experiment, slow electron velocity map imaging (SEVI) has instead been used.[24] This technique allows for a significant improvement in resolution, and insight into more nuanced dynamics such as rotational transitions with the added advantage of not being as challenging experimentally.

1.2.1 Autodetachment

One mechanism that can be observed through photoelectron spectroscopy is autodetachment, which is when it is energetically favorable for a vibrationally excited anion to spontaneously eject an electron and form a more stable neutral product.[28] This occurs in systems where the neutral and anion surface are very close energetically, so that vibrationally excited anions are less stable than the neutral. An example of this can be

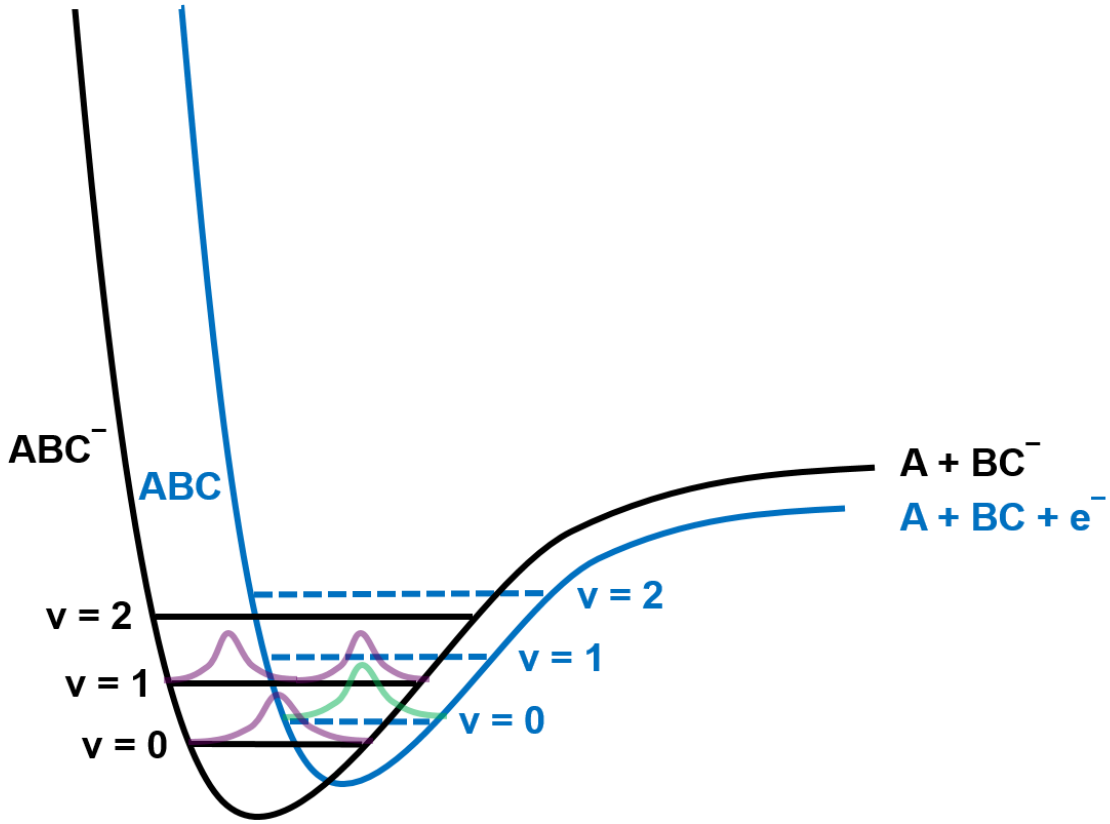

Figure 1.2. Representation of autodetachment. When a system has a small electron affinity, it can be energetically favorable to spontaneously eject an electron to reach the neutral state, rather than stay in a high vibrational state on the anion surface.

seen in Figure 1.2. When the anion is in its ground vibrational state, $\nu = 0$, the molecule is stable, but when excitation occurs to $\nu = 1$, it is energetically favorable for the anion to eject the electron. In this example, this results in neutral ground state $\nu = 0$, but can also result in other vibrational states being populated on the neutral surface, depending on the excitation on the anion surface and the spacing between the anion vibrational states in relation to the neutral vibrational states.[29] The electrons that result from this mechanism can then be observed through photoelectron spectroscopy. Autodetachment has a different relation to the photon energy than photodetachment because it is a nonadiabatic transition where the photon energy results in excitation on the anion surface, instead of a transition from the anion to the neutral surface.[30] Autodetachment can be observed in various experiments, including tunable laser autodetachment spectroscopy, elastic scattering, electron attachment, as well as photodissociation experiments that result in vibrationally excited products.[28-31]

1.3. Photofragment Translational Spectroscopy

Photodissociation spectroscopy is another technique that can be used to gain insight into the reaction dynamics of a system. While photodetachment measures electronic transitions, photodissociation spectroscopy is used measure the bond dissociation energy of a molecule. This is commonly used on both neutrals and positive ions. For negative ions, the bond dissociation energies are often higher than the energy required for photodetachment, so it is less frequently employed.[32] The exception for this includes some open shell anions with relatively small dissociation energies. An example of this can be seen in Figure 1.3. In this schematic, two scenarios are shown. In the first, the neutral surface is a repulsive curve, resulting in the kinetic energy release of two neutral fragments

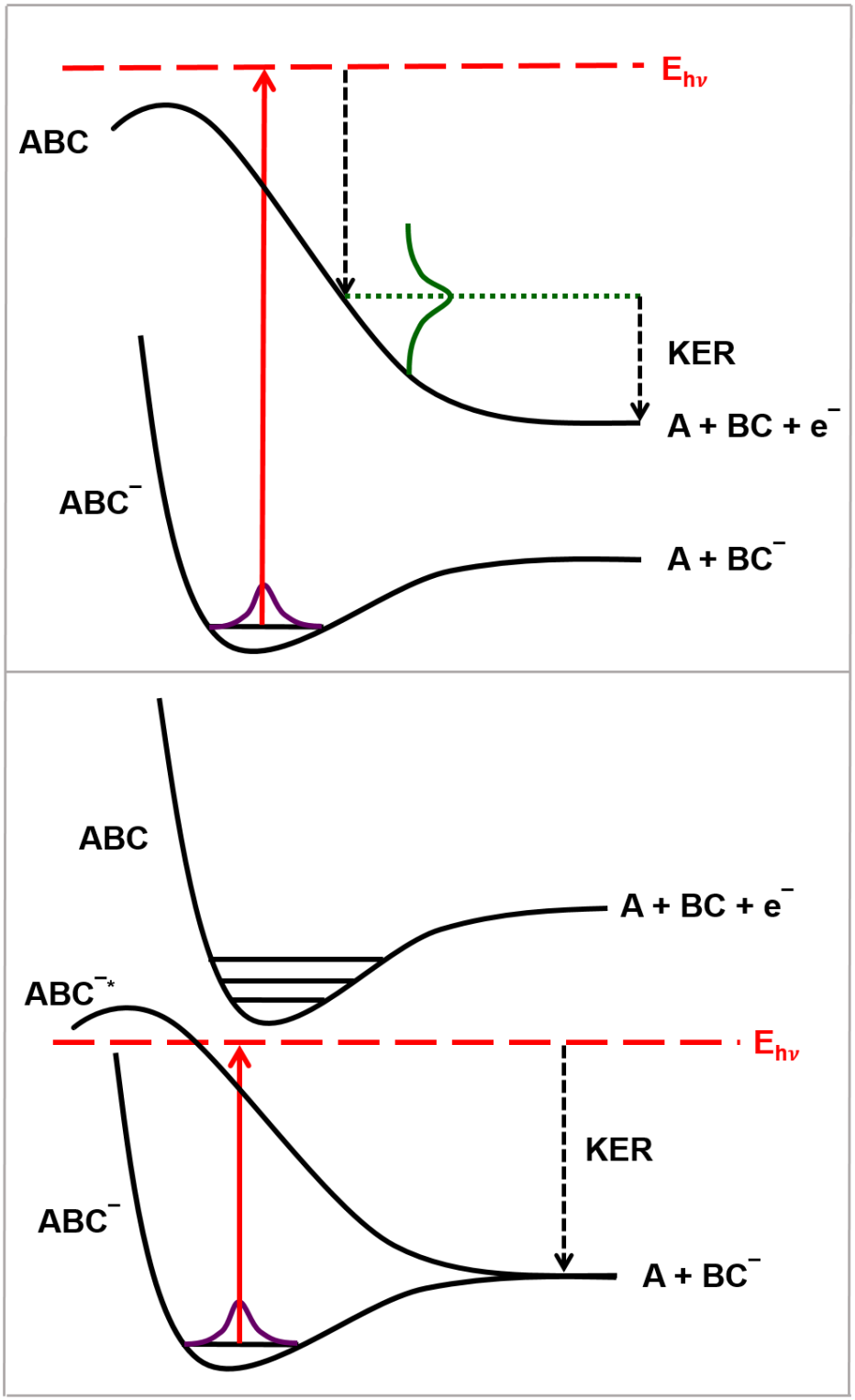

Figure 1.3. Schematic for photofragmentation. This can either be to a dissociative neutral surface, shown in the top panel, or photodissociation to the anion asymptote, shown in the lower panel.

being measured. In the second example, the neutral surface is energetically inaccessible for photodetachment to occur, but the photodissociation to the anion asymptote can be reached at the photon energy shown. In neutral systems, these products can then be measured directly, but for anions, often another process must occur so that the second fragment is neutralized.[32, 33] Neutralization of the anion fragment can occur either through autodetachment, as was discussed in 1.2.1 or sequential photodetachment via a second photon, which will be discussed in Section 1.4.3.

The most common measurement of the fragments is the velocity recoil resulting from dissociation. From this, both the kinetic energy release of the neutral as well as the product mass spectrum can be calculated. The photodissociation cross section is often also collected, but will not be discussed in detail in this thesis.[32, 34] In order to measure photodissociation, a fast beam of ions must be used. For a neutral experiment, two laser pulses are used, the first to photodetach an electron from the precursor anion and the second to induce dissociation. An anion is often used as a precursor so that it can be manipulated and accelerated prior to the photodissociation experiment. The kinetic energy release (KER) of a dissociation ABC → A + BC is given in terms of the center of mass and can be expressed as:

$$E_{CM} = \left(\frac{E_0}{l^2}\right)\left(\frac{m_A m_{BC}}{M^2}\right)[(v_0\tau)^2 + R^2] \cdot (1 + 2\frac{m_{BC} - m_A}{M} \cdot \frac{v_0\tau}{l}) \qquad (1.4)$$

In this equation, M is the parent mass, m is the mass of the respective fragments, l is the flight path from the interaction region to the detector, v_0 is the velocity, τ is the time and R is the distance between the two fragments on the detector. A schematic of this can be seen in Figure 1.4. By measuring M, l, v_0, τ and R, and assuming values of the fragments

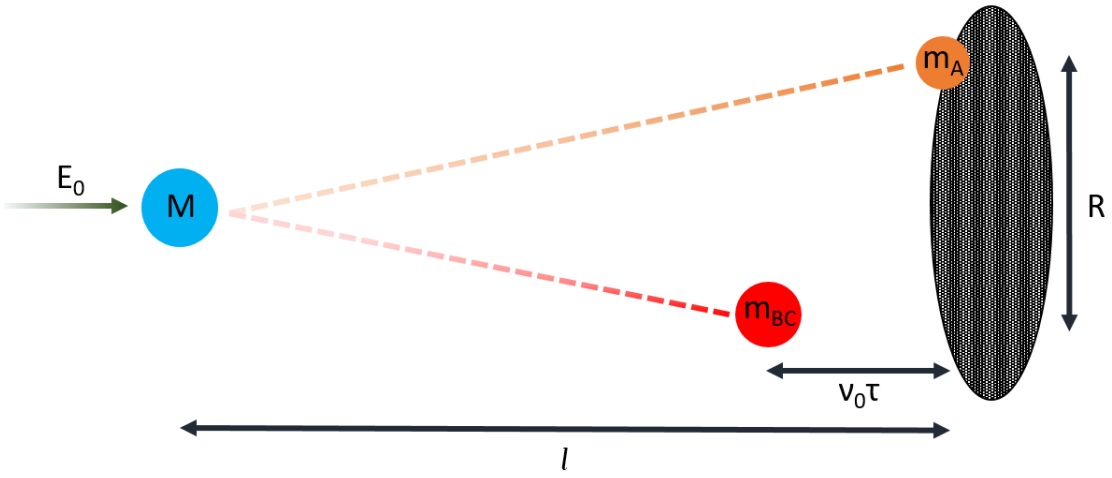

Figure 1.4. An example schematic of translational spectroscopy.

m_A/m_{BC}, the E_{CM}, or kinetic energy release can be calculated.[35] By measuring the kinetic energy release (KER), different dissociation dynamics can be observed, which can include vibrational states of the neutrals or different mass fragmentation.

1.4. Photoelectron-Photofragment Coincidence Spectroscopy

Photoelectron-photofragment coincidence spectroscopy is a technique that combines photoelectron spectroscopy with translational spectroscopy in order to give a complete understanding of the energy partitioning within a system. This requires a stable anion precursor, which can then be photodetached to the Franck-Condon region of the neutral. After photodetachment, if the neutral surface is a repulsive curve, the kinetic energy release (KER) of the resulting neutral fragments can also be measured. This technique can also confirm that a photoelectron spectrum results in a stable neutral product. This can be an especially powerful tool when previous photoelectron spectrum of a system has been measured, and the dissociation dynamics of the neutral have been theoretically calculated. By directly measuring the photofragments or photoneutrals, these calculations can either be confirmed, or challenged.

Because the electrons and the neutral fragments are measured in coincidence, each event can be correlated and give clear insight into some processes that might not otherwise be apparent. Each of these events can then be plotted in a coincidence plot, with the electron kinetic energy on one axis and the kinetic energy release on the other. Different mechanisms become apparent in coincidence plots, since each have distinct features. The three major mechanisms that were observed in this thesis are dissociative photodetachment, and photodissociation followed by either autodetachment or sequential photodetachment.

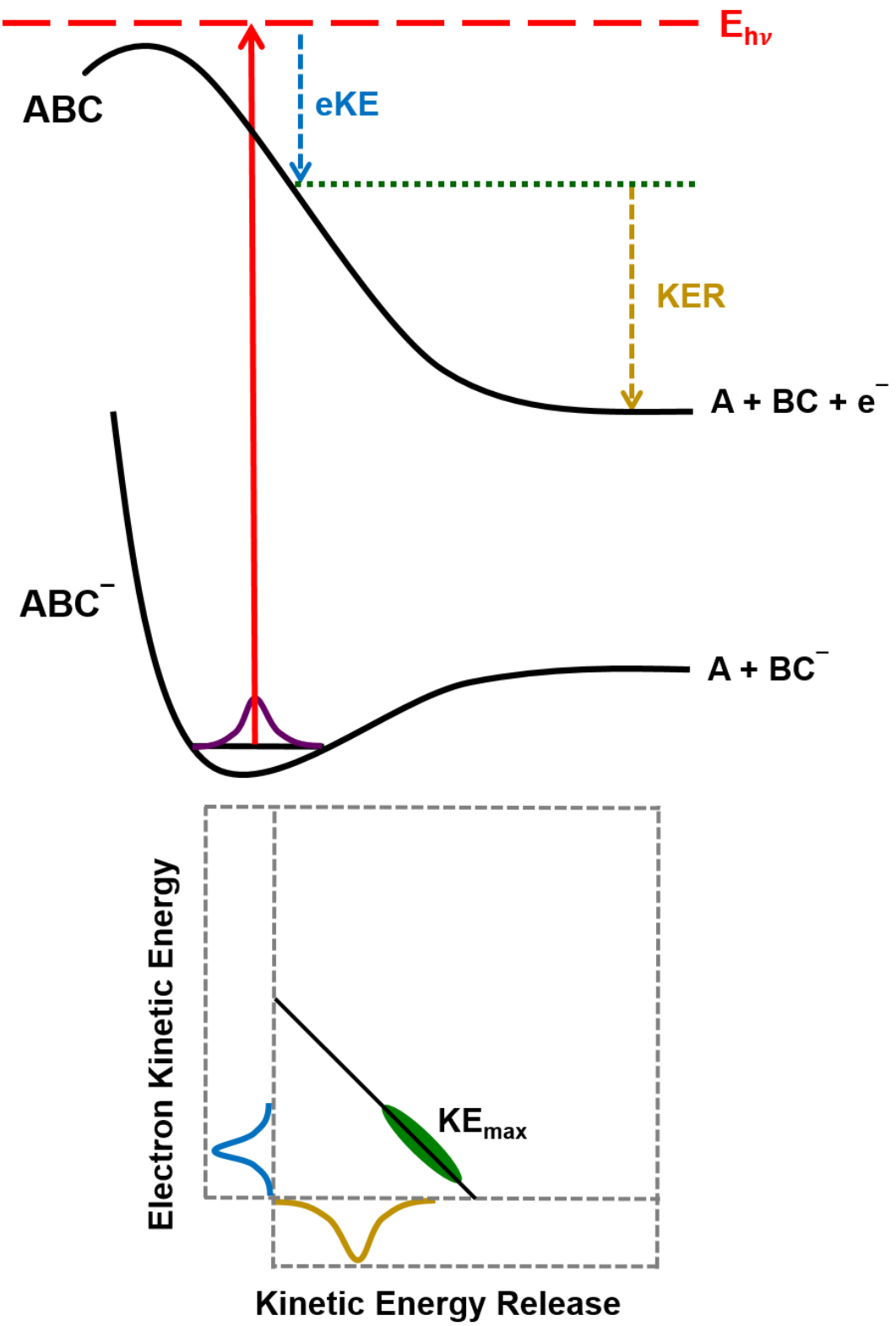

Figure 1.5. An example of dissociative photodetachment. This combines the information gained from photoelectron spectroscopy with the resulting neutral's dissociation dynamics. A coincidence plot is shown below.

Each of these has a unique signature on the coincidence plots, and will be explained in more detail below.

1.4.1. Dissociative Photodetachment

As mention, dissociative photodetachment is the process in which a stable anion is photodetached to a repulsive neutral surface. In this case, the electron kinetic energy (eKE) and the kinetic energy release (KER) can be directly correlated, and are expressed in the following equation:

$$KE_{max} = E_{h\nu} - AEA(BC^-) - \Delta D^\circ(ABC^-) \quad (1.5)$$

From a coincidence plot, an experimental kinetic energy maximum (KE_{max}) can be determined and compared to theoretical predictions. An example of dissociative photodetachment, as well as the corresponding coincidence plot can be seen in Figure 1.5. When the electron affinity of a system is known, the KE_{max} can provide insights into the dissociation energy on the anion surface. This can also be useful if the dissociation energy of the anion is known, but the electron affinity is not.

1.4.2. Photodissociation and Sequential Photodetachment

In some cases, when the neutral states are significantly higher in energy than the photon energy used, photodissociation to the anion asymptote is instead observed. This can be followed by either sequential photodetachment or autodetachment. Sequential photodetachment is observed when photodissociation results in an anion asymptote that is significantly more stable than the corresponding neutrals. When this occurs, a second photon is needed to photodetach the resulting anion state. This can occur if the timescale

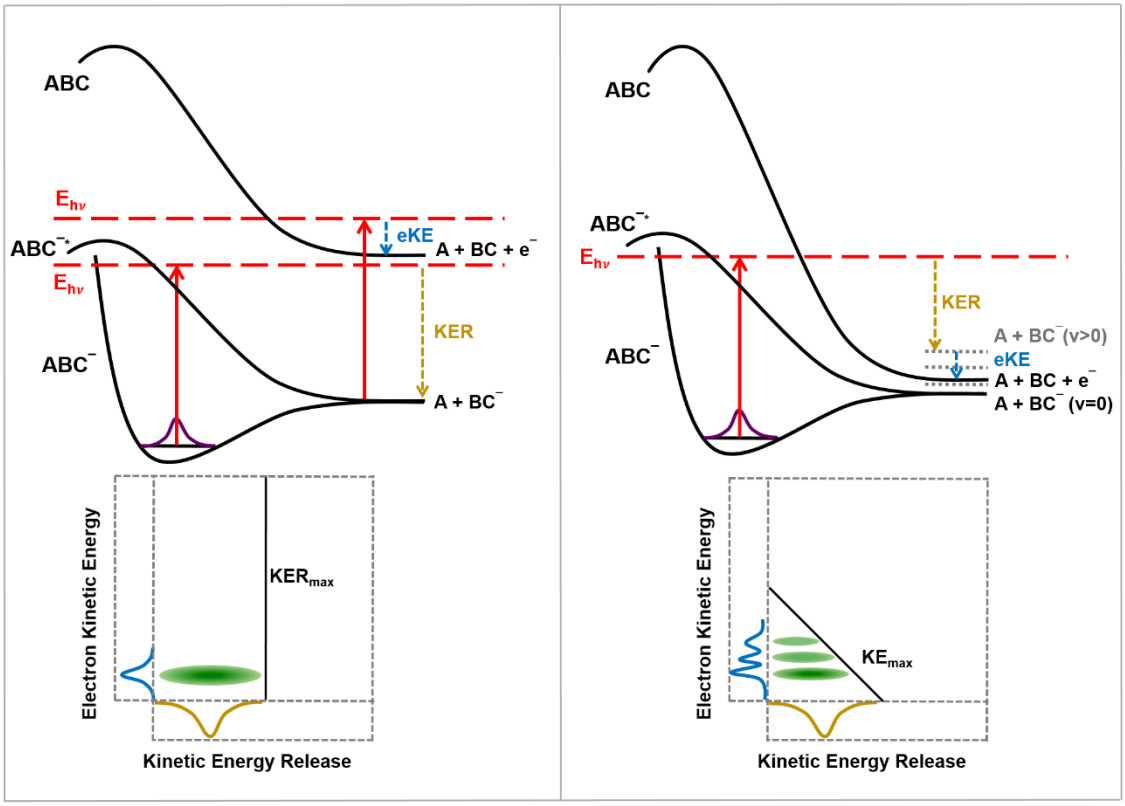

Figure 1.6. A schematic of photodissociation followed by either photodissociation, shown on the left, or autodetachment, as seen on the right. The corresponding coincidence plots can be seen below.

of the laser pulse is long enough to interact with the anion products that result from photodissociation. In this case, the kinetic energy release and electron kinetic energy measurements are decoupled, resulting in only the dissociation energy of the anion and the electron affinity of one of the anion products being measured. When this occurs, equation 1.5 is modified to be a kinetic energy release maximum (KER_{max}) since it is only a measurement of the dissociation energy of the anion. A KER_{max} is expressed as a vertical line on the coincidence plot. This mechanism can be seen in Figure 1.6 where the dissociation energy of the anion is measured by the first photon, and the second photon is only measuring the electron affinity of the BC anion. This mechanism will also be observed when the neutral state ABC cannot be accessed energetically with the photon energy used.

1.4.3. Photodissociation and Autodetachment

In the case of photodissociation followed by autodetachment, the anion states that are reached through photodissociation are unstable in relation to the neutral product states. Because photodissociation can result in a large geometry change, significant vibrational excitation can be observed in the resulting products. If these vibrational states are higher in energy than the neutral products, autodetachment will occur. An example of this mechanism can be seen in Figure 1.6 where the vibrational excitation of the anion product BC^- are energetically unstable in relation to BC neutral and result in autodetachment. Because multiple vibrational states on the anion surface can be populated, a vibrational progression can be observed in the photoelectron spectrum and corresponds to horizontal bands on the coincidence plot. The equation 1.5 still applies in this scenario, and a diagonal KE_{max} on the coincidence plot gives insight into the relative energetics of the states

accessed. When photodissociation is observed, the dissociation energy of the anion is being measured directly, instead of being inferred from the other measurements.

1.5. References

1. Miller, S. L., A Production of Amino Acids under Possible Primitive Earth Conditions. *Science* **1953,** *117* (3046), 528-529.

2. Miller, S. L.; Urey, H. C., Organic Compound Synthesis on the Primitive Earth. *Science* **1959,** *130* (3370), 245-251.

3. McKay, C. P., Urey Prize Lecture: Planetary Evolution and the Origin of Life. *Icarus* **1991,** *91*, 93-100.

4. Crutzen, P. J., The Influence of Nitrogen Oxides on the Atmospheric Ozone Content. *Quart. J. R. Met. Soc.* **1970,** *96*, 320-325.

5. Crutzen, P. J., Ozone Production Rates in an Oxygen-Hydrogen-Nitrogen Oxide Atmosphere. *J. Geophys. Res.* **1971,** *76* (30), 7311-7327.

6. Johnson, C. J.; Shen, B. B.; Poad, B. L. J.; Continetti, R. E., Photoelectron-Photofragment Coincidence Spectroscopy in a Cryogenically Cooled Linear Electrostatic Ion Beam Trap. *Rev. Sci. Instrum.* **2011,** *82*, 105105.

7. Shen, B.; Benitez, Y.; Lunny, K. G.; Continetti, R. E., Internal Energy Dependence of the Photodissociation Dynamics of O_3^- Using Cryogenic Photoelectron-Photofragment Coincidence Spectroscopy. *J. Chem. Phys.* **2017,** *147*, 094307.

8. Pedersen, S.; Herek, J. L.; Zewail, A. H., The Validity of the "Diradical" Hypothesis: Direct Femtosecond Studies of the Transition-State Structures. *Science* **1994,** *266*, 1359-1363.

9. Borden, W. T., *Diradicals*. John Wiley and Sons Inc: New York, 1982.

10. Chameides, W.; Walker, J. C. G., A Photochemical Theory of Tropospheric Ozone. *J. Geophys. Res.* **1973,** *78* (36), 8751-8761.

11. Lightfoot, P. D.; Cox, R. A.; Crowley, J. N.; Destriau, M.; Hayman, G. D.; Jenkin, M. E.; Moortgat, G. K.; Zabel, F., Organic Peroxy Radicals: Kinetics, Spectroscopy and Tropospheric Chemistry. *Atmos. Environ., Part A* **1992,** *26* (10), 1805-1961.

12. Tyndall, G. S.; Cox, R. A.; Granier, C.; Lesclaux, R.; Moortgat, G. K.; Pilling, M. J.; Ravishankara, A. R.; Wallington, T. J., Atmospheric Chemistry of Small Organic Peroxy Radicals. *J. Geophys. Res.* **2001,** *106* (11), 157-182.

13. Yan, C.; Kocevska, S.; Krasnoperov, L. N., Kinetics of the Reaction of CH_3O_2 Radicals with OH Studied over the 292-256 K Temperature Range. *J. Phys. Chem. A.* **2016,** *120*, 6111-6121.

14. Kissner, R.; Nauser, T.; Bugnon, P.; Lye, P. G.; Koppenol, W. H., Formation and Properties of Peroxynitrite as Studied by Laser Flash Photolysis, High-Pressure Stopped-Flow Technique, and Pulse Radiolysis. *Chem. Res. Toxicol.* **1997,** *10*, 1285-1292.

15. Ryden, J. C., N_2O Exchange Between a Grassland Soil and the Atmosphere. *Nature* **1981,** *292*, 235-237.

16. McQuarrie, D. A., *Quantum Chemistry*. University Science Books: Sausalito, California, 2008.

17. Nicholls, R. W., Franck-Condon Factors qv'v" of Molecular Band Systems and Their Interpolation. *J. Chem. Phys.* **1956,** *24* (5), 1104.

18. Coon, J. B.; DeWames, R. E.; Loyd, C. M., The Franck-Condon Principle and the Structures of Excited Electronic States of Molecules. *J. Mol. Spec.* **1962,** *8* (1-6), 285-299.

19. Bernath, P. F., *Spectra of Atoms and Molecules*. Oxford University Press: New York, New York, 2005.

20. Weaver, A.; Arnold, D. W.; Bradforth, S. E.; M., N. D., Examination of the $^2A_2'$ and $^2E'$ states of NO_3 by Ultraviolet Photoelectron Spectroscopy of NO_3^-. *J. Chem. Phys.* **1991,** *94* (3), 1740-1751.

21. Corderman, R. R.; Lineberger, W. C., Negative Ion Spectroscopy. *Ann. Rev. Phys. Chem.* **1979,** *30* (347-378).

22. Mozhayskiy, V.; Goebbert, D.; Velarde, L.; Sanov, A.; Krylov, A., Electronic Structure and Spectroscopy of Oxyallyl: A Theoretical Study. *J. Phys. Chem. A* **2010,** *114*.

23. Eppink, A. T. J. B.; Parker, David H., Velocity Map Imaging of Ions and Electrons Using Electrostatic Lenses: Application in Photoelectron and Photofragment Ion Imaging of Molecular Oxygen *Rev. Sci. Instrum.* **1997,** *68* (9), 3477-3484.

24. Osterwalder, A.; Nee, M. J.; Zhou, J.; Neumark, D. M., High Resolution Photodetachment Spectroscopy of Negative Ions via Slow Photoelectron Imaging. *J. Chem. Phys.* **2004,** *121* (13), 6317-6322.

25. Gantefor, G. F.; Cox, D. M.; Kaldor, A., Zero Electron Kinetic Energy Spectroscopy of Au_6^- *J. Chem. Phys.* **1991,** *96* (6), 4102-4105.

26. Kitsopoulos, T. N.; Waller, I. M.; Loeser, J. G.; Neumark, D. M., High Resolution Threshold Photodetachment Spectroscopy of Negative Ions. *Chem. Phys. Lett.* **1989,** *159* (4).

27. Lindner, R.; Dietrich, H. J.; Muller-Dethlefs, K., Basic Principles of ZEKE Spectroscopy. Optimized Resolution and Accurate Ionization Energy. *Chem. Phys. Lett.* **1994,** *228*, 417-425.

28. Neumark, D. M.; Lykke, K. R.; Andersen, T.; Lineberger, W. C., Infrared Spectrum and Autodetachment Dynamics of NH^- *J. Chem. Phys.* **1985,** *83* (9), 4364-4373.

29. Spence, D.; Schulz, G. J., Vibrational Excitation and Compound States in NO. *Physical Review A* **1971,** *3* (6).

30. DeVine, J. A.; Weichman, M. L.; Xie, C.; Babin, M. C.; Johnson, M. A.; Ma, J.; Guo, H.; Neumark, D. M., Autodetachment from Vibrationally Excited Vinylidene Anions. *J. Phys. Chem. Lett.* **2018,** *9* (5), 1058-1063.

31. Chu, Y.; Senn, G.; Matejcik, S.; Scheier, P.; Stampfli, P.; Stamatovic, A.; Illenberger, E.; Mark, T. D., Formation of NO^- Following Electron Attachment to NO Clusters. *Chem. Phys. Lett.* **1998,** *289*, 521-526.

32. Osborn, D. L.; Leahy, D. J.; Cyr, D. R.; Neumark, D. M., Photodissociation Spectroscopy and Dynamics of the $N_2O_2^-$ Anion. *J. Chem. Phys.* **1995,** *104*, 5026.

33. Nichols, B.; N., S. E.; Ryazanov, M.; Neumark, D. M., Photodissociation Dynamics of the i-Methylvinoxy Radical at 308, 248 and 225 nm Using Fast Beam Photofragment Translational Spectroscopy. *J. Phys. Chem. A.* **2017,** *121*, 579-586.

34. David, H. F.; Kim, B.; Johnston, H. S.; T., L. Y., Dissociation Energy and Photochemistry of NO_3. *J. Phys. Chem.* **1993,** *97*, 2172-2180.

35. Continetti, R. E.; Cyr, D. R.; Osborn, D. L.; Leahy, D. J.; Neumark, D. M., Photodissociation Dynamics of the N_3 Radical. *J. Chem. Phys.* **1993,** *99* (4), 2616-2630.

Chapter 2: Experimental Methods and Data Analysis

2.1. Overview of Experimental Apparatus

In order to study short-lived neutral species, systems have been developed to generate fast precursor anion beams that are easily manipulated. Fast beams are used for a number of reasons, most notably due to the fact that small mass differences can be more effectively separated and fast beams significantly increase detection efficiency. Because anion sources can generate multiple precursors within a small mass range that are related, it can be beneficial to study the more than one molecule under the same conditions. This reduces variability within the experiment, as well as allowing for an increase in the speed of data collection. These experiments were conducted on a photoelectron-photofragment coincidence (PPC) spectrometer, as seen in Figure 2.1. This chapter discusses an overview of the spectrometer, which is comprised of an ion source, various guiding optics, two different forms of ion traps, an interaction region with the laser, and two detectors, for both electron detection as well as multi-particle neutral detection. Combining the techniques of ion generation and stabilization with high resolution mass separation allows for the PPC spectrometer to be operated in multi-mass collection mode, which will be discussed in this chapter.

2.1.1. Source

In order to form a variety of ion precursors, a piezo electric pulsed valve with a pulsed discharge is used. The pulsed valve consists of a small aperture that allows a controlled amount of gas from a high-pressure region to a low-pressure region. The gas

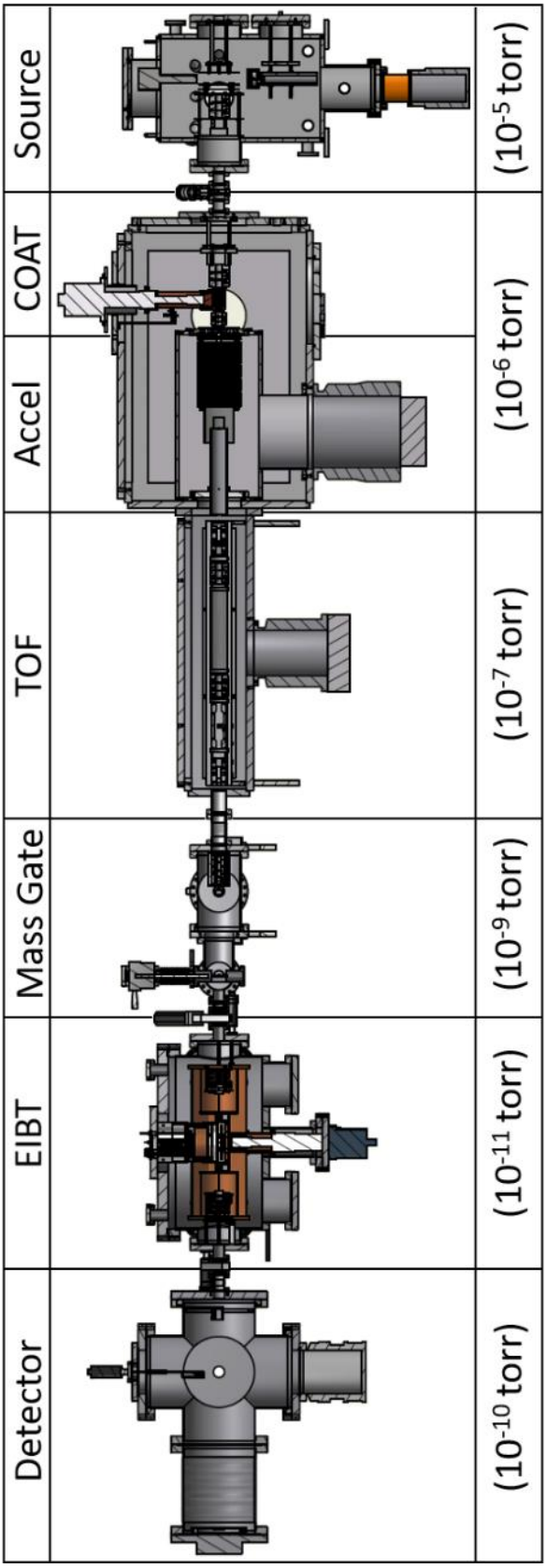

Figure 2.1. PPC spectrometer with operational pressures.

of interest is introduced to the 250 μm nozzle at a stagnation pressure of ~3 atm, by a fast piezo electric disk at 10 Hz. This change in pressure causes collisions between the molecules, which transfers vibrational and rotational energy into kinetic energy and is known as a supersonic expansion.[1] Supersonic expansions are known to have a temperature differential in the different portions of the expansion, with the center having the most collisions, and therefore the coldest ions. Hotter species are also able to be formed in the outer portions of the expansion where less collisions have occurred. While supersonic expansions have been measured to generate ions with vibrational temperatures of ~150K[2,3], experiments conducted previously in this laboratory on larger systems such as the tert-butoxide anion and the acetate anion have determined precursor temperatures of 400-1400 K, indicating that significant vibrational excitation is still possible with this source.[4, 5]

A contribution to precursor temperature is the pulsed discharge that is used with the supersonic expansion in order to generate ions. The expansion is pulsed by an electric discharge at 500 V, and stabilized with a 1 keV electron beam. The pulsed discharge ionizes and fragments the gas of interest to generate multiple ions and neutrals, while the electron beam from the filament electron gun increases the probability of creating anions. Collisions of high-energy electrons with molecules induce fragmentation and generate secondary low energy electrons in the plasma that can attach to other neutral molecules. While previously only the coldest portion of this expansion was utilized for this experiment, now all of the anions that are generated can be extracted and stabilized, resulting in high energy isomers and significant molecular rearrangement of the precursor gases or liquids that are vaporized.

The expansion is formed within a Wiley-McLaren time-of-flight spectrometer allowing for orthogonal extraction to the remaining portions of the experiment.[6] The Wiley-McLaren spectrometer is used to focus the ion packet in space and time, and consists of three plates, two that are pulsed and a third held at a constant potential. The supersonic expansion is formed between the first two plates. The first plate, also known as the source backing plate, is pulsed at a negative voltage, usually ~250 V, in order to repel the anions towards the remaining portion of the experiment, while the second plate is pulsed simultaneously at a negative voltage, ~210 V. The third plate is held at a lower voltage, ~8 V, and is used as a fine control of the focusing.

The ions are then focused by six more lens elements, which have a range of -150 to +150 V, to guide the ion beam into the next stage of the experiment. The portion of the expansion that is collected can be modified, either by the height of the pulsed valve, or by changing the time at which the expansion is extracted. By extracting at earlier times, which can be done by pulsing the Wiley plates quickly after the expansion is formed, or by positioning the pulsed valve higher in relation to the center of the Wiley-McLaren plates, the ions are given less time to collisionally cool, and results in more exotic species.

2.1.2. Cryogenic Octopole Accumulation Trap

The ions are then injected into the cryogenic octopole accumulation trap which has recently been added to the apparatus in order to cool ions into their ground vibrational states.[7] This is a linear radio frequency trap, with eight rods in a circular pattern.[8, 9] The entrance endcap is held at ground, and then switched to potential once the ions are in the trap. Within the circular pattern, alternating rods are electrically coupled, with neighboring

rods electrically isolated. This allows for an opposite RF phase to be applied to each set of rods and creates an octopole field that traps the ions in a linear trajectory. A homebuilt RF generator is used to produce the field (4MHz, 320 V peak-to-peak), and the entire trap is floated to -197 V.[10]

The ions are collisionally cooled with buffer gas that is introduced by a Gerlich valve.[11] The most common buffer gas used in these experiments is 80:20 He/H_2, but pure helium has also been proven to be sufficient to remove most of the vibrational excitation from the anions.[8] The trap is mounted on a Sumitomo RDK-205D 4K cryocooler cold head, which reduces the temperature of the trap and the buffer gas to ~17K. COAT is enclosed in radiative shielding in order to reduce black body radiation.

Both the entrance and exit sides of the trap contain lenses to help guide the ion trajectory in and out of the trap. Three shaping electrodes encompass the RF rods, in order to create a potential ramp guiding the ions towards the exit end of COAT. The ions are trapped for varying periods of time in order to thermalize to the temperature of the buffer gas, but most often in the experiments in this thesis are trapped for 40 ms. The exit endcap is then switched to ground in order to extract the ions from the trap. Three more lens elements and a voltage applied to the acceleration aperture plate guide the ions into the acceleration region.

2.1.3. Acceleration/Time-of-Flight/Mass gate

Once out of COAT, the ion packet is accelerated by plates that are incrementally increased in voltage. These 34 plates have 15 cm diameters and are separated by 1 cm. Within the stack of plates, an einzel lens is embedded in order to control the focusing of

the ions during acceleration. While ions can be accelerated to any voltage from 0-10 kV, the most frequent acceleration is to 7 kV. After being accelerated, the ions are injected into the HV switch, which is a tube that is floated at the same voltage as the end of the acceleration stack. The purpose of the HV switch is so that the ions can be re-referenced to ground, and the remaining portion of the experiment does not have to be floated to the acceleration voltage. This tube is 30 cm long with a 3 mm entrance opening and a 5 mm exit aperture and is switched to ground using a high-voltage switch (Behlke HTS 101-01). Because only the ions within the HV switch during re-referencing continue on to the subsequent portions of the experiment, the length of the HV switch is the first rough spatial determination of which masses are chosen.

In order to have a more accurate mass separation, the ions are then injected into a time-of-flight region, with a flight path of 1.13 m. Within the TOF region, there are two sets of einzel lenses and two sets of deflectors, both vertical and horizontal. These are used to focus and guide the ion packet. Each einzel lens is composed of three electrodes, with the two electrodes at either end held at ground and the center electrode held at either a positive or negative voltage to accelerate or decelerate the ions, respectively. Each deflector is composed of two sets of plates, with each set either horizontal or vertical in relation to the ion beam. A negative voltage is applied to one of the plates, while the other is held at ground in order to pull the ion beam in a specific direction.

While the TOF is usually the last mass separation before injection into the electrostatic ion beam trap, there is also a mass gate that can be employed when a specific set of masses needs to be isolated. The mass gate has been used in multi-mass experiments in order to determine the width of the ion packet, but it was found to be less sensitive than

the mass separation in the electrostatic ion beam trap. The mass gate consists of two parallel plates that have equal and opposite potentials that are pulsed to ground at a specific time. This allows for ions to be blocked from continuing into the electrostatic ion beam trap, unless they arrive at the time when the mass gate is switched to ground. This is in the mass gate chamber, along with another set of deflectors. These deflectors are the final steering optics, and allow for sensitive adjustments to injection into the electrostatic ion beam trap, which has been determined to be critical to maintaining a stable trapping trajectory.

2.1.4. Electrostatic Ion Beam Trap

The benefit of the implementation of the electrostatic ion beam trap (EIBT) is the ability to decouple the repetition rate of the source from the laser while not requiring deceleration of the ion packet.[12, 13] This is done by interrogating the same ion packet with the laser multiple times as it oscillates through the interaction region. The ion packet oscillates at keV energies in the trap between two electrostatic mirrors, which keep the ions on a specific trajectory. The mirrors are a stack of reflecting electrodes that are isolated with sapphire balls. Externally, a voltage divider is used to create a potential ramp on each mirror stack. In order to enter the trap, the entrance mirror is held at ground, and then switched to potential using a Behlke switch (HTS series). An electrostatic lens is used to help focus the trajectory within the EIBT and ion storage has been proven on the order of seconds.[14] Each mirror stack is mounted on two linear translators mounted on the corner of each of the stacks in order to give fine control to mirror alignment while remaining under vacuum. The trap region is cooled to ~20 K to reduce black body radiation and enclosed in radiation shields.

The interaction region of the ions with the laser is in the center of the EIBT in the field free region, and the electron detector is mounted above the trap. Because the interaction reaction is within the trap, the experiment can be carried out at 1037 Hz, regardless of the rate of the source. The photodetached electrons are extracted orthogonal to the ion beam, as discussed in Section 2.4.1, while the neutral particles are no longer held by the potential of the trap and travel downstream to the neutral particle detector, as discussed in Section 2.4.2.

On a single round trip between the two mirrors, the ion packet travels ~1 meter, resulting in high-resolution mass separation between different masses. This can either be employed in multi-mass mode, discusses in Section 2.6, or allow for a RF electrode to increase the overlap of a single mass with the laser beam. Coulomb interactions within the ion packet will eventually cause the ions to separate, so applying a small RF voltage, known as bunching, to the packet combats this dispersion. This also ensures that the resulting neutral fragments are travelling towards the neutral detector, rather than back towards the entrance of the EIBT. The bunching electrode is a cylinder on the entrance side of the trap through which the ions oscillate, that has a sinusoidal RF voltage. This is phaselocked to the laser, which allows the ion packet to phaselock to the laser pulses if the bunching frequency is set to the natural oscillation frequency that an individual mass within the trap. This electrode has a corresponding electrode on the exit side of the trap that is used to monitor the trapping intensities of the ions within the EIBT. While bunching is a useful technique to increase acquisition rates for a single mass, it must be deactivated in order to collect multiple masses simultaneously, and therefore was only employed for calibrations in the experiments conducted in this thesis.

2.1.5. Detector Chamber

Within the detector chamber are the multi-particle neutral detector, as well as an ion detector. The multi-particle detector will be discussed in detail in Section 2.4.2 and is mounted in the beam line on a vertical translator. This allows for multi-particle neutral detector to be moved slightly without venting the chamber. The ion detector is used prior to experiments in order to determine the time-of-flight and intensity of ions being formed. This is used for optimization of the ion beam to form the preferred precursor mass. The ion detector is mounted above the ion beam, with an ion deflector used to guide the beam into the detector. The ion detector is a chevron stack of microchannel plates with an anode and a high-speed preamplifier (Ortech VT-120).

2.2. Vacuum System

A consideration for this kind of experiment is the mean free path that the ion beam travels before interaction with background gas. By maintaining low pressures with a vacuum system, the number of collisions the ions make within the beam and with the background gas can be reduced. The requirements for these collisions change in different portions of the experiment, with collisions being nessecary in the source and COAT regions in order to generate and cool the ions, while avoiding collisions near the detectors and interaction region is nessecary. This is most critical in the EIBT, where approximately one meter is traversed per round trip for the ion packet. In order to efficiently store the ion packet in the EIBT for longer time periods, the mean free path is required to be 10^6 meters. This requires a pressure differential across the multiple chambers in order to support the

relatively high pressure regions of the source and COAT as well as the ultra high vacuum portions of the experiment.

The vaccum setup consists of two systems are that high vacuum, with resting pressures of 10^{-6} torr and lower, while the third system is ultra high vacuum with resting pressures of 10^{-9} torr and lower. The pressures for each of the chambers can be seen in Figure 2.1. The chambers are separated by small aperatures in order to maximize differential pumping and minimize gas flow between different pressure regions. Ion gauges monitor the pressures in each of the chambers and the foreline pressures are measured by thermocouple gauges. These are all connected to an interlock, which can isolate the backing pumps from the chambers with pneumatic valves and safely turn off the turbomolecular pumps if one region becomes overpressurized. The interlock also isolates the vacuum systems from each other, so that unaffected regions will remain under vacuum.

The source chamber is an independent system, due to more frequent maintenence requirements which involve venting. This system consists of an Edwards nEXT 240 turbomolecular pump (pumping speed of 240 L/s) and an Edwards XDS 35i backing pump (35 m^3/h). A gate valve is used between the source and COAT chambers so that the source can be vented without impacting the second vacuum system. The second vacuum system consists of COAT, the acceleration region, and the time-of-flight. While each of these region is a differentially pumped chamber, there are no gate valves separating the three areas. Three Edwards turbomolecular pumps are used in this system, a STP XA3203C for COAT (pumping speed 3200 L/s), a STP-A2503PV for the acceleration region (pumping speed 2200 L/s) and a STP-A803WAV-U for the time-of-flight (pumping speed 800 L/s).

All three chambers share an Edwards XDS 35i backing pump (35 m^3/h). A gate valve separates this vacuum system from the third ultra high vacuum area.

The ultra high vacuum system contains the mass gate chamber, the EIBT and the detector chamber, with each chamber able to be isolated with gate valves. This system requires maintaining low pressures, and therefore reducing the number of times each chamber needs to be vented is critical. The mass gate chamber has two turbomolecular pumps, a Pfeiffer TMU 260 (pumping speed 210 L/s) and an Edwards EXT 250H (pumping speed 250 L/s). The detector chamber also has two turbomolecular pumps, an Edwards EXT 255H (pumping speed 400 L/s) which is backed by an Osaka TG420MCAB (pumping speed 250 L/s). Both of these chambers are backed by an Edwards nXDS 10i (12.7 m^3/h) pump. The EIBT, which requires pressures of ~10^{-11}, uses an Oxford Instruments, Cryo-Plex 8 cryopump (pumping speed 2500 L/s) and a titanium sublimation pump (pumping speed 3000 L/s). The trap chamber does not contain any turbomolecular pumps, and therefore does not require a backing pump, but is connected to the Edwards nXDS 10i through a manifold which allows the chamber to be isolated. This is required when the trap chamber in vented in order reach rough vacuum required for the cryopump to be exposed to the chamber.

2.3. Laser System

Using a picosecond laser with a high repetition rate allows for high temporal resolution, which is required to directly measuring the time of arrival for electrons (see Section 2.4.1) as well as a high duty cycle to account for the low signal. A cavity-dumped, mode-locked Titanium:Sapphire-based regenerative amplifier meets these requirements,

and was used for these studies. The Ti:Sapphire (Clark MXR CPA-2000) produces a 1.2 ps pulse, 400 μJ/pulse at a repetition rate of 1037 Hz. Short laser pulses are known to have high peak power, which can cause damage to the cavity optical components, therefore chirped pulse amplification (CPA) is used. In order to create pulses that safe for amplification, dispersive gratings are used to temporarily stretch pulses to tens of picoseconds. Once amplified, a similar dispersive grating system can be used to recompress the pulse to the original short length.

The regenerative amplifier consists of multiple coupled laser systems, including a diode pumped fiber laser, and a Nd:YAG. The mode-locked diode pumped fiber laser generates low energy (nJ) picosecond pulses at 43.58 MHz, which are stretched using a grating system prior to injection at 1037 Hz into the Ti:Sapphire amplifier cavity. The amplifier cavity is pumped by the high power Q-switched Nd:YAG laser. The seed pulse passes through the Ti:Sapphire crystal multiple times until the maximum energy is reached. Once this occurs, the pulse is ejected from the cavity with a Pockel cell, and into a compressor region consisting of a grating and a prism, which is used to generate the final output.

The fundamental output of the Ti:Sapphire is 775 nm (1.60 eV) and can either be used for photodetachment, such as Chapter 4, or doubled with a beta-Barium-Borate (BBO) crystal to generate a 388 nm (3.20 eV) beam, which was employed for the remaining chapters in this thesis. The chosen wavelength is then aligned through the EIBT, using irises along the beam path in order to achieve proper alignment. The focusing of the laser can be modified to change the effective laser fluence and observe different dynamics when interacting with the ion packet. A 50 cm focal length lens is used to focus the beam to a

spot size of < 1mm in the interaction region or a 2.5:1 telescope is employed to generate a collimated beam.

2.4. Detectors

Both detectors are used to determine the velocity of the particle in three dimensions (v_x, v_y, v_z) in order to calculate the kinetic energy. For the electron detector, measuring the momentum indicates the orbital that the electron is being removed from, while on the neutral detector, the center of mass recoil of dissociating fragments is measured. Both detectors consist of a microchannel plate stack (MCP), which amplify the signal with an electron cascade and an anode that records the time and position of the resulting electron cloud. The z stacks of MCPs used on both detectors result in an electron cascade of ~10^7 electrons.[15] While both detectors employ the same method to amplify signal and detect both position and time, the anodes are unique to the kind of particle being measured. By collecting both the time and position of the particles, the electrons and their corresponding neutrals can be correlated.

2.4.1. Photoelectron Detector

After being photodetached, electrons are extracted orthogonal to the ion beam through a velocity map imaging (VMI) set up. Velocity map imaging is a common technique in photoelectron spectroscopy that is utilized to focus the electrons radially in order to achieve better resolution.[16] A new VMI configuration has been implemented in order to increase the resolution, however was not successful in impacting the overall resolution of the detector due to the short flight path of the electrons after detachment, and limitations to VMI fields interacting with trapping trajectories in the EIBT.

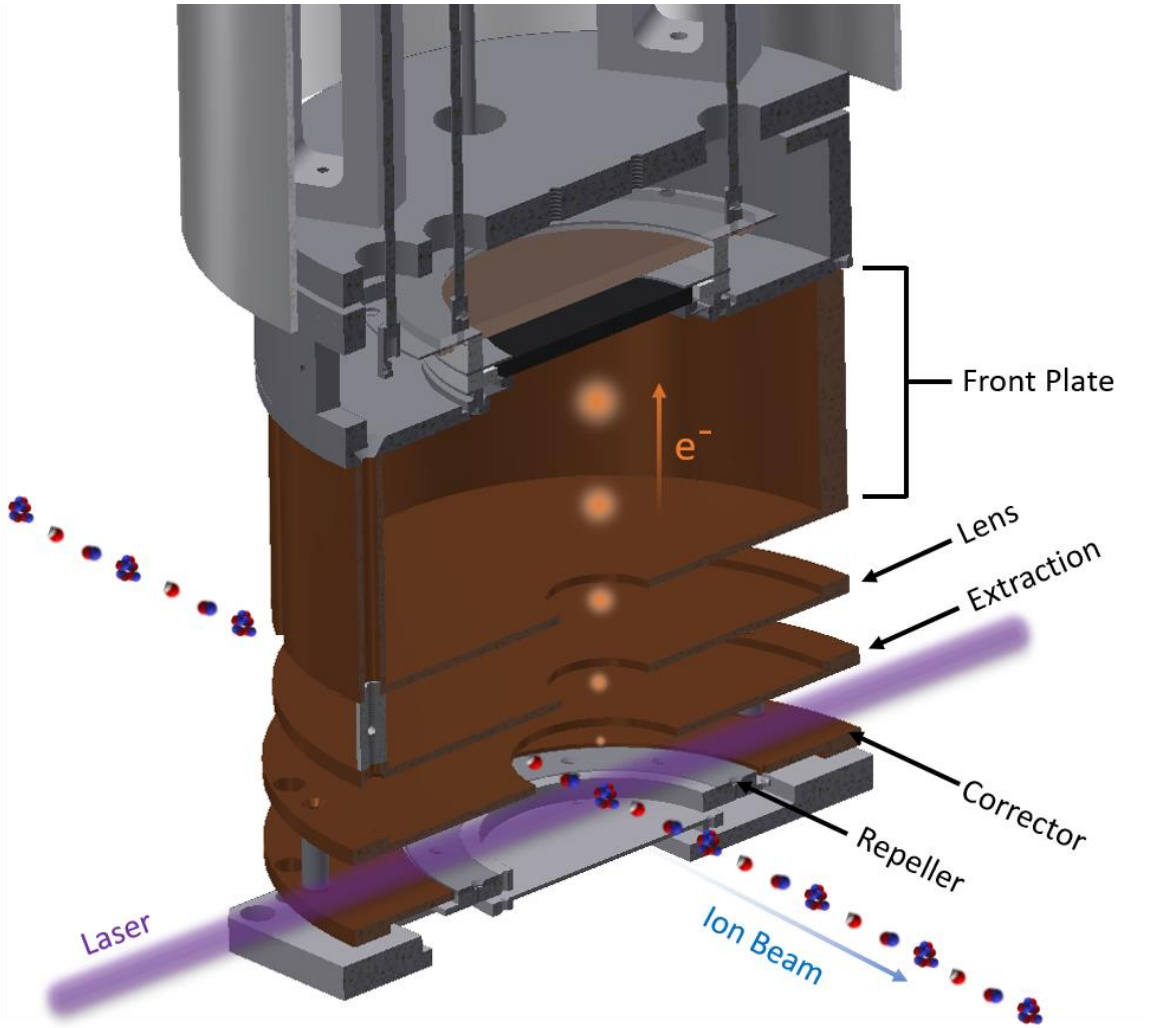

Figure 2.2. Schematic of the velocity map imaging electrodes and a portion of the electron detector.

A schematic of the current VMI apparatus can be seen in Figure 2.2. The repeller is used to direct the electrons towards the VMI set up, and a corrector of opposite polarity is used as fine control for ion packet trajectory in this region so that trapping is not affected by the repeller. The corrector and repeller are two concentric discs and the repeller contains a transmissive grid to reduce electron background.[14] This grid has recently been replaced with a solid plate, and has not been shown to have significant impact on the background signal. An extraction lens that has been modified in the new configuration, is held at ground, and another lens was added in order to focus the electrons prior to the field free region. This field free region was enclosed in the new design in order to reduce field penetration that could impact electron trajectories. While optimal spatial resolution is the goal of VMI, the timing resolution must also be considered. The current timing resolution of the electron detector is ~200 ps, but distortions to the time of arrival of electrons can have a significant impact on the overall resolution of the detector. The detector and VMI apparatus are enclosed by a magnetic shield to remove magnetic field interactions with the electron flight path.

The geometry of the anode allows for position to be determined from charge measurements. This is due to three intertwined electrodes, known as the wedge, strip and zigzag.[17-19] These are arranged in a repeating pattern, which can be seen in Figure 2.3. The wedge electrode, seen in light gray on Figure 2.3, tapers on one end in the x direction and alternates with the strip electrode, shown in black, which increases in thickness in the y direction. The zigzag electrode, shown in dark gray, separates the wedge and strip. When the electron cloud impacts the detector, the ratio of charge is used to determine position. Because each wedge component has a tapered end in the x direction, the charge measured

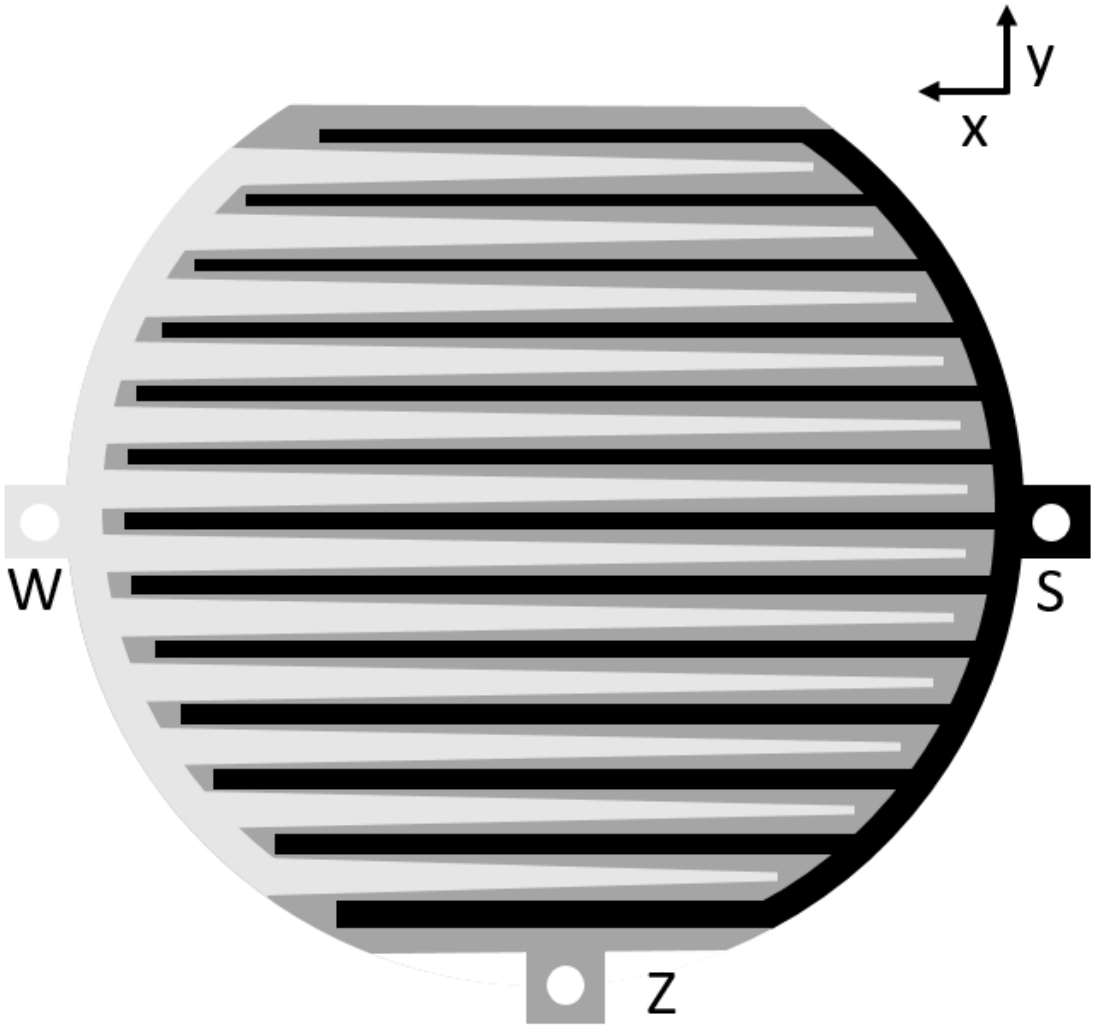

Figure 2.3. A cartoon rendering (not to scale) of the wedge, strip and z components of the electron detector.

on the wedge is compared to the overall charge to determine the position in the x direction. The increasing thicknesses of the strip is used to determine position in the y direction by comparing to the charge measured on the strip to the overall charge measured. The remaining charge is measured by the zigzag in order to normalize the total charge measured by the anode.

2.4.2. Multi-particle Neutral Detector

The neutral photofragments or photoneutrals are detected by a multi-particle detector at the end of the apparatus that measures time and position. The anode for this detector is a delay line detector, which are known to have good spatial and temporal resolution.[20, 21] In order to observe multiple particles resulting from fragmentation, four delay line quadrants are used, each of which can measure two particles simultaneously.[22, 23] This can be seen in Figure 2.4. When a charge cloud, which results from an accelerated neutral generating an electron cascade on the MCPs impinges on the detector, a charge signal is measured by the x and y fingers of the detector. The charge is then split for each axis and travels to the end of the delay lines, where the difference in time of arrival of signal is measured. The difference in time of arrival can be shown by:

$$\Delta t = t_2 - t_1 = \left(\frac{\frac{l}{2}+x}{v_{eff}}\right) - \left(\frac{\frac{l}{2}-x}{v_{eff}}\right) \tag{2.1}$$

where l is the delay line length, x is the position and v_{eff} is the effective velocity.[21] This can be directly proportional to the position on the detector face, when equation 2.1 is rearranged, as shown by:

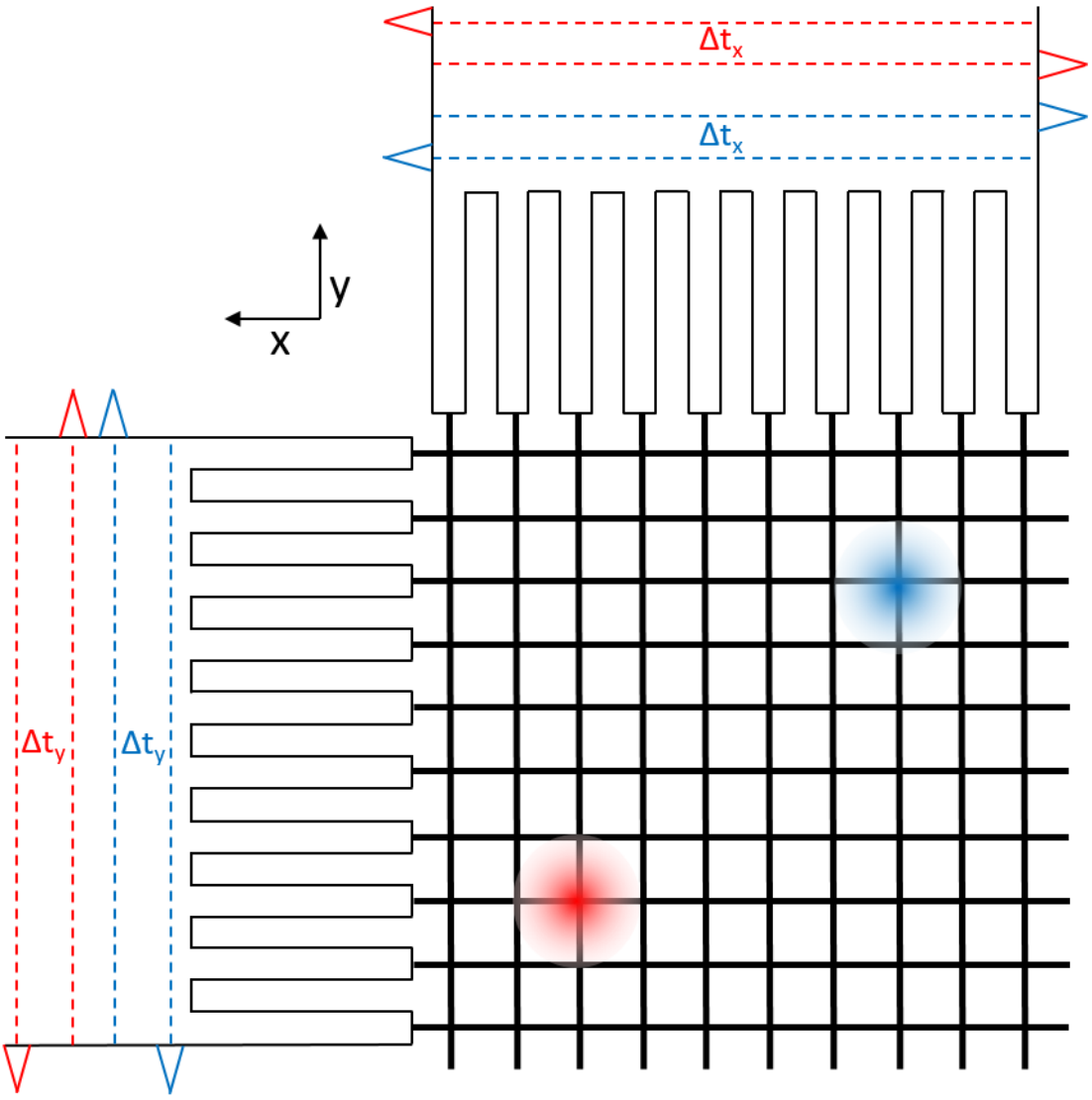

Figure 2.4. Cartoon rendering of delay line anode. This is representative of a single quadrant on the QXDL. The signal from the neutral particles are shown in red and blue, each of which triggers a signal to be sent to both ends of the serpentine delay lines. The difference in arrival time at the end of the delay line indicates position on the face of the detector.

$$x_{TAC} = \frac{\Delta t \cdot v_{eff}}{2} \tag{2.2}$$

The effective velocity of the signal is decreased in relation to the speed of light in order to have good resolution. This is done by having a long serpentine path for the signal to travel, as well as the material of the detector having a high dielectric constant. Each x and y value for the quadrants has its own effective velocity value. When a particle hits the edge of two quadrants, it is measured by both, resulting in artificially high signal between the quadrants.

2.4.3. Data Acquisition

A schematic of the signal conversion from the anodes to the computer for both the QXDL and the electron detector is shown in Figure 2.5. Each of the three charge signals from the electron detector are amplified by charge sensitive preamplifiers and converted using an analog to digital converter (ADC, Ortec AD413). The time-of-flight for the electrons is measured using a start signal from a photodiode, indicating when the laser passes through the interaction region, and the electrons being detected by the anode is used as the stop signal. The stop signal is recorded from the wedge electrode, and is amplified by a fast pre-amplifier (Ortec VT-120) before both the start and stop signal are analyzed by a constant fraction discriminator (CFD, Ortec 935). The CFD is triggered by 20% of the peak height in order to give more accurate timing information than threshold triggering. The time signals are then read by a time-to-amplitude converter (TAC, Ortec 566) with a 50 ns full scale before also being converted by the ADC. The signals from the ADC are read by a Computer Automated Measurement and Control (CAMAC) crate, which interfaces with a Labview program.

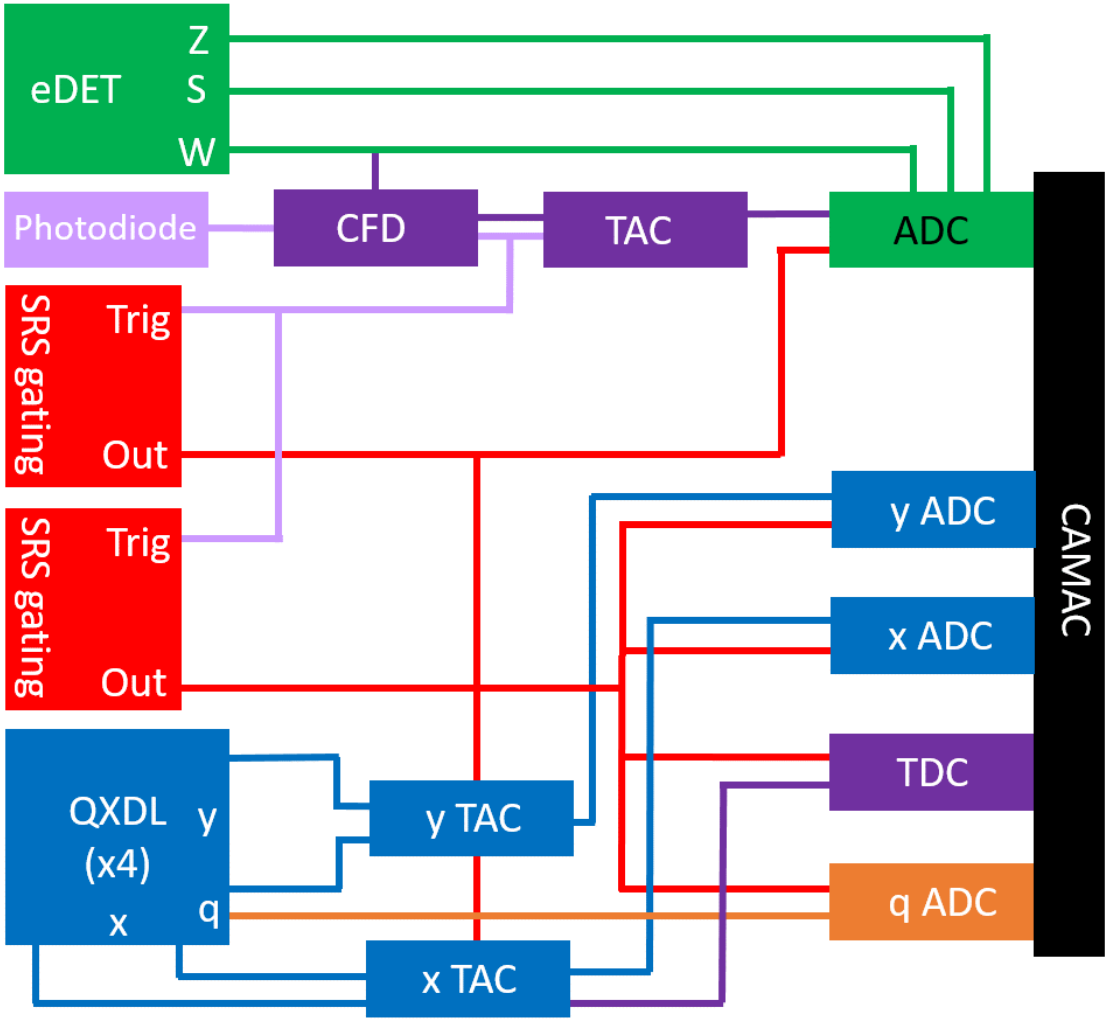

Figure 2.5. A simplified diagram of the interface between the electron and neutral detectors and the data acquisition system.

The signals from the QXDL are amplified and read by a custom 2- hit TAC (Siegmund Scientific). Eight TACs are required for the QXDL, with the first delay signal being measured as a start and the second delay signal measured as the stop time. The x and y position signals from the TAC are then relayed to two-eight channel ADCs (LeCroy 3351). The timing for the neutral detector is triggered by the photodiode signal from the laser, into a CFD (TC 454). The gating for the timing on both the electron and neutral data is controlled by a SRS DG535 and collected by a TDC (LeCroy 3371). The timing signal for the neutral time of arrival is collected off the x signal from the detector. The charge for each quadrant is also measured and collected by a third ADC (LeCroy 3351). These converted signals can then be read by the CAMAC crate in order to interface with the Labview program.

2.5. Data Analysis

The signal that is read into the Labview program for both the neutral and electron events then need to be converted to positions and times so that the velocities can be determined. This first requires data discrimination, as well as calibrating both the electron and neutral data in order to determine accurate velocities. Because this data contains a large amount of information, the ways in which the various gating techniques are used become critical. This includes gating on centroids and masses for the neutral data, and slicing and DAF corrections for the electron data. Finally, the way the correlated electron and neutral data will be discussed in the context of two dimensional coincidence plots, as well as total energy spectrum.

2.5.1. Data Discrimination

An important step in data analysis is discriminating the signal so that the individual neutral signal sorted according to the number of fragments that are produced, as well as the electron and neutral data being correlated. The first step is determining that all of the neutral data has a valid x, y and t signal, and that the electron data contains valid time signal and a charge signal from the three anodes. The data is then separated into categories of electron only events, neutral only events, and events with an electron in coincidence with neutral particles. The data that is sorted to have electrons in coincidence with neutrals is further categorized by the number of neutral photoneutrals or photofragments that are measured, with one, two or three particles being the most frequent number of particles observed. These files are then analyzed in a program known as Patti that allows the number of neutral particles to be specified. This program helps to isolate only the data of interest, removing events resulting from other masses, or multi-electron events.

2.5.2. Electron Calibration

The electron data is measured as a charge signal, as discussed in Section 2.4.1. While the charge for each anode is measured independently, the wedge, strip and zigzag are capacitively coupled.[19] Cross-talk factors (C_{ws}, C_{zw}, C_{sz}) are used in order to account for this coupling and have been determined through calibration. These factors in combination give three position constants for both the x and y direction, which can be seen below.

$$XC = \begin{Bmatrix} 1 - 2C_{SZ} - C_{WS}, \\ C_{WS} - C_{ZW}, \\ 1 - 2(C_{WS} + C_{zw} + C_{sz}) + 3(C_{zw} \cdot C_{sz} + C_{ws} \cdot C_{sz} + C_{ws} \cdot C_{zw}) \end{Bmatrix} \quad (2.3)$$

$$YC = \begin{Bmatrix} 1 - 2C_{zw} - C_{ws}, \\ C_{ws} - C_{sz}, \\ 1 - 2(C_{WS} + C_{zw} + C_{sz}) + 3(C_{zw} \cdot C_{sz} + C_{ws} \cdot C_{sz} + C_{ws} \cdot C_{zw}) \end{Bmatrix} \quad (2.4)$$

Other calibration factors used to determine position are the detector additive constant (DAC) and the detector multiplicative constant (DMC). Corrections for focusing of the VMI are also used, and have been discussed in detail previously.[23] All of these correction factors are determined through calibrations of well-known systems such as O^- or O_2^-. Combining these position constants from equation 2.3 and 2.4 to account for cross talk factors with the DMC and DAC corrections result in the charge being converted to position using the following equations:

$$X = DAC_x + \frac{\left[DMC_x \cdot \left(\frac{Q_s}{Q_{tot}} - C_{sz}\right) \cdot XC_1 - XC_2\left(\frac{Q_w}{Q_{tot}} + C_{zw}\right)\right]}{XC_3} \quad (2.5)$$

$$Y = DAC_y + \frac{\left[DMC_y \cdot \left(\frac{Q_w}{Q_{tot}} - C_{zw}\right) \cdot YC_1 - YC_2\left(\frac{Q_s}{Q_{tot}} + C_{sz}\right)\right]}{YC_3} \quad (2.6)$$

Where Q_s, Q_w and Q_{tot} are the charge on the strip, wedge and the total charge. These give the position values, but the time must also be calibrated. This is also done with DAC and DMC factors that are determined with known systems:

$$TOF = DMC_t \cdot t_{meas} + DAC_t \quad (2.7)$$

where the t_{meas} is the time measured from the experiment. The focusing effects of the VMI change the electron flight time, meaning that an effective TOF (TOF-t_{cal}) must be used in order to calculate velocities. The x, y and z velocities are represented as:

$$v_x = \frac{x}{TOF_{eff}} \quad (2.8)$$

$$v_y = \frac{y}{TOF_{eff}} \tag{2.9}$$

$$v_z = \frac{\Delta v_z}{\Delta TOF_{eff}} \left(TOF_{eff} - TOF_0\right) \tag{2.10}$$

Where TOF_0 is the time-of-flight for a zero-energy electron. The electron kinetic energy can then be calculated using equations 2.8-2.10:

$$eKE = \frac{m_e\left(v_x^2 + v_y^2 + v_z^2\right)}{2} \tag{2.11}$$

2.5.3. Neutral Calibrations

The neutral calibrations are significantly less involved than the electron data. Because the time is measured for the neutral detector in order to determine position, it is assumed that crosstalk factors impact the signal significantly less than the charge measurements on the electron detector. Due to the minor contribution of cross-talk factors, only DMC and DAC are needed to calibrate the neutral positions. For x and y positions this is calibrated by:

$$x = DMC_x \cdot x_{TAC} + DAC_x \tag{2.12}$$

$$y = DMC_y \cdot y_{TAC} + DAC_y \tag{2.13}$$

Where the x_{TAC} and y_{TAC} are the signal measured from the TAC as described in equation 2.1. For the multi-particle neutral detector, O_4^- is used as a well-studied system in order to determine the calibration constants. These positions are then used to calculate the velocity as shown in the following equations:

$$v_x = \frac{x}{TOF_{CM}} \tag{2.14}$$

$$v_y = \frac{y}{TOF_{CM}} \tag{2.15}$$

$$v_z = v_{beam} \cdot (TOF - TOF_{CM}) \tag{2.16}$$

The TOF_{CM} is the time-of-flight for the center of mass. When a dissociation occurs along the beam path, the center of mass deviates from these equations, due to the fact that the fragments travelling towards the detector have a shorter flight time and the particles travelling away from the detector have a longer flight time. This has a minimal effect on the KER for the experiments discussed in this thesis, but has been shown to have more of an impact in previous experiments.[23, 24] While the neutral detector is capable of three and four body dissociation experiments, only two body dissociations will be discussed in this thesis. As discussed in Section 1.3, the Kinetic Energy Release (KER) can be calculated from the center of mass:

$$KER = \frac{p_1^2}{2m_1} + \frac{p_2^2}{2m_2} \tag{2.17}$$

Where p_1 and p_2 are the momentum vectors of the particles resulting from dissociation, and m_1 and m_2 are the masses of the fragments.

2.5.4. Gating

Gating is used in order to increase the resolution of the individual data sets, as well as to cleanly separate different data from the same collection. While most of the bad data is removed through data discrimination, false coincidence is still considered valid events,

and must be removed through gating. The primary gates that are employed are centroid gating of the neutral data and electron slicing, but in certain data sets discussed in this thesis, mass gating and KER gating are also used for the neutral data. These gating techniques are especially critical in multi-mass data collection, due to the fact that different mass dissociations can have overlap in fragment time of arrivals.

Centroid gating is used in order to reduce contribution from neighboring masses, false coincidences, and different fragmentation channels. Dissociations from different parent masses will have different center of mass vectors. By gating on the center of mass of a specific dissociation, contributions from other masses will be removed. This gating also helps to reduce contribution from false coincidences. These can occur when two impacts are registered on the neutral detector with an electron, but are the result of two stable neutrals, or a stable neutral with one of the dissociative fragments. As discussed in Section 2.5.3, the center of mass is based on an assumed fragmentation, so centroid gating can also separate individual dissociation channels from the same parent mass. This is critical to observing distinct dissociation dynamics when there is a significant different in the masses of the fragments formed.

While centroid gating will remove most of the contributions from other fragmentation channels, mass gating will ensure that only a specific range of masses will be analyzed. This can either be used to analyze fragments of the same mass, or differing masses, but is often only used when there is a large difference in fragment mass between two different dissociation channels. Mass gating is not frequently employed in analysis because it cannot be used when the masses of the fragments are not known. If the incorrect

mass of the fragments is input and gated on, the program will fit the data to the given masses, and output incorrect results.

The position information from the electron detector has a smaller uncertainty than the timing. This is the result of nonlinearities in the time to velocity conversion discussed in Section 2.5.2. Because the error on the v_z is larger than v_x and v_y, analyzing the data surround $v_z \sim 0$ gives a significant reduction in this error contribution. By slicing the data, low energy electrons and electrons that are ejected along the laser vector are favored, resulting in a change in relative intensities of the peaks in the photoelectron spectrum. This can be corrected by the data acceptance function, which is represented below.

$$DAF = \begin{cases} \frac{|v| \sin\theta}{v_z^{slice}}, & |v| > v_z^{slice}, \theta(|v|) > \theta^{slice}(|v|) \\ 1, & |v| \leq v_z^{slice} \\ 1, & \theta(|v|) \leq \theta^{slice}(|v|) \end{cases} \quad (2.18)$$

Figure 2.6 shows an O_2^- photoelectron spectrum collected at 3.20 eV and how different slicing conditions change the resolution. The top panel is unsliced, the middle panel is sliced without DAF corrections and the bottom panel is slicing with DAF corrections.

KER gating can be used when two different electronic states have different dissociation dynamics, but span the same energy regime in the photoelectron spectrum. This is employed in Chapter 5 in order to observe the two different photoelectron spectra by gating on different portions of the KER. A similar process can be used to gate on different portions of a photoelectron spectrum in order to observe changes in the KER, but was not employed for this thesis.

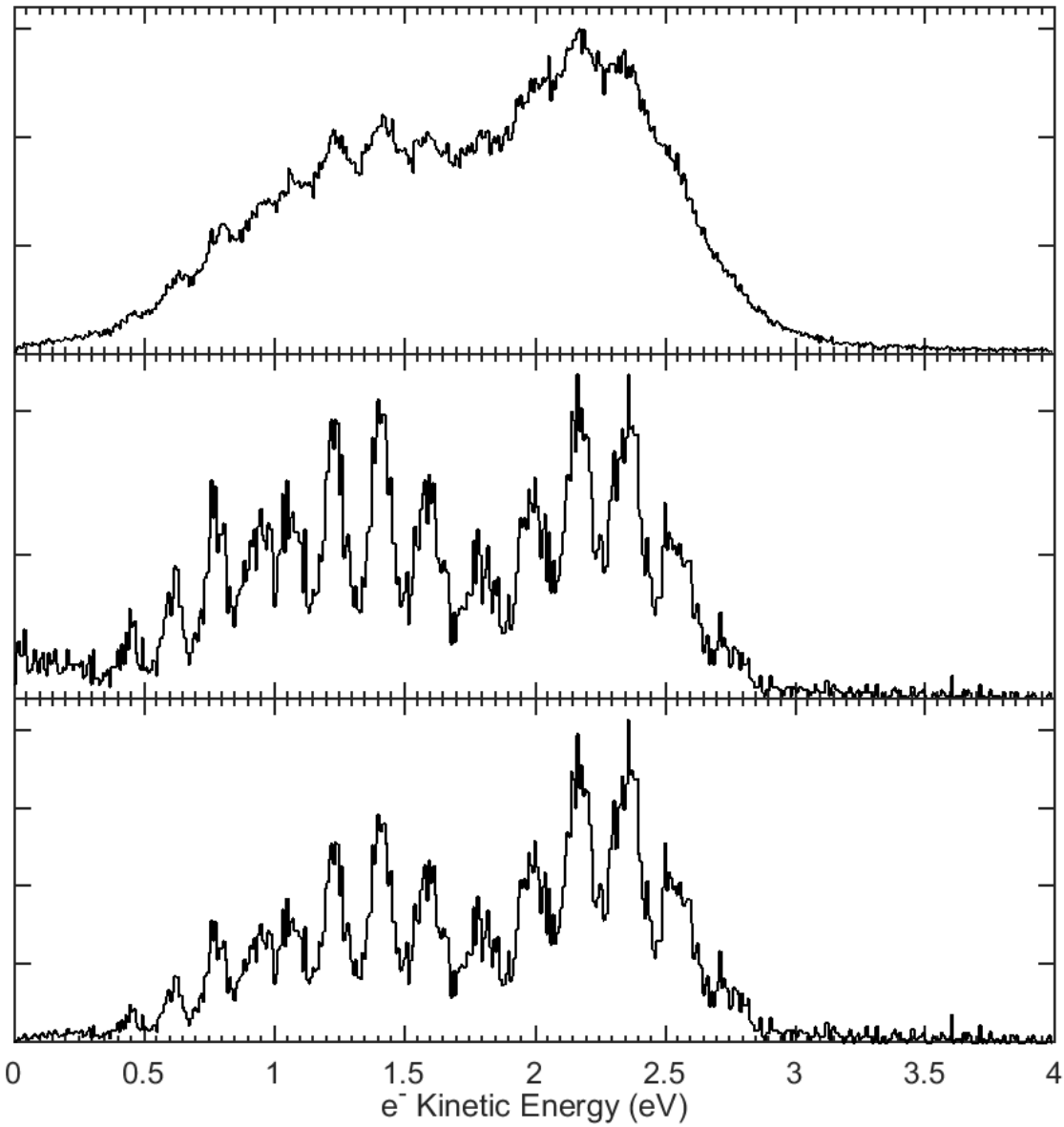

Figure 2.6. A comparison of the resolution of the photoelectron spectra of O_2^- at 388 nm (3.20 eV) when data is unsliced (top panel), sliced without DAF correction (center panel) or sliced with DAF correction (bottom panel).

2.5.5. Coincidence Calculations

Once the energies for the electron and neutrals are calculated, the total energy can be represented as,

$$E_{tot} = eKE + KER \tag{2.19}$$

which can be represented in two methods, either a one dimensional histogram or a coincidence spectrum. A coincidence spectrum is a two dimensional representation of the total energy, with the kinetic energy release on one axis and the electron kinetic energy on the other. This can reveal different features that might not be as clearly represented in a one dimensional E_{tot} plot. As discussed in Chapter 1, kinetic energy maxima can be plotted on a coincidence plot in order to give insight into the internal energy of the precursors. Coincidence plots can also reveal different mechanisms through the signatures on the plot, such as ionic photodissociation, which is seen as vertical features, or autodetachment, which is observed as low eKE bands. In Chapter 6, these eKE peaks are seen to have a slight shift in energy which is dependent on KER. This is only seen as peak broadening in a one-dimensional plot. Gating on the KER can also be used to distinguish different photoelectron spectra from the same data, if different dissociation dynamics are observed. A coincidence plot also helps to easily identify non-physical features, such as false coincidence.

2.6. Multi-Mass Data Collection

Mass spectrometry is used in a variety of fields to characterize systems based on mass to charge ratios. One of the most common forms is time-of-flight mass spectrometers

(TOFMS). This method of analysis can be used to determine ion intensity, but the detection of TOFMS is limited by short flight paths or large mass to charge ratios.[25] With the development of new methods to form and stabilize a multitude of different anions, a more sensitive mass separation is required to correctly identify small mass variations. Multi-mass data collection allows for better mass separation and mass assignment based on neutral particle time of arrivals, instead of information based on the anion precursors.

Multi-mass collection mode is a technique that can be used when multiple anions within a similar mass range are generated. This allows for all the masses to be collected at the same time, but for individual coincidence plots and photoelectron spectra to be generated from the same data set. This reduces the variability within collection, so that a direct comparison can be made between different species under the same conditions. This technique can be used to observe analogs that have similar masses or derivatives from the similar precursors simultaneously, reducing the time required to collect comparison studies.

Multi-mass data collection is possible because of the electrostatic ion beam trap (EIBT). This technique gives the ability to trap multiple particles in a specific trajectory, as discussed in Section 2.1.4. Zajfman and coworkers were able to prove that multiple ion masses could be stored in a trap at the same time. Using this technique, they were able to create high resolution mass spectrometry due to each of the individual species having its own oscillation frequency.[26] This method was proven to work to differentiate between different isotopes of the same ion, but has also been applied to larger molecular systems.[27] Unlike TOFMS, the EIBT is not limited by the mass of the species being studied.

In order to create multiple anions with small mass variations, hydrogen, oxygen, nitrogen and carbon were used as precursor molecules. These are some of the most abundant elements in the universe, and are the source for many chemical reactions. Because there are many possible systems that can be formed at a range of different atomic masses with reported photoelectron spectra, this combination of elements makes an ideal system to study multi-mass capabilities. Because of the advances in ion generation that have resulted from the implementation of COAT, as discussed in Section 2.6, the ability to run multi-mass collection has become more critical to the experiment.

In order to obtain a multi-mass collection mode, bunching of the ion packet within the EIBT must be disabled. Multi-mass collection has been used in the past, but has been limited to collecting only two systems at the same time.[14, 28] Any species within the chamber when the entrance mirror closes will be trapped. The limiting factor in number of masses that can be obtained is the time window of the neutral particle detector. The neutral fragments are detected in a 900 ns time window, with up to ten individual molecules able to be collected simultaneously. The mass assignments are chosen based on time of arrival on the neutral detector, which can be seen in Figure 2.7. These assignments are determined by the calculated time of arrival based on the known acceleration energy of the particles and the flight path to the neutral detector.

Each of the individual photoelectron spectra can be found based on the electrons in coincidence with a specific photoneutrals or photofragments time-of-flight. In analysis, gating within the neutral time-of-flight allows for different centroids to be correlated with time of arrivals. The electrons correlated to these centroids can then be extracted from the overall photoelectron spectrum. When the centroids for two species are close in times, such

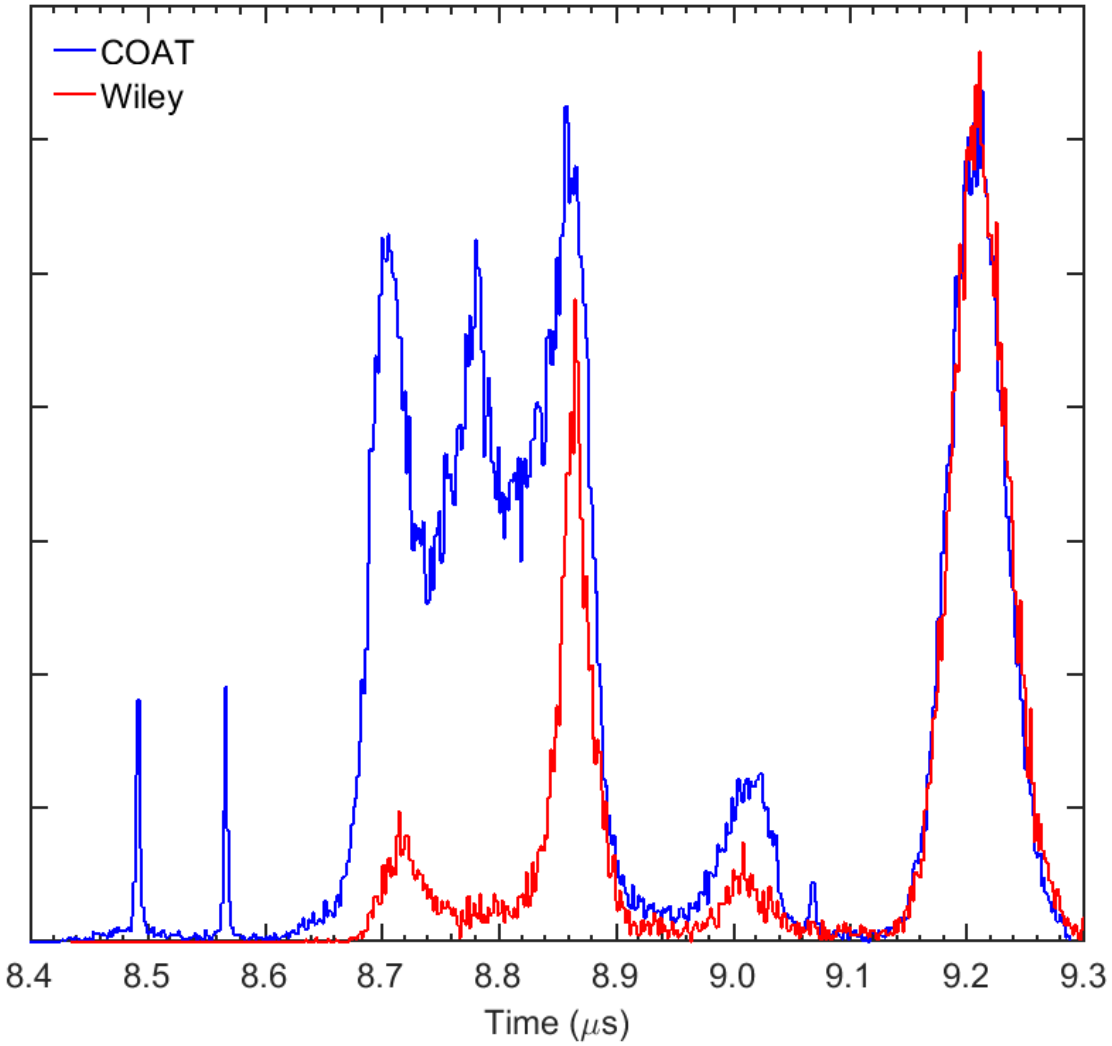

Figure 2.7. Multi-mass mode time-of-flight both with and without COAT. The difference in ion intensity changes, most notably the lack of 56 and 57 amu in the Wiley data, as well as 61 amu, which is not present in the COAT data.

as mass 60 and mass 62, gating on time of arrival could cause real signal from one of the centroids to be lost in the process of gating out the other. In order to correct for this, the center of mass gating, which is used on all data in order to reduce signal from border hits on the QXDL, becomes critical. This allows for more sensitive control in analyzing the data from each individual dissociation and removes crosstalk from other species within the photoelectron spectra.

Due to the variety of anion precursors produced, six individual molecules were collected within range of ten mass units at a photon energy of E_{hv} = 3.20 eV. For each of these systems, both the electron and the neutral particles were collected. Stable and dissociative channels were seen in the different spectra. An example of a time-of-flight using multi-mass collection mode can be seen in the blue trace in Figure 2.7. The first peak in the time of arrival is a stable neutral, with a minor dissociation channel, which has been assigned to mass 56. The second mass also photodetached to a stable neutral product and is assigned to mass 57. The stable data from mass 56 and 57 are assigned as the oxyallyl diradical (C_3H_4O) and the acetone enolate radical (C_3H_5O), and are discussed in Chapter 3. A minor dissociative channel for the oxyallyl diradical at E_{hv}=3.20 eV is discussed in Chapter 4. Photoexcitation of the oxyallyl anion was also investigated at E_{hv}=1.60 eV, which is the focus of Chapter 5. The most intense peak has been assigned to the photodissociation of $N_2O_2^-$, which is discussed further in Chapter 6. Two other dissociative peaks were observed and can be attributed to the photodissociation of NO_3^-, discussed in Chapter 7, and the photodissociation of NO^- $(H_2O)_2$ clusters. The final stable peak was determined to be mass 64 and could possibly be assigned as photodetachment of C_4O^- resulting from an excited state of the anion, though this assignment is tentative at best.

2.7. Exotic Species Stabilization

In order to characterize the contribution COAT plays in ion stabilization, the trap can be turned off, with all of the electrodes grounded, and the ions pass through unaffected. This results in a larger energy spread in the ion packet due to the lack of cooling within COAT. Without COAT, the Wiley-McLaren time-of-flight spectrometer focuses the ions through the grounded electrodes and into the remaining portion of the experiment. A change in the ions that are formed is expected, and observed in the neutral particle time of arrival, as seen in Figure 2.7. Under the same source conditions, a different distribution in anion photodetachment is observed. All of the photoneutrals, (mass 56, 57, and 64) are not observed without COAT, and a significant decrease in mass 60 and 62 is seen. Significant rearrangement of the glyoxal precursor is required to produce mass 56 and 57, the oxyallyl diradical and the acetone enolate radical and the nitrogen oxides produced at mass 60 and 62 have been determined to be higher energy isomers. Without COAT, an increase in signal related to weakly bound clusters was seen. Mass 66 is seen in the same intensity in either mode, indicating that COAT is not necessary to the stabilization of $NO^-(H_2O)_2$ clusters. Mass 61, which was unobserved with COAT, is one of the main signals in the non-COAT data. This is the result of $OH^-(N_2O)$ clusters, which are slightly dissociative, and possibly did not survive the collisional cooling process within COAT.

The addition of the Wiley-McLaren spectrometer contributes to a larger distribution of the expansion being collected, and for COAT to stabilize these exotic species. Previously, only the coldest part of the expansion was used for experiments, but by stabilizing exotic species with COAT, the full range of potential precursors from the supersonic expansion can be studied. Having the ability to turn COAT off still allows for

weakly bound clusters that are generated to be observed, as well as to determine which species are the result of the collisional cooling within COAT. By stabilizing hot anions in local minima with COAT, these anions are able to exist on the timescale of the experiment. This opens up a range of vibrationally cold, but excited electronic states that have not been as extensively studied using photoelectron-photofragment coincidence spectroscopy.

2.8. References

1. Deckers, J.; Fenn, J. B., High Intensity Molecular Beam Apparatus. *Rev. Sci. Instrum.* **1962,** *34* (1), 96-100.

2. Smalley, R. E.; Wharton, L.; Levy, D. H., Molecular Optical Spectroscopy with Supersonic Beams and Jets. *Acc. Chem. Res.* **1977,** *10*, 139-145.

3. Mate, B.; Tejeda, G.; Montero, S., Raman Spectroscopy of Supersonic Jets of CO_2: Density, Condensations, and Translational, Rotatational and Vibrational Temperatures. *J. Chem. Phys.* **1998,** *108* (7), 2676-2685.

4. Shen, B. B.; Poad, B., L. J.; Continetti, R. E., Photoelectron-Photofragment Coincidence Studies of the *tert*-Butoxide Anion $(CH_3)_3CO^-$, the Carbanion Isomer $(CH_3)_2CH_2COH^-$, and Corresponding Radicals. *J. Phys. Chem. A.* **2014,** *118*, 10223-10232.

5. Lu, Z.; Continetti, R. E., Dynamic of the Acetyloxyl Radical Studied by Dissociative Photodetachment of the Acetate Anion. *J. Phys. Chem. A.* **2004,** *108*, 9962-9969.

6. Wiley, W. C.; McLaren, I. H., Time of Flight Mass Spectrometer with Improved Resolution. *Rev. Sci. Instrum.* **1955,** *26*, 1150-1157.

7. Shen, B. B. Preparation of Hot and Cold Ions for Photoelectron-Photofragment Coincidence Spectroscopy. University of California, San Diego, San Diego, 2018.

8. Shen, B.; Benitez, Y.; Lunny, K. G.; Continetti, R. E., Internal Energy Dependence of the Photodissociation Dynamics of O_3^- Using Cryogenic Photoelectron-Photofragment Coincidence Spectroscopy. *J. Chem. Phys.* **2017,** *147*, 094307.

9. Otto, R.; Xie, J.; Brox, J.; Trippel, S.; Stei, M.; Best, T.; Seibert, M. R.; Hase, W. L.; Wester, R., Reaction Dynamics of Temperature-Variable Anion Water Clusters Studied with Crossed Beams and By Direct Dynamics. *Faraday Discuss.* **2012,** *157*, 41-57.

10. Jones, R. M.; Gerlich, D.; Anderson, S. L., Simple Radio-Frequency Power Source for Ion Guides and Ion Traps. *Rev. Sci. Instrum.* **1997,** *68* (9), 3357-3362.

11. Gerlich, D.; Mueck, G. J.; Person, U. Schnelles Ventil zur Erzeugung Sehr Kurzer Gasimpulse.

12. Johnson, C. J. Investigation of the Reaction of OH and CO to form H and CO_2 by Photoelectron-Photofragment Coincidence Spectroscopy in a Cryogenic Ion Beam Trap. University of California, San Diego, San Diego, 2011.

13. Dahan, M.; Fishman, R.; Heber, O.; Rappaport, M.; Altstein, N.; Zajfman, D.; van der Zande, W. J., A New Type of Electrostatic Ion Trap for Storage of Fast Ion Beams. *Rev. Sci. Instrum.* **1998,** *69*, 76-83.

14. Johnson, C. J.; Shen, B. B.; Poad, B. L. J.; Continetti, R. E., Photoelectron-Photofragment Coincidence Spectroscopy in a Cryogenically Cooled Linear Electrostatic Ion Beam Trap. *Rev. Sci. Instrum.* **2011,** *82*, 105105.

15. Siegmund, O. H. W.; Coburn, K.; Malina, R. F., Investigation of Large Format Microchannel Plate Z Configurations. *IEEE Trans. Nucl. Sci.* **1985,** *32* (1), 443-447.

16. Eppink, A. T. J. B.; Parker, David H., Velocity Map Imaging of Ions and Electrons Using Electrostatic Lenses: Application in Photoelectron and Photofragment Ion Imaging of Molecular Oxygen. *Rev. Sci. Instrum.* **1997,** *68* (9), 3477-3484.

17. Martin, C.; Jelinksky, P.; Lampton, M.; Malina, R. F.; Anger, H. O., Wedge-and-Strip Anodes for Centroid-Finding Position-Sensitive Photon and Particle Detectors. *Rev. Sci. Instrum.* **1981,** *52* (7), 1067-1074.

18. Siegmund, O. H. W.; Malina, R. F.; Coburn, K.; Werthimer, D., Microchannel Plate EUV Detectors for the Extreme Ultraviolet Explorer. *IEEE Trans. Nucl. Sci.* **1984,** *31*, 776-779.

19. Siegmund, O. H. W.; Lampton, M.; Bixler, J.; Bowyer, S.; Malina, R. F., Operational Characteristics of Wedge and Strip Image Readout Systems. *IEEE Trans. Nucl. Sci.* **1986,** *33*, 724-727.

20. Lampton, M.; Siegmund, O.; Raffanti, R., Delay Line Anodes for Microchannel-Plate Spectrometers. *Rev. Sci. Instrum.* **1987,** *58*, 2298-2305.

21. Friedman, P. G.; Cuza, R. A.; Fleischman, J. R.; Martin, C.; Schiminovich, D.; Doyle, D. J., Multilayer Anode with Crossed Serpentine Delay Lines for High Spatial Resolution Readout of Microchannel Plate Detectors. *Rev. Sci. Instrum.* **1996,** *67*, 596-608.

22. Hanold, K. A.; Luong, A. K.; Clements, T. G.; Continetti, R. E., Photoelectron-Multiple-Photofragment Coincidence Spectrometer. *Rev. Sci. Instrum.* **1999,** *70*, 2268-2276.

23. Clements, T. Multi-Body Dissociative Photodetachment Dynamics of Small Molecular and Cluster Anions. University of California, San Diego, San Diego, 2002.

24. Savee, J. An Experimental Probe of Electronic Interactions in Excited Molecules Produced by Charge Exchange. University of California San Diego, San Diego, 2009.

25. Guilhaus, M., Principles and Instrumentation in Time-of-Flight Mass Spectrometry. *J. Mass. Spectrom.* **1995,** *30*, 1519-1532.

26. Zajfman, D.; Rudich, Y.; Sagi, I.; Strasser, D.; Savin, D. W.; Goldberg, S.; Rappaport, M.; Heber, O., High Resolution Mass Spectrometry Using a Linear Electrostatic Ion Beam Trap. *Int. J. Mass. Spectrom.* **2003,** *229*, 55-60.

27. Rahinov, I.; Toker, Y.; Heber, O.; Strasser, D.; Rappaport, M.; Schwalm, D.; Zajfman, D., Lifetime Measurements in an Electrostatic Ion Beam Trap Using Image Charge Monitoring. *Rev. Sci. Instrum.* **2012,** *83* (3), 033302.

28. Poad, B. L. J.; Johnson, C. J.; Continetti, R. E., Photoelectron-Photofragment Coincidence Studies of NO^--X Clusters (X = H_2O, CD_4). *Faraday Discussions* **2011,** *150*, 481-492.

Chapter 3: Spectroscopy of Ethylenedione and Ethynediolide: A Reinvestigation

3.1. Introduction

Efforts to observe the ethylenedione molecule (OCCO) have led to many failed attempts to create the stable neutral product.[1-3] While many analogs have been successfully characterized including C_2OS and C_2S_2, long-lived states of neutral OCCO have not been observed synthetically or spectroscopically since it was first predicted.[4-9] Neutralization-reionization mass spectrometry, a technique for the examination of transient species, has also been unfruitful.[10] Recently, Sanov and co-workers claimed the observation of OCCO, and its analog HOCCO, using anion photoelectron spectroscopy.[11] In order to build upon their work, and examine their predictions about the dissociation dynamics of neutral OCCO, photoelectron-photofragment coincidence (PPC) spectroscopy was used to study potential isomeric anions at a mass-to-charge (m/z) ratio of 56 and 57.

PPC spectroscopy combines photoelectron spectroscopy in coincidence with measurements of the dissociation dynamics of photodetached neutral products or stable photoneutrals.[12] A pulsed discharge of glyoxal vapor and N_2O was suggested in reference 11 to form $OCCO^-$ through an abstraction of H_2^+ from glyoxal. Using this method, photoelectron spectra for m/z 56 and 57 anions were recorded at E_{hv} = 3.20 eV (388 nm), as seen in Figure 3.1. These spectra were collected in coincidence with one stable neutral product, shown by the sharp peaks in the time-of-flight (TOF) spectrum in Figure 3.2. A minor dissociation channel attributed to the same molecule was also observed in the m/z 56 time-of-flight, and will be expanded upon in a later chapter. Based on ref. 11, photodetachment of $OCCO^-$ (m/z 56) would be expected to produce the manifold of low-

lying electronic states of OCCO, including the triplet ground state inferred to have a lifetime of ~0.5 ns, and three dissociative singlet states. Sanov and co-workers also reported a comparison of the photoelectron spectra for the m/z = 56 and 57 anions, assigning the latter to ethynediolide ($HOCCO^-$).[13] A comparison of the spectra from reference 13 recorded at E_{hv} = 3.49 eV, Figure 3.3(a), and the spectra in Figure 3.1 show nearly identical features. The photoelectron spectrum for m/z 56 reported here is consistent with the spectra reported in ref. 11, however, it corresponds to neutral products that are stable on the > 8 μs neutral time-of-flight in this experiment. Such a stable product is clearly not consistent with the OCCO triplet state lifetime reported in ref. 11 and theoretical predictions for this molecule.

Theoretical studies have predicted that the triplet ground state of neutral OCCO is linear and more stable than the spin-allowed dissociation channel producing $CO(^3\Pi)$ + $CO(^1\Sigma^+)$ by 3.2-3.5 eV.[10, 14, 15] Several dissociative singlet states were also predicted, the lowest calculated to cross 0.13 eV above the triplet state minimum.[10] The triplet ground state was predicted to undergo intersystem crossing prior to dissociation into singlet products $CO(^1\Sigma^+)$ + $CO(^1\Sigma^+)$, calculated to be exothermic by some 2.5 eV.[10] This low energy crossing has been proposed to result in a short lifetime for triplet OCCO, perhaps rationalizing why it has not been experimentally observed. These predictions are consistent with the assignments made in ref. 11 but not with the stable neutral product seen in the PPC experiments as shown in the time-of-flight spectrum in Figure 3.2. The observation of a vibrationally resolved spectrum at E_{hv} = 2.33 eV was also reported in ref. 11 and assigned to the OCCO triplet state, seen in Figure 3.3(b). From this spectrum, the adiabatic electron affinity (AEA) of the stable $^3\Sigma^-$ state was reported to be 1.936(8) eV and the

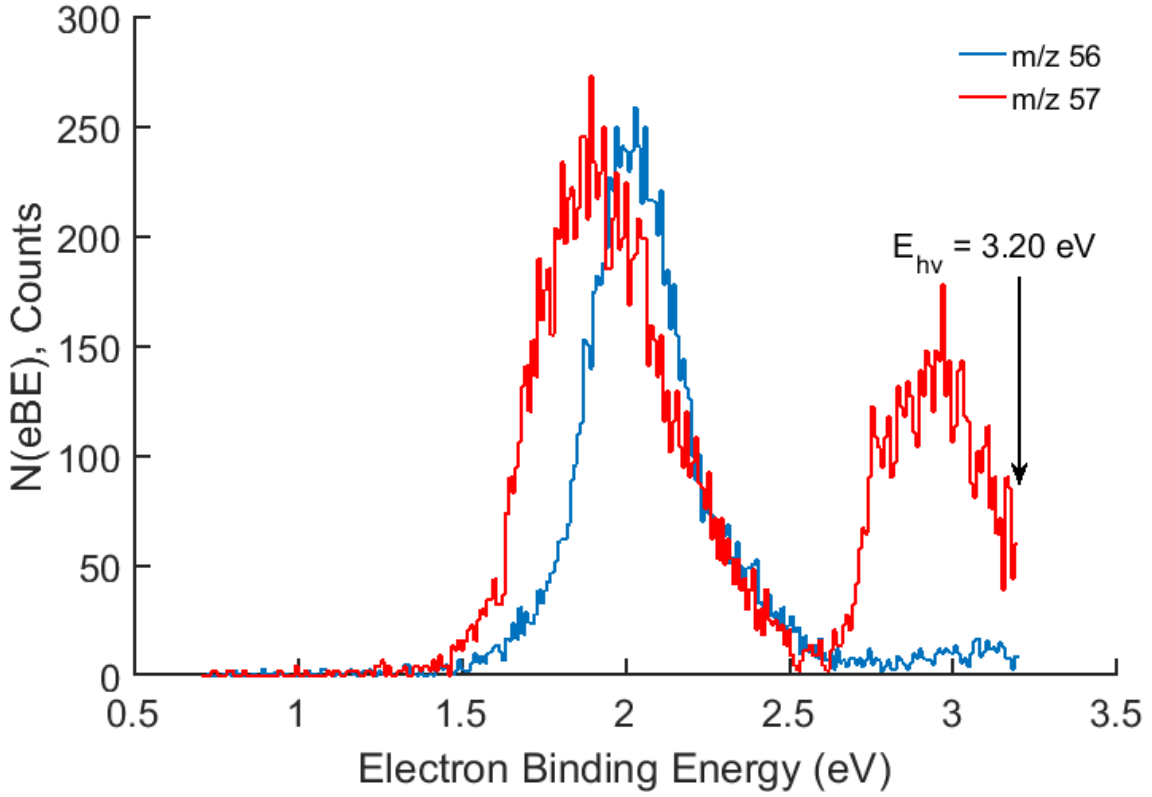

Figure 3.1. A comparison of photoelectron spectra for m/z 56 (blue) and m/z 57 (red) anions recorded in this study in coincidence with stable neutral products at E_{hv} = 3.20 eV.

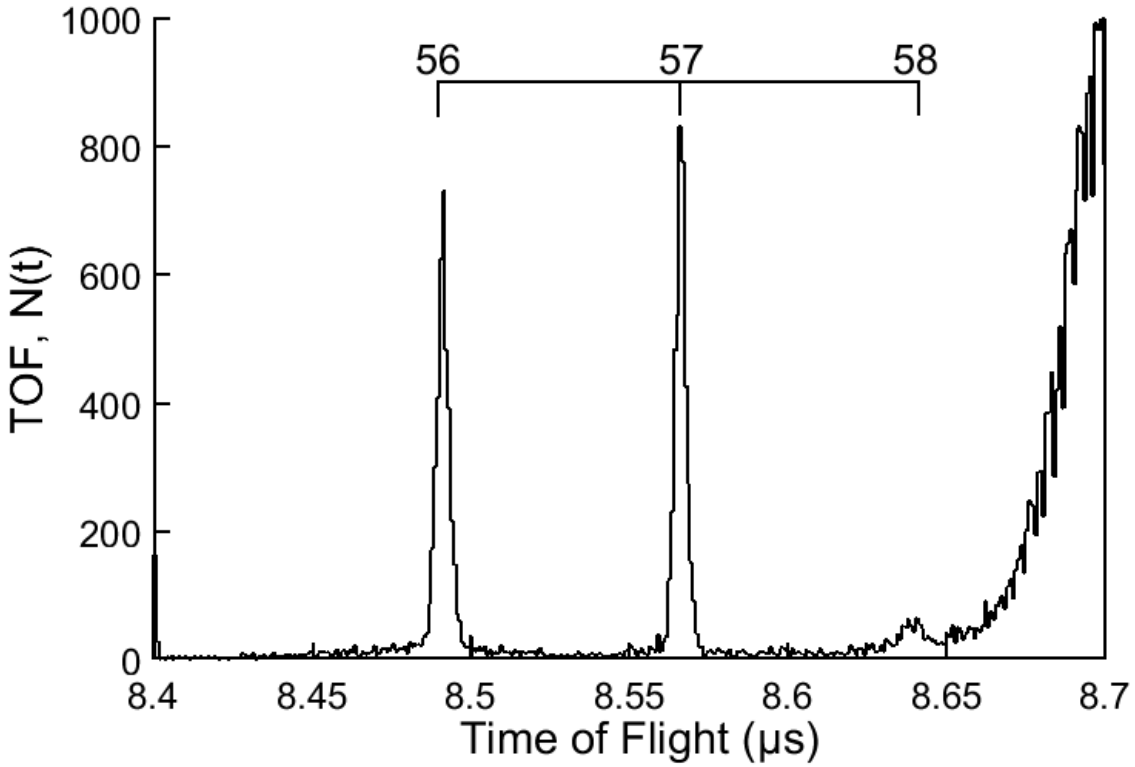

Figure 3.2. Neutral particle TOF spectrum for m/z 56, 57, 58 and the onset of m/z 60 at $E_{h\nu}$ = 3.20 eV. Sharp peaks correspond to stable neutral products, and a very minor dissociation channel can be seen as the broad base around m/z 56.

417(15) cm^{-1} vibrational progression was the evidence given for the 0.5 ns lifetime assignment. The AEA for HOCCO was reported to be 1.763(6) eV consistent with Figure 3.3(a).[13] Refs. 11 and 13 also reported energetics for OCCO using the CCSD/aug-cc-pVTZ level of theory that gave calculated vertical detachment energies similar to the experimental results, as well as Franck-Condon simulations of the spectra. However, the $OCCO^-$ anion structure required a significant geometry change to reproduce the spectra in ref. 13 as compared to the optimized geometry reported. Most notably, the OCC bond angle was changed 6.1 degrees in the anion structure so the OCCO Franck-Condon simulation would fit the experimental results. To simulate the m/z 57 spectrum, two structural isomers were invoked. The first isomer required a rearrangement of the glyoxal precursor, resulting in a hydrogen atom attached to a terminal oxygen. The second more energetically stable isomer would result from a single deprotonation of glyoxal. Based on the reported calculations, the spectrum was primarily attributed to the higher energy isomer. Because the justification of both the OCCO and HOCCO spectra required significant changes in the anion geometries, as well as the counterintuitive assignment to the higher energy isomer in the latter case, the calculations from ref. 11 and 13 would appear to be suspect.

3.2. Experimental Methods

Synthesis of the $OCCO^-$ anion was attempted using glyoxal with nitrous oxide as a precursor, as described by Sanov and co-workers.[13] The glyoxal solution (Acros Organics, Inc., 40 wt. % in water) was dried for 18 hours using 3 Å molecular sieves in a 1:1 ratio while being chilled to 4° C. This solution was then extracted, placed in a sample holder and heated to 45° C using N_2O as a carrier gas. Anions were generated in a pulsed supersonic expansion and injected into a cryogenic octopole accumulation trap (COAT).[12]

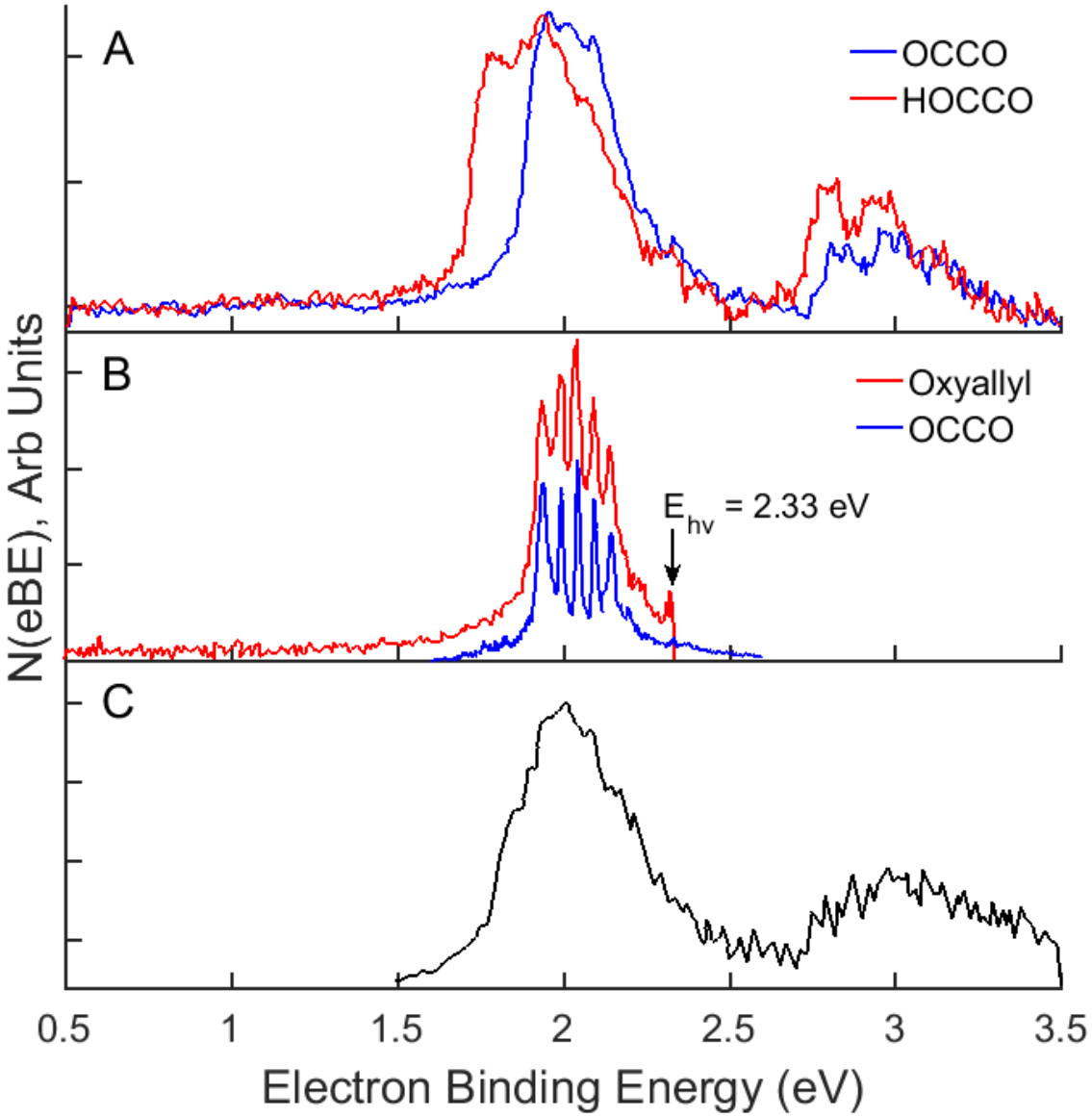

Figure 3.3. **A)** *Red trace:* $OCCO^-$ data reported in ref. 13. *Blue trace:* $HOCCO^-$ data reported in ref. 13, both at E_{hv} = 3.49 eV (adapted from Fig. 1b in ref. 13). **B)** *Red trace*: m/z 56 $OCCO^-$ data at E_{hv} = 2.33 eV (adapted from Fig. 1a in ref. 11). *Blue trace:* Photoelectron spectrum of $C_3H_4O^-$ at E_{hv} = 3.53 eV, assigned to the X^1A_1 and a^3B_2 states of the oxyallyl diradical. (adapted from Fig. 3a in ref. 18) **C)** Ref. 18 data for m/z 56 oxyallyl diradical collected at E_{hv} = 3.49 eV. (adapted from Fig. 7c in ref. 19).

The ions were collisionally cooled with buffer gas (80:20 He/H_2 mix) at ~17 K for 40 ms before being accelerated to 7 keV, re-referenced to ground with a potential switch, and separated by time of flight. The species of interest were then injected into a cryogenic electrostatic ion beam trap (EIBT) where they oscillate for 100 ms while being crossed with a 1037 Hz picosecond pulsed Ti:Sapphire regenerative amplifier (Clark-MXR CPA-2000) at a photon energy of 3.20 eV.[16] Photoelectrons were extracted orthogonal to the ion beam and focused onto a time and position sensitive detector, allowing determination of the photoelectron recoil velocity and the electron kinetic energy. The neutral particles were collected in coincidence with the electrons using a multi-particle time and position sensitive detector on the ion beam axis 1.31 m from the laser interaction region. All figures are plotted in electron binding energy (eBE) which is defined as eBE = $E_{h\nu}$ – eKE.

3.3. Computational Methods

A refined calculation of the AEA of the $^3\Sigma^-$ state of OCCO that goes beyond the CCSD level used in ref. 13 has also been carried out with geometries for the anion and the neutral triplet optimized at aug-cc-pVTZ/CCSD(T) level of theory. Single point energetics were calculated at aug-cc-pVDZ, aug-cc-pVTZ, aug-cc-pVQZ and aug-cc-pV5Z. SCF energies were extrapolated using $E_x=E_{CBS}=A^{9BX}$ and CCSD (T) correlation energies were calculated using $E_x = E_{CBS} - \frac{A}{x^3}$. The total electronic contribution to the AEA was determined to be 1.666 eV. The zero point energies for the anion and the neutral were calculated to be 2610.5 cm^{-1} and 3021.5 cm^{-1}, respectively. This resulted in a 0.051 eV contribution to the AEA. The calculated values for each of these energies at the optimized geometries can be seen in Table 3.1.

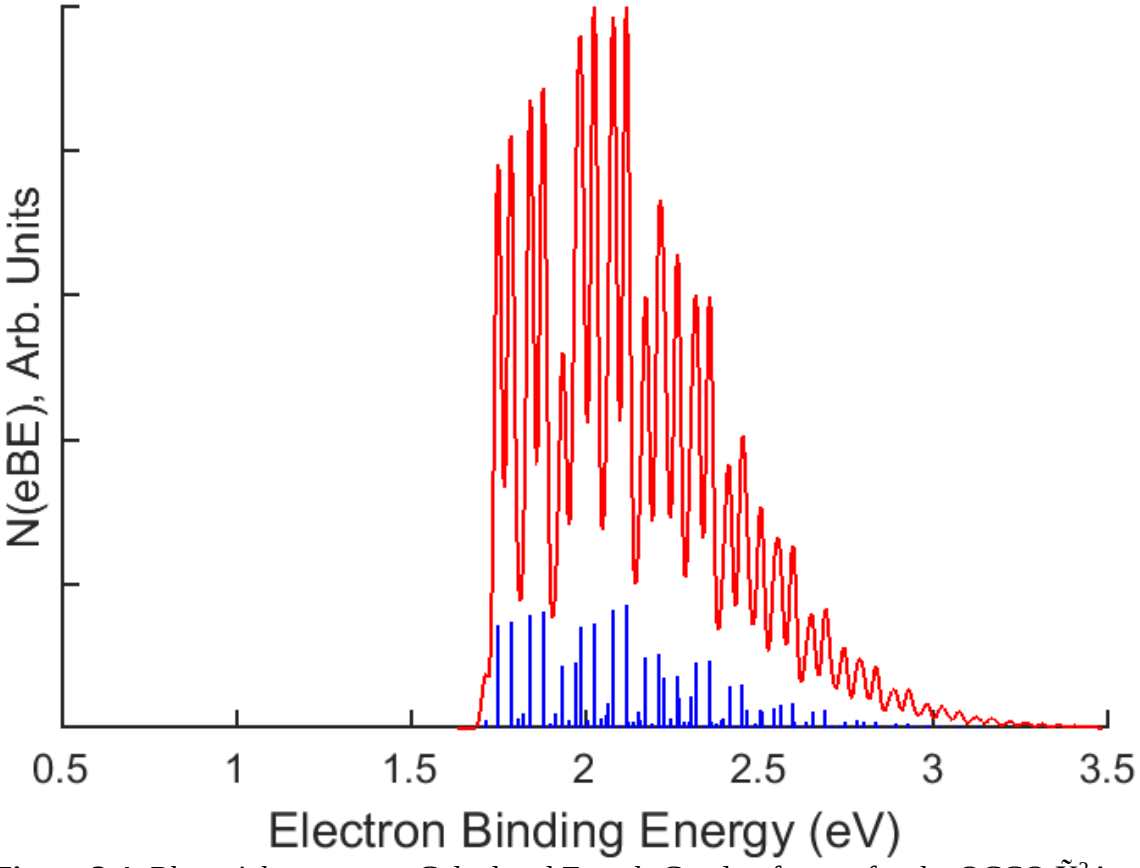

Figure 3.4. *Blue stick spectrum:* Calculated Franck-Condon factors for the OCCO $\tilde{X}^2A_u$ — $\tilde{X}^3\Sigma^-$ transition at the CCSD(T) level. *Red trace:* Simulated photoelectron spectrum using a 25 meV full-width-at-half-maximum convolution.

Table 3.1. Single-point energetics (XZ refers to aug-cc-pVXZ). SCF energies are extrapolated using $E_X = E_{CBS} = A^{9BX)}$; CCSD (T) correlation energies calculated using $E_X = E_{CBS} - \frac{A}{x^3}$.

	SCF		**CCSD(T)**	
	Triplet	*Anion*	*Triplet*	*Anion*
TZ	-225.4616133	-225.4690181	-0.771610737	-0.8238795923
QZ	-225.4759378	-225.4828907	-0.8140266717	-0.8674059768
5Z	-225.4791397	-225.4860112	-0.8284966865	-0.8823660168
extrap	-225.4800614	-225.489168	-0.8436783415	-0.8980617965

The result of these calculations suggests that the AEA is significantly lower than the 1.936(8) eV given in ref. 11, with a value of 1.717 eV being obtained at the CCSD(T) level (as extrapolated to the basis set limit). A conservative estimate of the uncertainty of this calculation is ≤0.02 eV. In addition, a Franck-Condon simulation of the photoelectron spectrum was performed, and the result of this is shown in Figure 3.4. In contrast to the spectra shown in Figure 3.3(a) and 3.3(b), the simulated spectrum of the $^3\Sigma^-$ state contains extended vibronic structure involving mostly the trans bend and CC stretching modes, consistent with the substantial geometry change between the anion and the $^3\Sigma^-$ neutral state.

3.4. Discussion

The observation of stable species at m/z 56 and 57 and the noted inconsistencies in the calculations forced a re-examination of the OCCO assignment. Reviewing the literature, the oxyallyl diradical, C_3H_4O, produced by photodetachment of the oxyallyl anion is found to be the best assignment for the m/z 56 spectra reported here and in ref. 11.[17-19] Lineberger and co-workers reported photoelectron spectra of this anion at $E_{h\nu}$ = 3.53 eV.[17] The spectrum reported for the oxyallyl anion and the $OCCO^-$ spectrum at $E_{h\nu}$ = 2.33 eV reported in ref. 11 are compared in the electron binding energy (eBE) spectra in Figure 3.3(b). The AEAs, the observed vibrational peak spacings, intensities and profiles are in striking agreement, as seen in Table 3.2. Although the vibrational progression was not observed in the lower-resolution spectrum collected in the present study at $E_{h\nu}$ = 3.20 eV, the features that were observed have the same signature as the spectrum reported in ref. 11 at $E_{h\nu}$ = 3.49 eV. Specifically, the intense peak at eBE = 2.00 eV, previously assigned to the OCCO triplet state is assigned here to photodetachment of $C_3H_4O^-$. Ref. 11

Table 3.2. Comparison of published data for the neutral species derived from photoelectron spectra at m/z 56 ($C_3H_4O^-$ and $OCCO^-$) and m/z 57 ($C_3H_5O^-$ and $HOCCO^-$).

	Oxyallyl Diradical ($\tilde{X}^1A_1$) [18]	**Ethylenedione** [11]
Adiabatic Electron Affinity	1.942 ± 0.010 eV	1.936 ± 0.008 eV
Vibrational Frequency	405 ± 10 cm^{-1}	417 ± 15 cm^{-1}
	Acetone Enolate Radical ($\tilde{X}^2A''/A^2A'$) [20]	**Ethynediolide** [13]
Adiabatic Electron Affinity	1.760 ± 0.004 eV	1.763 ± 0.006 eV
Excited State	2.786 ± 0.012 eV	2.8 eV

also attributed a broad band spanning the triplet state as a dissociative OCCO singlet state. A similar broad feature was also reported in the oxyallyl spectrum and assigned in ref. 18 to a structural isomer, the acetylcarbene radical. Because of the many vibrational modes and a large geometry change between the anion and the neutral, the acetylcarbene spectrum is not vibrationally resolved.[18] With this information, the OCCO triplet state assigned in ref. 11 should be reassigned to the oxyallyl diradical, and the first OCCO singlet state as the acetylcarbene radical, although the latter assignment is perhaps more tentative.

Photodetachment of the oxyallyl anion was also studied in ref. 18 reporting Franck-Condon simulations for the three low-lying electronic states of oxyallyl. The photoelectron spectrum they reported at $E_{h\nu}$ = 3.49 eV is shown in Figure 3.3(c).[19] The excited state of oxyallyl observed in the spectrum reported in ref. 18 matches well with the spectral features assigned to the S_2 and S_3 states of OCCO in ref. 11. In contrast, the excited state was observed with only a very low intensity in the present study at $E_{h\nu}$ = 3.20 eV. Possible explanations for the difference in the excited state contributions at these photon energies are the energy dependence of the photodetachment cross section and the possible role played by anionic resonances in the production of the excited state. Given the information in ref. 18 and the calculations in ref. 19, the two higher singlet states of OCCO, S_2 and S_3, are reassigned to the excited state of oxyallyl.

Now that the oxyallyl diradical has been determined to be the correct assignment of the m/z 56 data, the m/z 57 data can be compared to spectra in the literature. The m/z 57 photoelectron spectrum has the same features as both the acetone enolate (also known as methyl vinoxide) spectrum reported in refs. 18 and 20, as well as the HOCCO spectra reported in ref. 13. The AEA and excited state energetics for acetone enolate radical

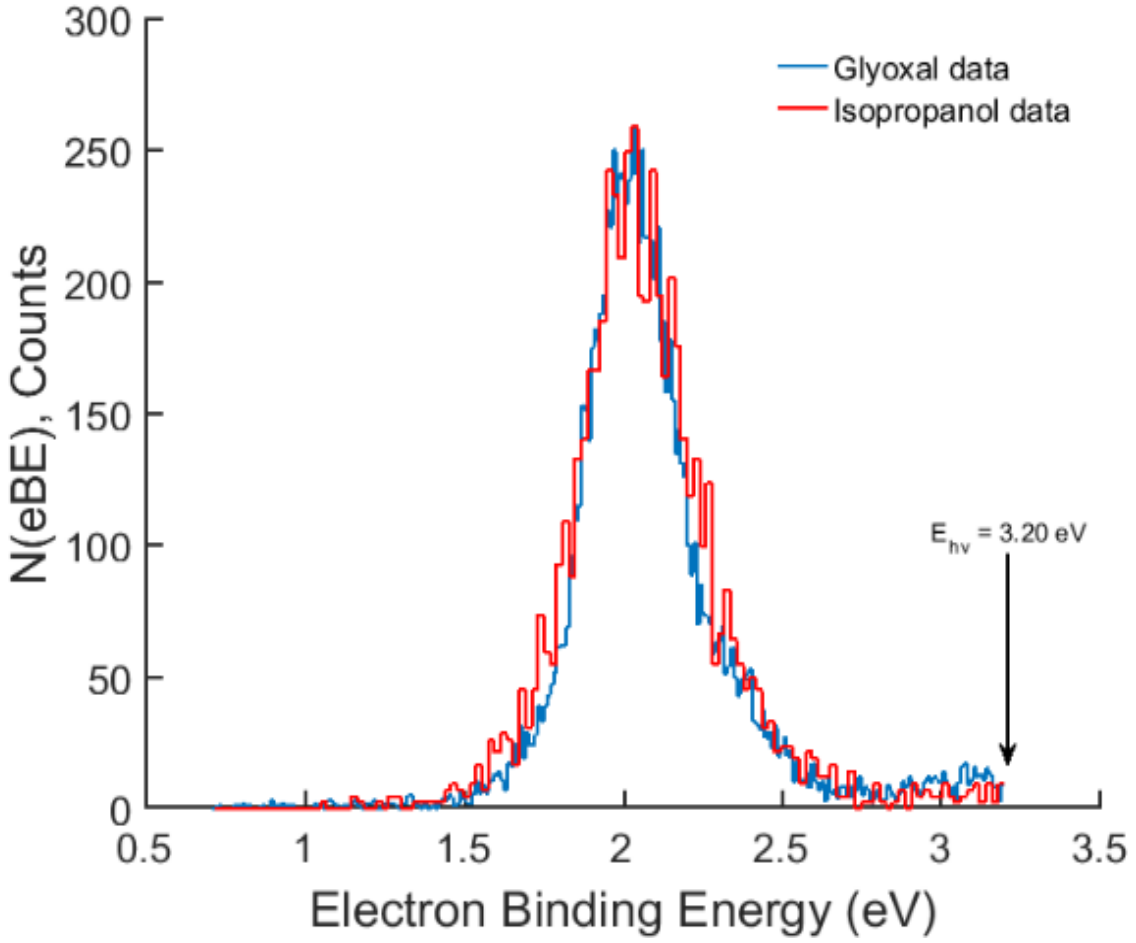

Figure 3.5. A comparison of photoelectron spectra for m/z 56 with ion synthesis of glyoxal/N_2O (red) from ref. 6 and isopropanol/N_2O (blue) from ref 17 and 18 recorded at E_{hv} = 3.20 eV.

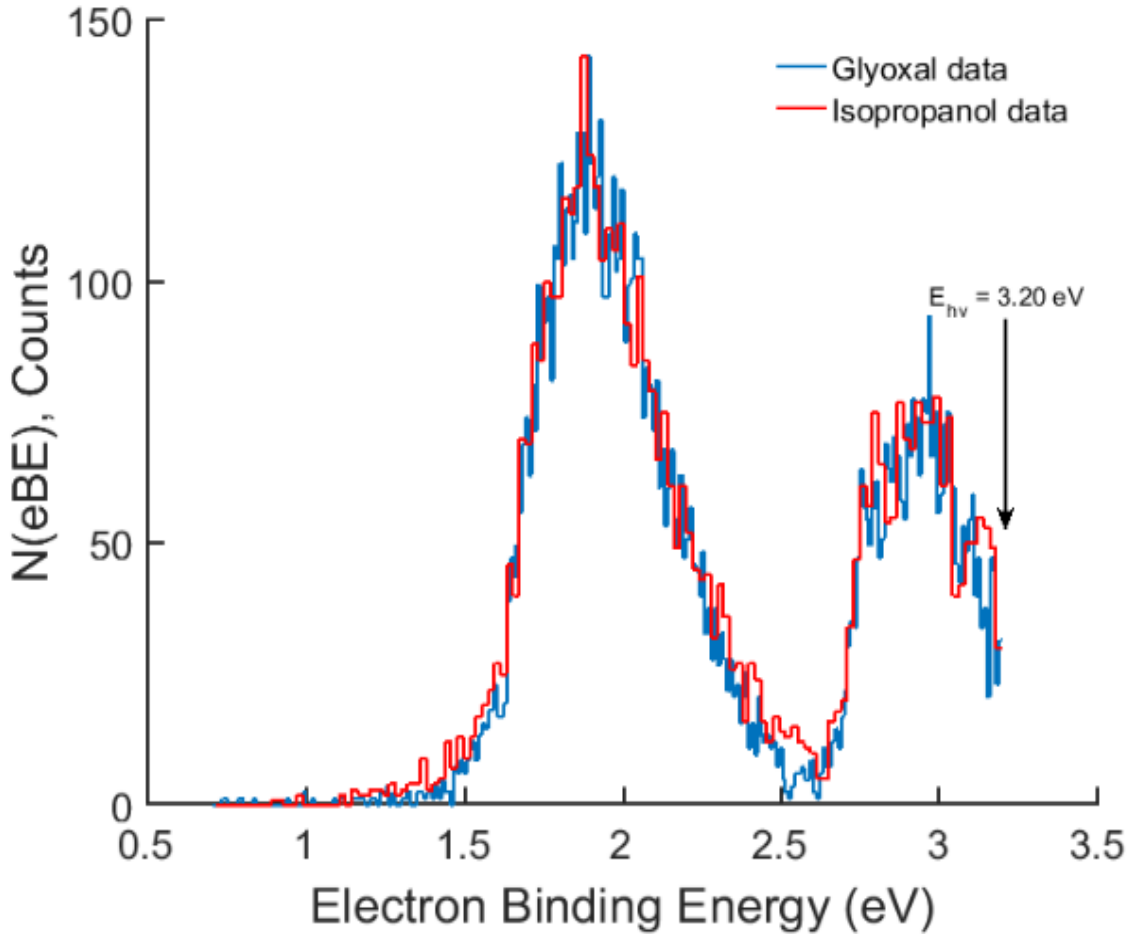

Figure 3.6. A comparison of photoelectron spectra for m/z 57 with ion synthesis of glyoxal/N_2O (red) from ref. 6 and isopropanol/N_2O (blue) from ref 17 and 18 recorded at $E_{h\nu}$ = 3.20 eV.

reported in ref. 18 are identical to the data reported in ref. 13, as seen in Table 3.2. In the present study, photodetachment to both the ground and excited states were observed to produce a stable neutral species, consistent with the previous study of acetone enolate conducted in this laboratory using PPC spectroscopy.[20] The peak in Figure 3.1 at eBE =1.90 eV measured in coincidence with m/z 57, is therefore attributed to photodetachment of the acetone enolate anion to the ground state of the corresponding radical, and the feature above eBE = 2.61 eV is assigned to the first excited state.

Further experiments were conducted in order to confirm that oxyallyl and the acetone enolate radical were the correct assignments of the m/z 56 and 57 photoelectron spectra. The ion synthesis reported in ref 17 and 18 using a pulsed discharge on an isopropanol/N_2O mixture was used, and Figures 3.5 and 3.6 show comparisons of the isopropanol method to the original data using the method in ref. 11 of glyoxal/N_2O. Both methods of ion synthesis had identical photoelectron spectra, further confirming the mass assignment of the oxyallyl radical and the acetone enolate radical. The m/z 56 and m/z 57 in the isopropanol data were also measured in coincidence with stable photoneutrals. The time-of-flight for the isopropanol method is shown in Figure 3.7. The stable and dissociative channels of m/z 56 were also observed in this experiment, confirming that both channels are attributed to oxyallyl. Using an ion synthesis of deuterated ispropanol/N_2O a shift of the m/z 56 and 57 to m/z 60 and 62 respectively was observed, further confirming the assignments of oxyallyl and acetone enolate. These results confirm that the features assigned in ref. 13 to the ground and excited states of ethylenedione and ethynediolide should be reassigned to the ground and first excited states of oxyallyl and the acetone enolate radical, respectively.

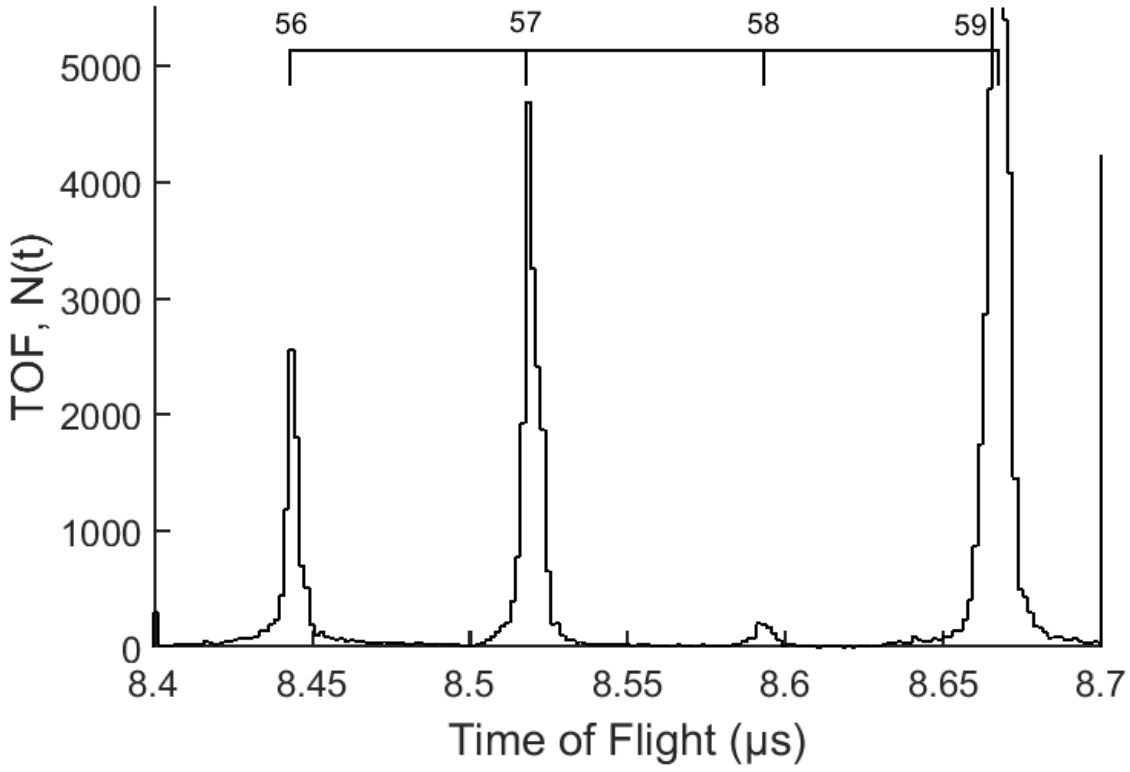

Figure 3.7. Neutral particle TOF spectrum for m/z 56, 57, 58 and 59 at $E_{h\nu}$ = 3.20 eV for the isopropanol/N_2O ion synthesis. Both stable and dissociative m/z 56 are observed in this TOF, as well as the glyoxal/N_2O ion synthesis.

3.5. Conclusion

In conclusion, the long-lived states of ethylenedione, sought experimentally for over a century, remain unobserved. Given the overwhelming evidence from this study, previous theory and the literature, we have found that the spectra for ethylenedione and ethylenediolide reported in refs. 11 and 13 should be reassigned to the oxyallyl diradical, C_3H_4O, and the acetone enolate radical, C_3H_5O. These results show that pulsed discharge ion sources can cause significant structural rearrangement and the formation of a wide range of structural isomers for small organic anions. These results add to the history of frustration that has accompanied the search for ethylenedione and opens the way for further efforts.

This chapter is adapted from the following publication, in which the dissertation author is the primary author and the dissertation advisor is the corresponding author. Lunny, K. G., Benitez, Y., Albeck, Y. Strasser, D., Stanton, J. F., Continetti, R. E.; "Spectroscopy of Ethylenedione and Ethynediolide: A Reinvestigation", *Angewandte Chemie International Edition,* 2018, 57, 5394.

3.6. References

1. Chen, H.; Holmes, J. L., The generations of OC_2O^+ and OC_2O and a Study of the Ionized OC_3O and C_2O by Tandem Mass Spectrometry. *Int. J. Mass Spectrom. Ion Processes* **1994,** *133*, 111.

2. Dawson, D.; Chen, H.; Holmes, J. L., Letter: On the Structure of $C_2O_2^+$ Generated from $C_2O_2^+$. *European Journal of Mass Spectrometry* **1996,** *2*, 373

3. Lewars, E. G., *Modeling Marvels*. Berlin, 2008.

4. Maier, G.; Reisenauer, H. P.; Ruppel, R., 2-Thioxoethen-1-on (OCCS). *Angew. Chem. Int. Ed.* **1997,** *109,* 1972.

5. Suelzle, D.; Terlouw, J.; Schwarz, H., Experimental Evidence for the Existence of Neutral and Ionized Thioxoethylenone in the Gas Phase. *J. Am. Chem. Soc.* **1990,** *112* (2), 628-630.

6. Birney, D.; Berson, J., Norborna-2,5-dien-7-one: A Covalent Benzene-Carbon Monoxide Adduct. A New Point on the Cycloreversion Structure-Reactivity Correlation Curve. *J. Am. Chem. Soc.* **1985,** *107* (15), 4553-4554.

7. Birney, D.; Berson, J., Synthesis of the Covalent Benzene-Carbon Monoxide Cycloadduct, Norborna-2,5-dien-7-one. *Tetrahedron* **1985,** *42* (6).

8. Dean, D. L.; Hart, H., New Enone Photochemistry. *J. Am. Chem. Soc.* **1972,** *94* (2).

9. Staudinger, H.; Anthes, E., Oxalylchlorid. V.: Über Oxalylbromid und Versuche zur Darstellung von Di-Kohlenoxyd. *Ber, Dtsch. Chem. Ges.* **1913,** *46.*

10. Schroder, D.; Heinemann, C.; Schawrz, H.; Harvery, J.; Dua, S.; Blanksby, S.; Bowie, J., Ethylenedione: An Intrinsically Short-Lived Molecule. *Chem. Eur. J.* **1998,** *4* (12).

11. Dixon, A.; Xue, T.; Sanov, A., Spectroscopy of Ethylenedione. *Angew. Chem. Int. Ed.* **2015,** *54* (127), 8764-8767.

12. Shen, B.; Benitez, Y.; Lunny, K. G.; Continetti, R. E., Internal Energy Dependence of the Photodissociation Dynamics of O_3^- Using Cryogenic Photoelectron-Photofragment Coincidence Spectroscopy. *J. Chem. Phys.* **2017,** *147*, 094307.

13. Dixon, A.; Xue, T.; Sanov, A., HOCCO versus OCCO: Comparative Spectroscopy of the Radical and Diradical Reactive Intermediates. *The Journal of Chemical Physics* **2016,** *144*.

14. Thomas, R. J.; DeLeeuw, B.; O'Leary, P.; Schaefer, H. F. I.; Duke, B.; O'Leary, B., The Ethylenedione Anion: Elucidation of the Intricate Potential Energy Hypersurface. *The Journal of Chemical Physics* **1995,** *102* (16).

15. Talbi, D.; Chandler, G. S., Extensive ab Initio Study of the C_2O_2, C_2S_2, and C_2OS Systems: Stabilities and Singlet-Triplet Energy Gaps. *J. Phys. Chem. A* **2000,** *104*.

16. Johnson, C. J.; Shen, B. B.; Poad, B. L. J.; Continetti, R. E., Photoelectron-Photofragment Coincidence Spectroscopy in a Cryogenically Cooled Linear Electrostatic Ion Beam Trap. *Rev. Sci. Instrum.* **2011,** *82*, 105105.

17. Ichino, T.; Villano, S.; Gianola, A.; Goebbert, D.; Velarde, L.; Sanov, A.; Blanksby, S.; Zhou, X.; Hrovat, D.; Borden, W. T.; Lineberger, W. C., The Lowest Singlet and Triplet States of the Oxyallyl Diradical. *Angew. Chem. Int. Ed.* **2009,** *48*.

18. Ichino, T.; Villano, S.; Gianola, A.; Goebbert, D.; Velarde, L.; Sanov, A.; Blanksby, S.; Zhou, X.; Hrovat, D.; Borden, W. T.; Lineberger, W. C., Photoelectron Spectroscopic Study of the Oxyalyl Diradical. *J. Phys. Chem. A* **2011,** *115*, 1634.

19. Mozhayskiy, V.; Goebbert, D.; Velarde, L.; Sanov, A.; Krylov, A., Electronic Structure and Spectroscopy of Oxyallyl: A Theoretical Study. *J. Phys. Chem. A* **2010,** *114*.

20. Alconcel, L.; Deyerl, H. J.; Continetti, R. E., Effects of Alkyl Substitution on the Energetics of Enolate Anions and Radicals. *J. Am. Chem. Soc.* **2001,** *123* (50), 12675-12681.

Chapter 4: Dissociative Photodetachment of the Oxyallyl Anion in the Near Ultraviolet via Triplet-Singlet Intersystem Crossing

4.1. Introduction

Diradicals are transient species that play important roles in a number of reaction mechanisms.[1-3] These intermediates are a class of molecules with two degenerate or near-degenerate molecular orbitals that can be difficult to study due to their highly reactive nature.[3] An example of a true diradical is trimethylenemethane $CH_2C(CH_2)CH_2$, a ground state triplet that is a model system for studying this class of short lived species.[4, 5] The oxyallyl diradical, C_3H_4O, is a structural analog of trimethylenemethane with one of the CH_2 groups replaced by an oxygen atom.[6] Lone pair interactions with the oxygen atom stabilize the C_{2V} structure on the singlet surface and splits the degeneracy of the $^1A_1$ and $^3B_2$ orbitals. This has been predicted by theory to result in a ~0.06 eV separation between the singlet and triplet diradical electronic states.[6, 7] While these electronic states have been observed experimentally with photoelectron spectroscopy, the near degeneracy has made assignment of the individual states difficult without the support of high-level theory.[6-8] Photoelectron-photofragment coincidence (PPC) spectroscopy provides an alternative method to study transient species and resolve the photoelectron spectra of different electronic states based on the dissociation dynamics of the resulting neutral products. This has been employed for the oxyallyl diradical system in order to separate the nearly degenerate low-lying triplet and singlet states as well as a higher lying $^3B_1$ state through experimental measurements.

Many experimental and theoretical studies have been conducted on the oxyallyl system.[6-13] Schalley *et al.* have done extensive mapping of the isomers of C_3H_4O on the potential energy surface of the anion as well as the neutral singlet and triplet surfaces. Neutralization-reionization experiments were used to confirm some of the relative energy states predicted by theory.[9] The ground states for the oxyallyl anion as well as the high energy $^2B_1$ anion were calculated and are shown in Figure 4.1. On the neutral surface, cyclopropanone and the barrier to dissociation were reported, with the barrier determined to be 2.3 eV above the stable CO + C_2H_4 dissociation channel.[9] The heat of formation of cyclopropanone has been determined through fluorescence yield experiments.[14] Schalley *et al*. were unable to find a C_{2v} singlet structure for oxyallyl, and predicted that the open ring structure is a transition state for the cyclization of cyclopropanone. However, they were able to calculate a stable C_{2v} triplet state and observe dissociation of the corresponding cation through neutralization-reionization experiments.[9]

Anion photoelectron spectroscopy revealed nearly degenerate $^3B_2$ and $^1A_1$ neutral states, as well as a $^3B_1$ excited state, and determined an adiabatic detachment energy (ADE) to the singlet state of 1.94 eV at E_{hv}= 3.53 eV.[6, 8] The ADE to the $^3B_2$ state was inferred from Franck-Condon calculations to be ~2.00 eV while the higher-lying $^3B_1$ state was characterized by ADE = 2.823 eV.[6] This was further confirmed by Mozhayskiy *et al.* who replicated the photoelectron spectrum as well as conducted high-level theory calculations to reproduce the experimental results.[7] These calculations were in agreement with the previous photoelectron spectroscopy study that the C_{2V} structure of the singlet state was 0.06 eV lower in energy than the C_{2v} $^3B_2$ state. While this C_{2v} structure was not found to be a minimum on the singlet surface, it was observed through photoelectron spectroscopy

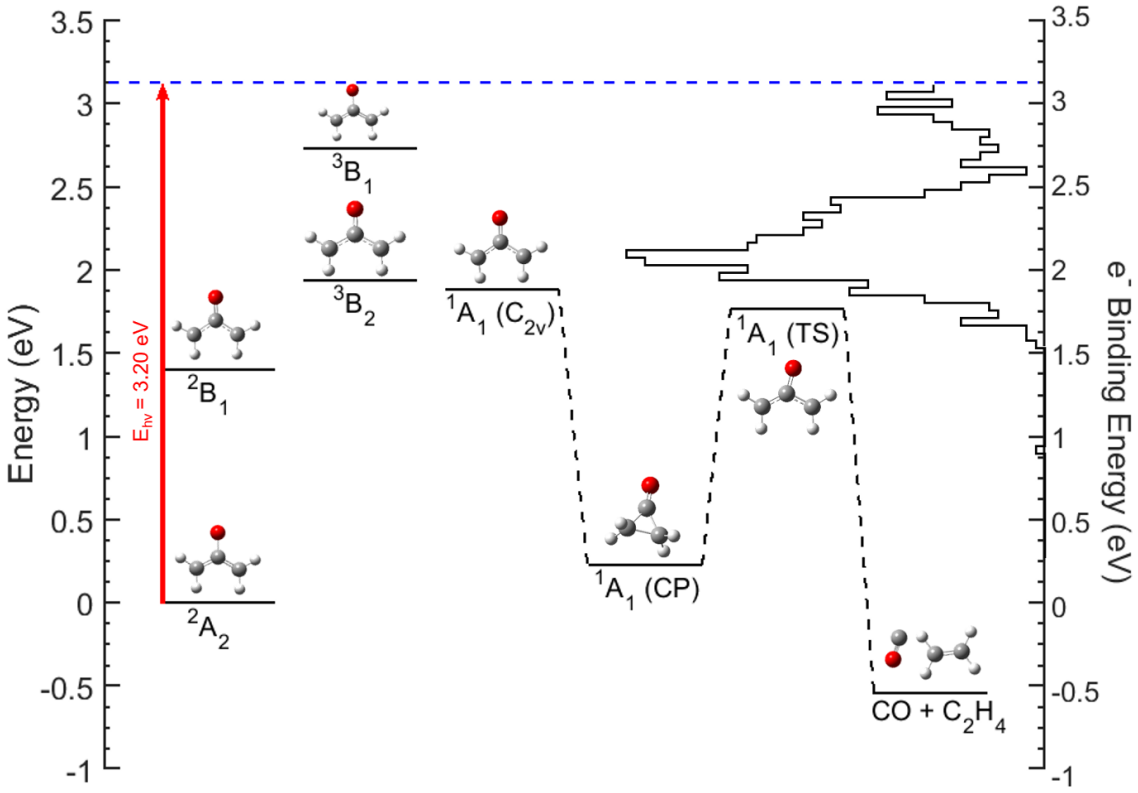

Figure 4.1. Energetics for the oxyallyl system plotted with the photoelectron spectrum measured in coincidence with two neutral fragments. The neutral electronic states are shown as well as the theoretical predictions about the cyclopropanone structure, and transition states for the neutral surface.[6,7,9]

and predicted to have a lifetime of ~170 fs, due to spectral broadening.[6, 7] The C_{2v} singlet state is predicted to have a barrier-less transition to cyclization forming the more stable structure of cyclopropanone.[7] Mozhayskiy *et al.* were able to calculate the structures in the Franck-Condon region of the singlet transition state as well as the two triplet states accessible at a photon energy of 3.49 eV. The difference in geometries between the singlet and triplet states is seen most dramatically in the difference in the CCC bond angle. While both the $^3B_2$ and $^3B_1$ states have bond angles of 121.3˚, the singlet state is predicted to have a bond angle of 110.4˚, with excitation of the ν_7 C-C-C bending mode observed in the photoelectron spectrum for both the $^3B_2$ and $^3B_1$ states.[6, 7]

PPC spectroscopy is able to directly measure the dynamics for dissociative states produced by photodetachment of stable anions. Coincidence measurements allow separation of overlapping photoelectron spectra for stable and dissociative neutral product states. If two distinct dissociation mechanisms are observed for different electronic states, the corresponding photoelectron spectra can be disentangled. A previous publication on the oxyallyl system using PPC spectroscopy reported the photoelectron spectrum measured in coincidence with stable neutral radicals at a photon energy of 3.20 eV. This was found to be identical to the photoelectron spectrum of ethylenedione (C_2O_2) reported in the literature, leading to the reassignment of that spectrum to the oxyallyl diradical.[15, 16] Photophysics of the oxyallyl anion have also been studied at a photon energy of 1.60 eV using PPC spectroscopy, wherein excitation to a dipole bound state (DBS) on the singlet surface was observed ~0.3 eV below the photodetachment threshold. This resulted in observation of either delayed photoemission or dissociative photodetachment via a two photon process.[17] Using a photon energy of 3.20 eV, the ground $^1A_1$ state as well as the

two low-lying $^3B_2$ and $^3B_1$ states can be accessed. In the following, the dissociation dynamics for these states will be reported and discussed in terms of qualitative predictions based on earlier electronic structure calculations.

4.2. Experimental Methods

These experiments were conducted using a PPC spectrometer that has been described in detail previously.[18] Anions were generated using dried glyoxal solution (Acros Organics, Inc. 40% wt. in water), heated to 45˚ C with N_2O as a carrier gas. A pulsed supersonic expansion with a pulsed discharge at 10 Hz was used to generate ions, which were injected with a Wiley-McLaren time-of-flight spectrometer into a cryogenic octopole accumulation trap (COAT).[19] Inside COAT, the anions were collisionally cooled at 17 K with 80:20 He/H_2 buffer gas for 40 ms. After extraction from COAT, the ions were accelerated to 7 keV, re-referenced to ground with a potential switch and separated by time-of-flight for injection into the cryogenic electrostatic ion beam trap (EIBT).[20]

Once inside the EIBT, the ion packet oscillates for 100 ms while being crossed with a picosecond pulsed Ti:Sa regenerative amplifier (1037 Hz repetition rate, Clark-MXR CPA-2000, 1.2 ps, 400 μJ/pulse 775 nm fundamental) at a photon energy of 3.20 eV (388 nm). Multiple anions were produced simultaneously using this ion source. High-resolution mass separation is achieved by detection of the neutral products in coincidence due to the mass-dependent velocity and oscillation frequency of the anions in the EIBT. The difference in oscillation frequency allows for multiple species to be photodetached simultaneously.[21] Photoelectrons are extracted orthogonal to the ion beam and focused using velocity map imaging onto a time-and position-sensitive electron detector in order to

determine electron kinetic energy (eKE). The electron detector was calibrated using O_2^- giving a resolution of ΔeKE/eKE ~4%. The neutral particles that result from this photodetachment are no longer held by the potential of the EIBT, and travel from the interaction region 1.31 m in line with the original ion beam to impact a multi-particle time and position sensitive detector, which measures the kinetic energy release (KER). For dissociative events, the product mass distribution is measured for momentum matched neutral products. In the case of the dissociation of 56 amu, an equal product mass distribution was observed, peaking at 28 amu with a FWHM of 3 amu. The neutral detector was calibrated using O_4^- giving a resolution of ΔKER/KER ~10%.

4.3. Results

In this experiment, six distinct photoelectron spectra of either stable or dissociative molecules from 56 – 66 amu were collected and isolated based on the neutral particle time of arrival. The 56 amu data, assigned to the oxyallyl diradical, was measured in coincidence with predominately stable neutral This can be seen in the photoelectron spectra in Figure 4. 2, as well as the electrons measured in coincidence with the minor dissociation channel, accounting for ~10% of the overall signal. The stable photoelectron spectrum for the oxyallyl diradical was reported previously in the reassignment of the ethylenedione (C_2O_2) spectrum in the literature.[15, 16, 22] The present study examines the dissociative events and shows how they are related to production of the three lowest-lying states of the oxyallyl diradical. The oxyallyl diradical has also been studied using PPC spectroscopy at a photon energy of 1.60 eV.[17] The results of this have been discussed previously, but briefly, are the result of excitation to a dipole bound state (DBS) ~0.3 eV below threshold in the

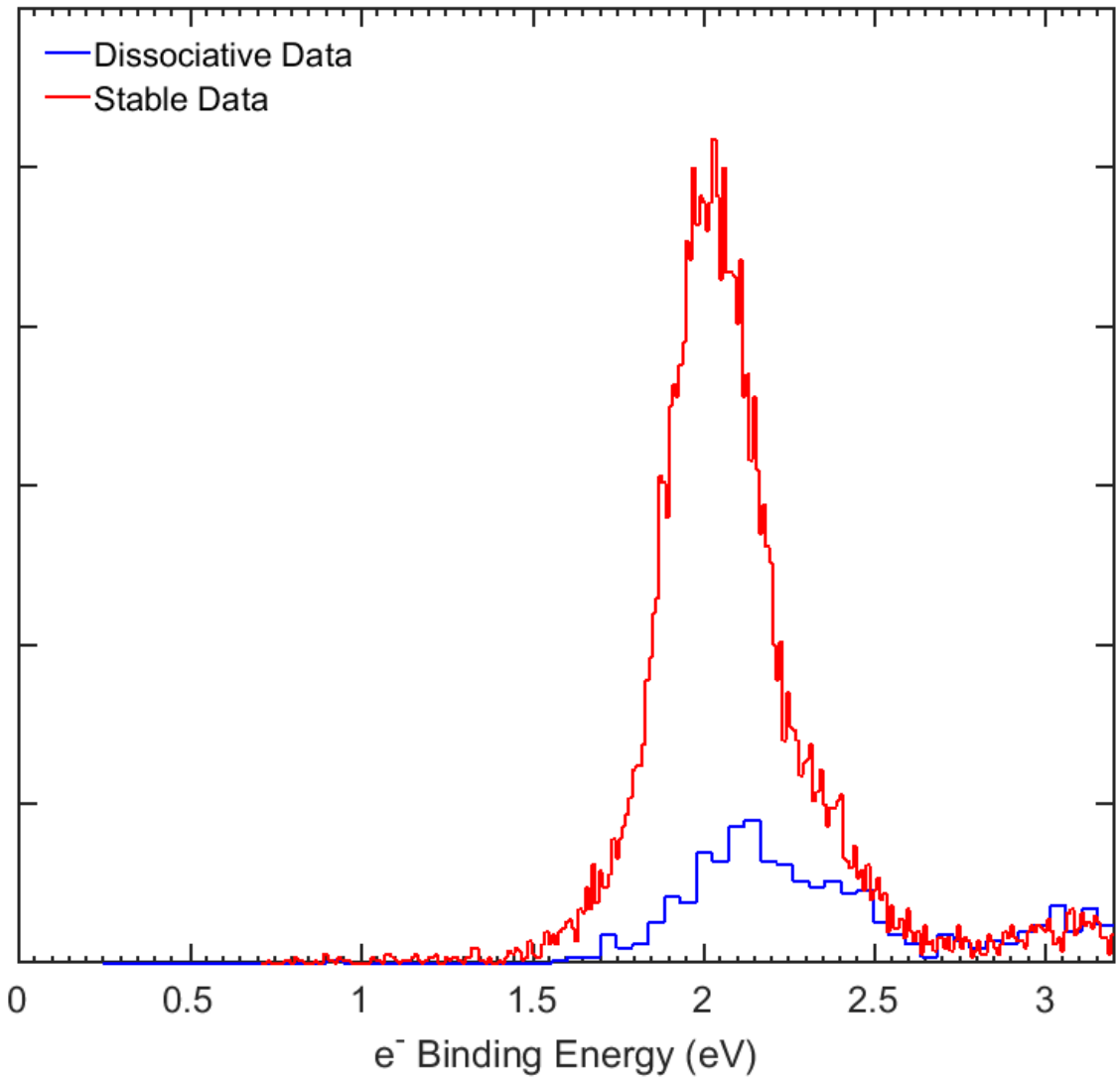

Figure 4.2. Photoelectron spectrum of the oxyallyl diradical collected at 3.20 eV. The red trace shows electrons in coincidence with a single stable neutral, while the blue trace shows electrons measured in coincidence with two neutral fragments of equal mass.

Franck-Condon region on the singlet surface. The DBS is supported by the zwitterionic character of the singlet state that results in a ~4.2 Debye dipole moment and was observed to undergo two processes, resulting in either stable or dissociative product channels. Because the DBS would also exhibit the same lifetime as the neutral singlet core in the process of cyclization, the stable product was attributed to a delayed photoemission process resulting in the production of neutral cyclopropanone. When a second photon interacts with the system during ring closure, the barrier to dissociation is overcome to the stable CO + C_2H_4 channel with significant vibrational excitation in the neutral products.[17]

For the spectrum collected at E_{hv}=3.20 eV, both the nearly degenerate $^3B_2$ and $^1A_1$ neutral states as well as a low-lying $^3B_1$ excited state are accessible through photodetachment. In the current study, stable products dominate for the two nearly degenerate states with only 10% of the overall photodetachment signal attributed to dissociation events. Figure 4.2 is an overplot of the electrons measured in coincidence with one stable product or two momentum-matched photofragments represented by the red and blue traces, respectively. The states accessed can be assigned to the nearly degenerate $^1A_1$ and $^3B_2$ states and an excited $^3B_1$ state. While the diradical states were significantly less populated in the dissociative channel, the excited triplet was equally likely to form either stable or dissociative product. The photoelectron spectrum that was measured in coincidence with two momentum-matched photofragments can also be seen in relation to the calculated energetics for the system in Figure 4.1.

The PPC spectrum measures the correlation between the KER and eKE, as shown in Figure 4.3. The coincidence spectrum reveals three distinct regions based on the eKE and differences in the energy partitioning among the dissociative products. These can be

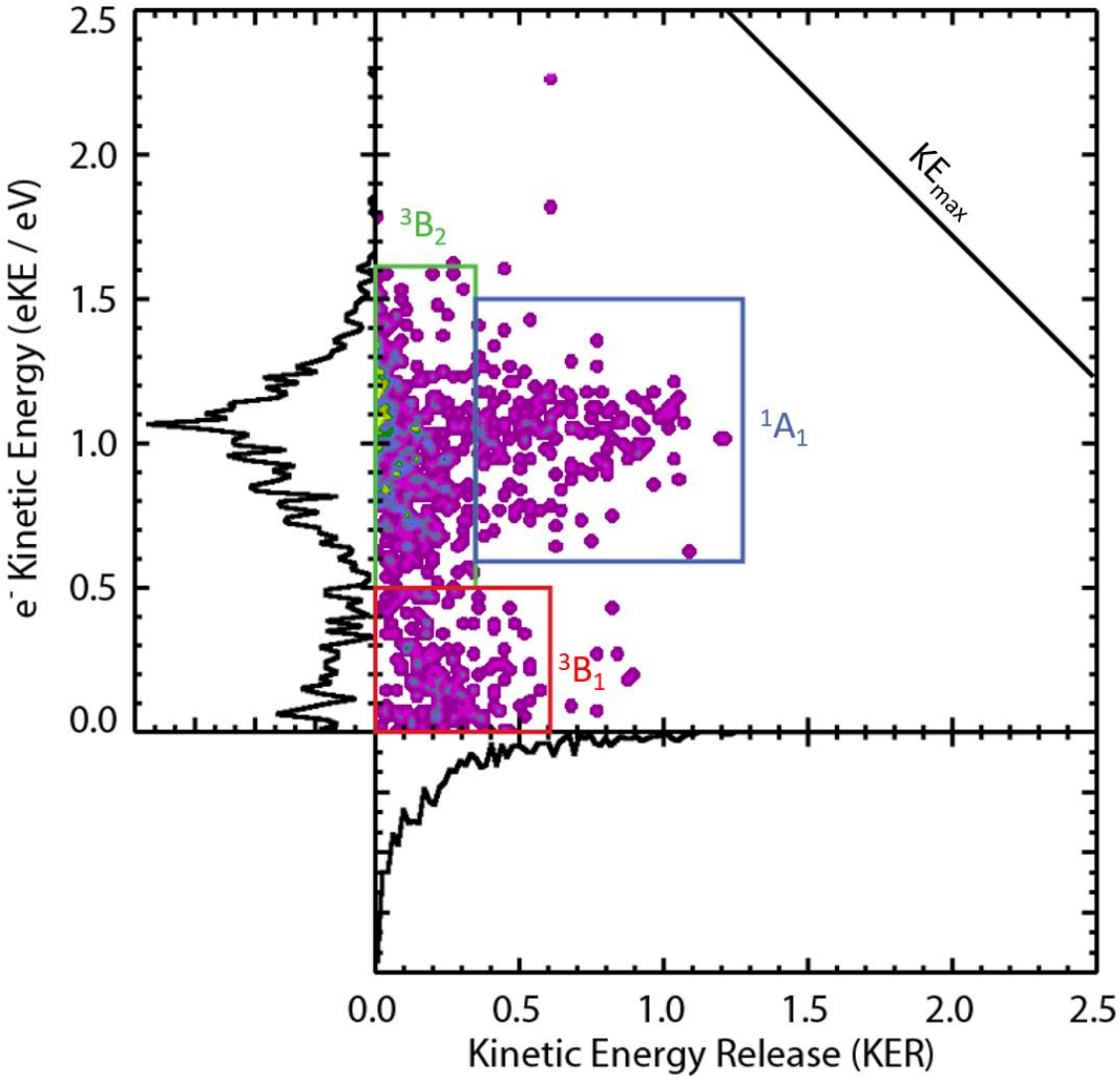

Figure 4.3. Coincidence plot for the dissociative data at 3.20 eV. Three channels can be seen, two with a low kinetic energy release, and one higher KER channel.

attributed to the three known electronic states of the neutral accessed at this photon energy (E_{hv}= 3.20 eV). Each of these channels can be seen in comparison to the theoretical kinetic energy maximum (KE_{max}), as shown in Figure 4.3. While the excited $^3B_1$ electronic state spans a distinct portion of the photoelectron spectrum, the two diradical states overlap in the same eKE regime. The photoelectron spectrum for the dissociative data agrees with the photoelectron spectrum measured in coincidence with one stable product in the previous above threshold PPC study. It has not been possible to isolate these nearly degenerate states in previous photodetachment experiments. However, when measured in coincidence with neutral fragments, even though the eKE resolution is low, the distinct dissociation dynamics allow the states to be distinguished using the relative photofragment KER. This allows for the photoelectron spectra to be resolved based on neutral product energy partitioning. Figure 4.4 shows the total photoelectron spectrum measured in coincidence with dissociative products, as well as the distinct photoelectron spectra for the nearly degenerate $^1A_1$ and $^3B_2$ electronic states. For the $^3B_2$ state, the KER limits were 0-0.35 eV, with eKE limits of 0.5-2.5 eV. For the $^1A_1$ state, the KER limits were 0.35-2.5 eV and eKE limits of 0.5-2.5 eV. For the $^3B_1$ state, the KER limits were 0-2.5 eV, and eKE limits of 0-0.5 eV. When the two diradical states were disentangled, it was determined that there was a 0.06 eV separation between the ADE of the $^1A_1$ state and ADE of the $^3B_2$ state, in excellent agreement with prior theory and experiment.

4.4. Discussion

For the $^1A_1$ dissociation, a large KER is observed as a result of dissociation to the energetically stable CO + C_2H_4 product channel. The E_{hv}=3.20 eV is sufficient to overcome detachment energy for the C_{2v} singlet structure.[7, 9] A large KER is observed in systems

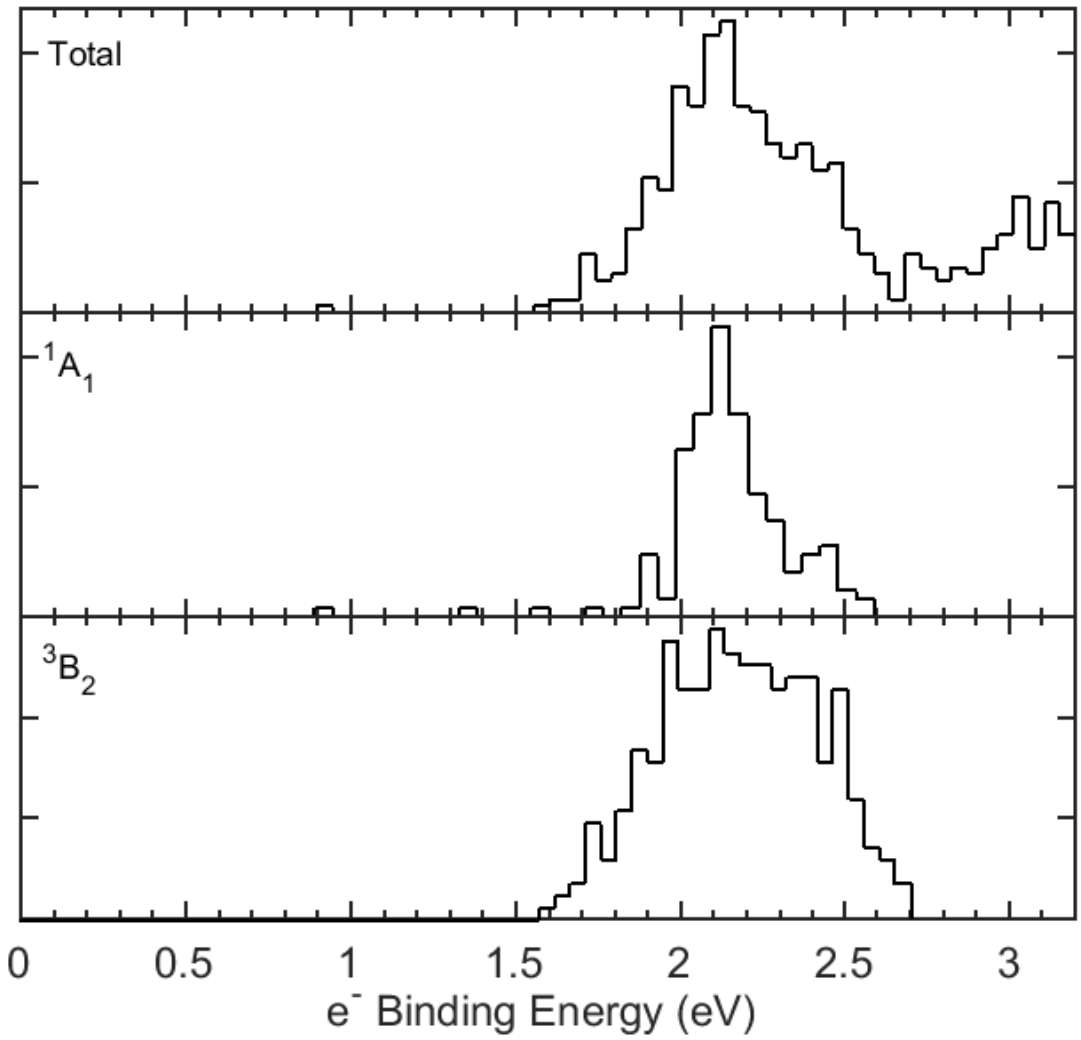

Figure 4.4. The total photoelectron spectrum measured in coincidence with dissociative products, as well as the individual photoelectron spectra for the two diradical states. The different photoelectron spectra were resolved through KER gating.

where the final product states are significantly more stable than the Franck-Condon region accessed through photodetachment. These steep dissociative curves are observed in the case of dissociation to CO + C_2H_4, which has been calculated to be 0.54 eV lower in energy than the ground state oxyallyl anion.[9] While some energy must be partitioned into overcoming the transition state barrier, a significant geometry change is also needed in order to reach the dissociative channel, which is observed leading to highly vibrationally excited products.

For the ground and excited triplet states, this symmetric dissociation channel is spin forbidden, indicating that intersystem crossing to the singlet surface would be required to reach the same CO + C_2H_4 product channel. The two triplet states have CCC bonds of approximately 121.3˚, a notably different geometry as compared to the $^1A_1$ CCC bond angle of 110.4˚. Due to the $^2A_2$ anion having a CCC bond angle of 113.7˚, significant vibrational excitation would be expected in the photoelectron spectrum for the $^3B_2$ and $^3B_1$ states.[7] Lineberger and co-workers observed a vibrational progression attributed to the ν_7 bending mode in the photoelectron spectrum for both the $^3B_1$ and $^3B_2$ states however a vibrational progression was not observed in the $^1A_1$ state.[6] Both triplet channels have a much smaller KER than the maximum available due to the internal excitation induced by intersystem crossing prior to dissociation.

Schalley *et al.* calculated the spin orbit coupling matrix element between the ground state singlet and the triplet surface to be small, indicating that intersystem crossing would not be favored.[9] This mechanism is still plausible due to the fact that the total dissociation observed for all three states only accounts for 10% of the overall signal. While the dissociative signal attributed to the $^1A_1$ and $^3B_2$ states is much lower in intensity as

compared to the stable signal, the $^3B_1$ channel is observed in equal intensity in dissociative and stable photoelectron spectra. The spin orbit coupling of the excited state to the singlet has not been reported, so it is possible that this is a more favored mechanism than the crossing from the $^3B_2$ state to the $^1A_1$ state. Sanov, Krylov and co-workers were able to model the $^1A_1$ curve using the symmetric rotation of the CH_2 groups and the CCC angle as internal coordinates from the Franck-Condon region to cyclopropanone.[7] However, no predictions about other portions of the surface, including dissociation of cyclopropanone were reported.[7] Intersystem crossing from the $^3B_2$ state to the $^1A_1$ state is predicted by theory to be a minor mechanism, which is consistent with these results.

The separation between the singlet and triplet states in the oxyallyl diradical have been a subject of debate in theoretical calculations due to the complicated structure of the $^1A_1$ surface. While the C_{2v} structure of the singlet forms cyclopropanone, a significant barrier to dissociation lies between cyclopropanone and the CO + C_2H_4 channel. This barrier has been calculated to be ~0.1 eV below the adiabatic detachment energy to the singlet state. While ring closure is the dominant mechanism on the singlet surface, it is evident from these results that dissociative photodetachment to CO + C_2H_4 is also a minor mechanism that occurs. The photoelectron spectra in Figure 4.4 for the individual states reveal that the experimental separation between the $^1A_1$ and $^3B_2$ states is ~0.06 eV, which is in excellent agreement with the calculated separation of ~0.06 eV.[7] The agreement in separation of the $^1A_1$ and $^3B_2$ states in this experiment further supports the assignment of these features in the photoelectron spectrum, allowing for the interpretation of the dissociation dynamics of the individual channels.

4.5. Conclusion

Dissociative photodetachment from the oxyallyl anion above threshold was observed for the first time from all three electronic states. The electron affinities match well with previous reported experimental values, and reveal the individual dissociation dynamics of each channel. The observation of dissociation from the $^3B_2$ and $^3B_1$ states indicates that intersystem crossing occurs from both states to the singlet surface, resulting in highly internally excited C_2H_4 + CO products. Direct photoexcitation on the $^1A_1$ surface leading to dissociation was also observed to result in C_2H_4 + CO products. These results confirm theoretical predictions for this system and provide further insights into the role triplet/singlet intersystem crossing can play in the dissociation dynamics of small organic radicals.

Chapter four is being prepared for publication, in which the dissertation author is the primary author and the dissertation advisor is the corresponding author. Lunny, K. G., Albeck, Y., Benitez, Y., Strasser, D., Continetti. R. E., "Dissociative Photodetachment of the Oxyallyl Anion in the Near Ultraviolet via Triplet-Singlet Intersystem Crossing"

4.6. References

1. Pedersen, S.; Herek, J. L.; Zewail, A. H., The Validity of the "Diradical" Hypothesis: Direct Femtosecond Studies of the Transition-State Structures. *Science* **1994,** *266*, 1359-1363.

2. Salem, L.; Rowland, C., The Electronic Properties of Diradicals. *Angew. Chem. Int. Ed.* **1972,** *11* (2), 92-111.

3. Borden, W. T., *Diradicals.* John Wiley and Sons Inc: New York, 1982.

4. Wenthold, P. G.; Hu, J.; Squires, R. R.; Lineberger, W. C., Photoelectron Spectroscopy of the Trimethylenemethane Negative Ion. *J. Am. Soc. Mass. Spectrom.* **1999,** *10*, 800-809.

5. Slipchenko, L. V.; Krylov, A. I., Electronic Structure of the Trimethylenemethane Diradical in its Ground and Electronically Excited States: Bonding, Equilibrium Geometries, and Vibrational Frequencies. *J. Chem. Phys.* **2003,** *118* (15), 6874-6883.

6. Ichino, T.; Villano, S.; Gianola, A.; Goebbert, D.; Velarde, L.; Sanov, A.; Blanksby, S.; Zhou, X.; Hrovat, D.; Borden, W. T.; Lineberger, W. C., Photoelectron Spectroscopic Study of the Oxyallyl Diradical. *J. Phys. Chem. A* **2011,** *115*, 1634.

7. Mozhayskiy, V.; Goebbert, D.; Velarde, L.; Sanov, A.; Krylov, A., Electronic Structure and Spectroscopy of Oxyallyl: A Theoretical Study. *J. Phys. Chem. A* **2010,** *114*.

8. Ichino, T.; Villano, S.; Gianola, A.; Goebbert, D.; Velarde, L.; Sanov, A.; Blanksby, S.; Zhou, X.; Hrovat, D.; Borden, W. T.; Lineberger, W. C., The Lowest Singlet and Triplet States of the Oxyallyl Diradical. *Angew. Chem. Int. Ed.* **2009,** *48*.

9. Schalley, C. A.; Blanksby, S.; Harvey, J. N.; Schroder, D.; Zummack, W.; Bowie, J. H.; Schwarz, H., A Combined Neutralization-Reionization Mass Spectrometric and Theoretical Study of Oxyallyl and Other Elusive Neutrals. *Eur. J. Org. Chem.* **1998,** *1998* (6), 987-1009.

10. Osamura, Y.; Borden, W. T.; Morokuma, K., Structure and Stability of Oxyallyl. An MCSCF Study. *J. Am. Chem. Soc.* **1983,** *106*, 5112-5115.

11. Hess, B. A.; Smentek, L., On the Relative Stabilities of Singlet and Triplet Oxyallyl and Cyclopropanone: A Density Functional Study. *Eur. J. Org. Chem.* **1999**, 3363-3367.

12. Coolidge, M. B.; Yamashita, K.; Morokima, K.; Borden, W. T., Ab Initio MCSCF and CI Calculations of the Singlet-Triplet Energy Differences in Oxyallyl and in Dimethyloxyallyl. *J. Am. Chem. Soc.* **1990,** *112* (5), 1751-1754.

13. Karami, F.; Vahedpour, M., Computational Mechanistic Investigation of the Gas Phase C_2H_4 + CO Reaction on the Singlet and Triplet Potential Energy Surfaces. *J. Iran. Chem. Soc.* **2014,** *11*, 781-790.

14. Rodriguez, H. J.; Chang, J. C.; Thomas, T. F., Thermal, Photochemical and Photophysical Processes in Cyclopropanone Vapor. *J. Am. Chem. Soc.* **1976,** *98* (8), 2027-2034.

15. Lunny, K. G.; Benitez, Y.; Albeck, Y.; Strasser, D.; Stanton, J. F.; Continetti, R. E., Spectroscopy of Ethylenedione and Ethynediolide: A Reinvestigation. *Angew. Chem. Int. Ed.* **2018,** *57* (18), 5394-5397.

16. Dixon, A.; Xue, T.; Sanov, A., Spectroscopy of Ethylenedione. *Angew. Chem. Int. Ed.* **2015,** *54* (127), 8764-8767.

17. Albeck, Y.; Lunny, K. G.; Benitez, Y.; Shin, A. J.; Strasser, D.; Continetti, R. E., Resonance-Mediated Below-Threshold Delayed Photoemission and Non-Franck-Condon Photodissociation of Cold Oxyallyl Anions. *Angew. Chem. Int. Ed.* **2019,** *58* (16), 5312-5315.

18. Shen, B.; Benitez, Y.; Lunny, K. G.; Continetti, R. E., Internal Energy Dependence of the Photodissociation Dynamics of O_3^- Using Cryogenic Photoelectron-Photofragment Coincidence Spectroscopy. *J. Chem. Phys.* **2017,** *147*, 094307.

19. Wiley, W. C.; McLaren, I. H., Time of Flight Mass Spectrometer with Improved Resolution. *Rev. Sci. Instrum.* **1955,** *26*, 1150-1157.

20. Johnson, C. J.; Shen, B. B.; Poad, B. L. J.; Continetti, R. E., Photoelectron-Photofragment Coincidence Spectroscopy in a Cryogenically Cooled Linear Electrostatic Ion Beam Trap. *Rev. Sci. Instrum.* **2011,** *82*, 105105.

21. Zajfman, D.; Rudich, Y.; Sagi, I.; Strasser, D.; Savin, D. W.; Goldberg, S.; Rappaport, M.; Heber, O., High Resolution Mass Spectrometry Using a Linear Electrostatic Ion Beam Trap. *Int. J. Mass. Spectrom.* **2003,** *229*, 55-60.

22. Dixon, A.; Xue, T.; Sanov, A., HOCCO versus OCCO: Comparative Spectroscopy of the Radical and Diradical Reactive Intermediates. *J. Chem. Phys.* **2016,** *144*.

Chapter 5: Resonance-Mediated Below-Threshold Delayed Photoemission and Non-Franck-Condon Photodissociation of Cold Oxyallyl Anions

5.1. Introduction

Photoionization and photodetachment are generally considered prompt events in which an electron is instantaneously removed from a neutral or anionic system, respectively. The resulting instantaneous change in the electronic potential surface can trigger nuclear motion dynamics, structural rearrangement and even dissociation on femtosecond – picosecond timescales. In contrast, near threshold photodetachment of hot cluster anion systems can exhibit delayed emission, occurring up to hundreds of microseconds after the laser pulse.[1-3] Such delayed emission has been successfully explained in terms of thermionic emission from a microcanonical ensemble, resulting in a characteristic power-law decay even in relatively small systems such as the C_4^- cluster.[3] In larger molecular anions, such as polycyclic aromatic hydrocarbons, long-lived resonances and delayed ionization have also been observed.[4] In this work, delayed emission in a small, cold molecular anion is examined using photoelectron-photofragment coincidence (PPC) spectroscopy after photoexcitation ~0.3 eV below the adiabatic detachment energy. The oxyallyl anions ($C_3H_4O^-$) are observed to undergo competing delayed autodetachment and photodetachment by a second photon in processes mediated by nuclear dynamics in an intermediate excited state.

Delayed emission is a fundamental physical process that can play a role in electron-molecule and anion-neutral reactions in systems as complex as radiation damage in biology and astrochemical processes.[5-7] One class of neutral intermediates that exhibit complex

electronic structure, even in relatively small molecular systems, are diradicals.[8, 9] Perfect diradicals such as trimethylenemethane, $CH_2C(CH_2)CH_2$, have two degenerate molecular orbitals.[10, 11] Substitution of an oxygen atom for one of the CH_2 groups in trymethylenemethane results in the oxyallyl diradical, C_3H_4O, where the degeneracy is lifted by stabilization of the singlet state via interactions with the lone pairs on the oxygen atom.[9] The energetics and structure of the oxyallyl diradical have been previously examined in a number of theoretical studies.[12-16] The first experimental examination of oxyallyl was reported by Lineberger and co-workers, who observed the singlet and low-lying triplet states of the diradical by photodetachment of the oxyallyl anion. The adiabatic detachment energy (ADE) of 1.94 eV was measured at a photon energy of E_{hv} = 3.53 eV.[17, 18] In a recent publication, oxyallyl was further characterized using PPC spectroscopy at a photon energy of E_{hv} = 3.20 eV.[19] The results were consistent with the photoelectron spectra reported by Lineberger and co-workers and measured in coincidence with the predominant production of a stable neutral, confirming theoretical predictions about the stability of the $^3B_2$ ground state.

Both the neutral and anion surfaces of the C_3H_4O system show several local minima, including stable C_{2v} structures as well as triangular closed-ring cyclopropanone (CP) structures.[12] Figure 5.1 shows a selected part of the energetic landscape of the neutral and anionic systems based on the experimental values from Lineberger and co-workers as well as the theoretical predictions from the literature.[12, 13, 18] The C_3H_4O anion surface includes multiple isomers, including the $^2A_2$ oxyallyl anion ground state, the excited cyclopropanone anion and the low-lying $^2B_1$ oxyallyl anion excited state. The anion ground state is calculated to have a planar C_{2v} symmetric geometry while the

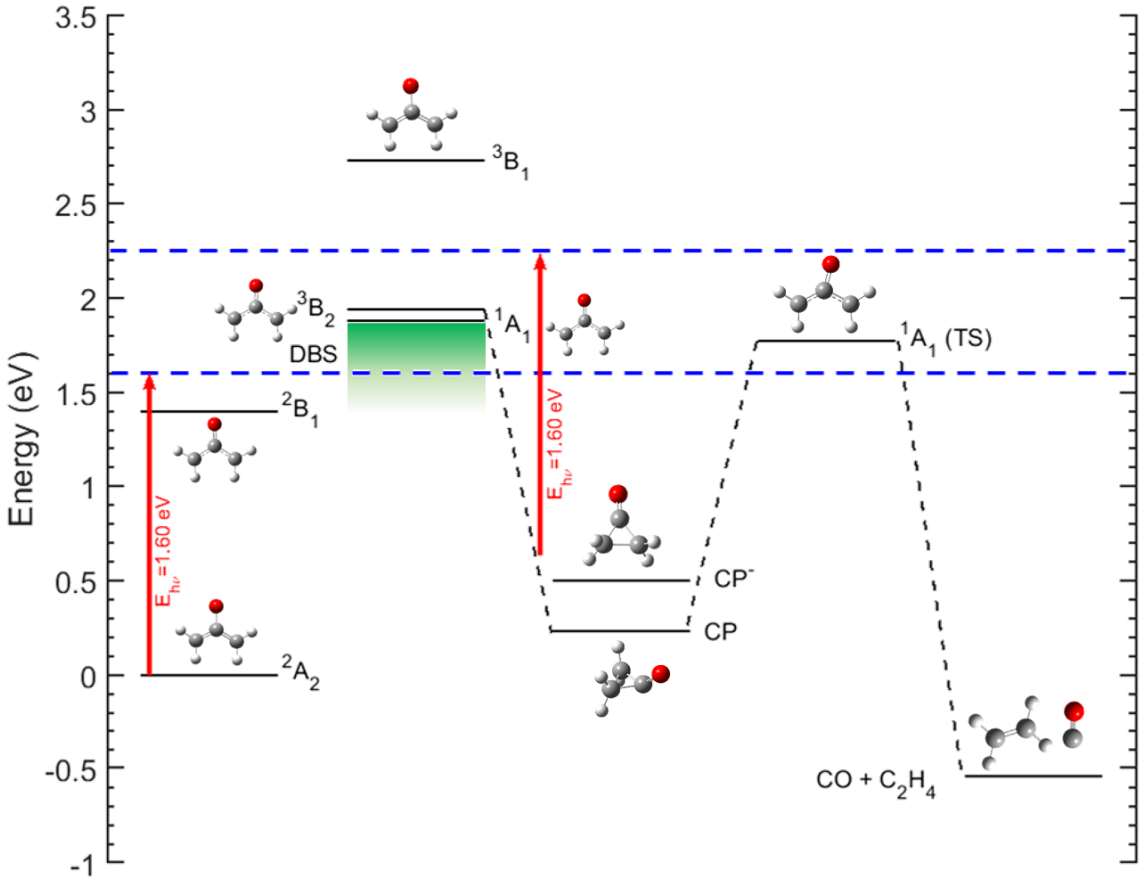

Figure 5.1. Energetics diagram of the relevant portions of the oxyallyl anion and neutral potential energy surfaces.[12, 13] The proposed energy range of the dipole bound state (DBS) built on the $^1A_1$ singlet core is represented in green.

cyclopropanone anion has the oxygen out-of-plane resulting in C_s symmetry. For the neutral surface, singlet and triplet states are shown. While the singlet has no barrier between the Franck-Condon geometry and ring closure to form the neutral cyclopropanone, the ground and excited triplet states are stable and are estimated to decay on a microsecond time scale due to a small spin-orbit coupling.[18] Dissociation towards the energetically favorable CO + C_2H_4 fragments exhibits a barrier with a calculated transition state lying ~1.76 eV above the anion ground state, ~0.17 eV below the 1.94 eV adiabatic detachment energy.[12]

In this study, photodetachment from cold oxyallyl anions is explored at a photon energy ~0.3 eV below the adiabatic detachment energy (E_{hv}=1.60 eV), using photoelectron-photofragment coincidence spectroscopy. The cold precursor anions are prepared using a cryogenic octopole accumulation trap, ensuring that the anions are in their ground electronic and vibrational states.[20] PPC spectroscopy is able to directly distinguish both prompt and delayed photodetachment, as well as dissociative events and stable neutral products by measuring the electron photoemission from anions in coincidence with the resulting neutral products. The measured photoelectron spectra, fragment recoil, and the correlation of photoelectron kinetic energy and photofragment kinetic energy release are presented and discussed in terms of the nature of the long-lived autodetachment resonance.

5.2. Experimental Methods

The experimental setup was previously described in detail.[20, 21] As discussed in our recent study of oxyallyl anion formation and assignment in experiments at a photon energy of 3.20 eV, different precursors including glyoxal or isopropanol vapor seeded in N_2O can

be used to form oxyallyl anions.[13, 22] The ions are produced in a supersonic expansion source with a pulsed discharge at 10 Hz and crossed with a 1 keV electron beam. The ions are then extracted using a Wiley-McLaren time-of-flight mass spectrometer and cooled in a cryogenic octopole accumulation trap (COAT). Thus, any vibrational or electronic excitation in the ionization process is quenched by collisions with a 17 K He/H_2 buffer gas mixture for 40 ms. The cold ions are then accelerated to 7 keV and mass selected before injection into a cryogenic electrostatic ion beam trap (EIBT) that allows a fast ion beam to oscilate between two electrostatic mirrors. In the field free region of the EIBT, the ion beam is intersected by a 1.2 ps 775 nm (1.60 eV) laser pulse operating at 1037 Hz (Ti:Sapphire regenerative amplifier Clark-MXR CPA 2000). A 0.5 m focal length lens was used for high power measurements, compared to low power measurements with a 2.5:1 telescope, to confirm two-photon events. Photoelectrons are extracted orthogonal to the ion beam, allowing 3D imaging of the electron energy on a time and position sensitive detector.

The timing resolution of the photoelectron detector is ~200 ps, somewhat smaller than the 300 ps bin width in the electron flight time distribution in Figure 5.2. Neutral products are detected 1.31 m downstream, when products recoil through the EIBT trapping potentials on a multi-particle time and position sensitive detector. As the parent anion energy is determined by the EIBT trapping conditions, the time-of-flight (TOF) to the detector provides additional verification of the parent anion mass. Furthermore, in the case of dissociation, momentum conservation allows mass assignment and rejection of random coincidence events. Coincidence detection of both photoelectrons and neutral fragments allows obtaining the total kinetic energy released in each dissociative photodetachment event. The electron detector was calibrated using O_2^- giving a resolution of $\Delta eKE/eKE$

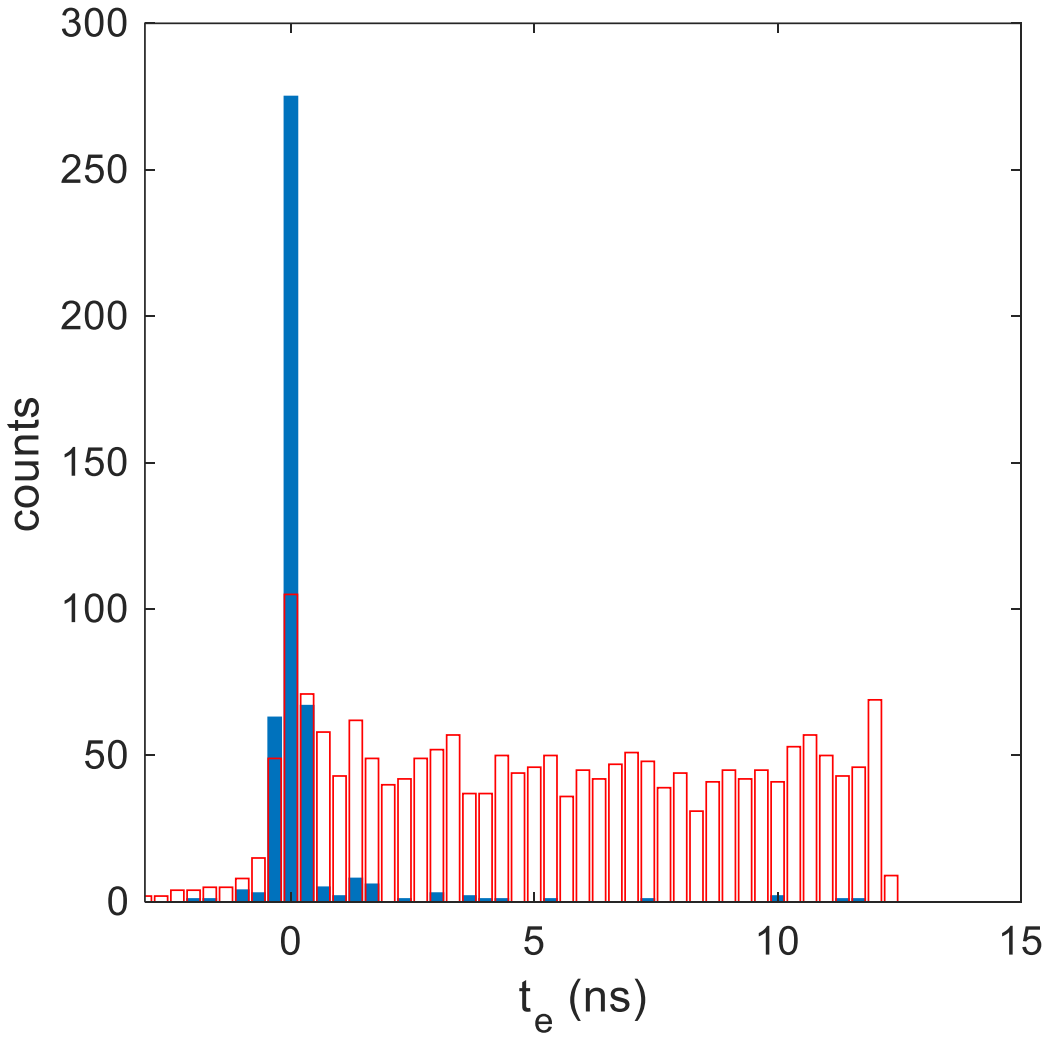

Figure 5.2. Time-of-arrival spectrum for electrons incident on the photoelectron detector in coincidence with a single neutral product (empty red bars) or in coincidence with two correlated neutral fragments (full blue bars).

~4% and the neutral detector was calibrated using O_4^- giving a resolution of ΔKER/KER ~10%.

5.3. Discussion

Figure 5.2 shows the electron time-of-flight (t_e) from the laser-ion interaction region to the photoelectron detector, relative to the arrival time of prompt zero kinetic energy electrons. Photoelectrons arriving in coincidence with a dissociation event are found to arrive at the expected t_e = 0, with a width of ~200 ps corresponding to photoelectrons ejected along the TOF axis with an electron kinetic energy (eKE) spread of ~300 meV, as shown by the full blue bars. In contrast, photoelectrons arriving in coincidence with a single neutral product exhibit extended t_e up to ~12 ns, consistent with delayed emission with respect to the 1.2 ps laser pulse. The sharp drop at ~12 ns reflects the exit of the fast photoexcited anions from the photoelectron spectrometer. This is the first observation of delayed emission for a small, cold molecular system.

Due to the photoelectron spectrometer extraction field, delayed emission can affect the final trajectory of the neutral product. Indeed, the neutral fragments are detected above the position of prompt detachment products that is reproduced by the center of mass position of prompt dissociative events on the detector plane, which can be seen in Figure 5.3. On the horizontal axis of the neutral detector, the narrow spread of delayed hit positions is comparable to the spread observed for prompt detachment center of mass positions. Thus, reflecting the intrinsic velocity spread of the trapped anion beam and supporting a single neutral product in the case of the delayed detachment channel.

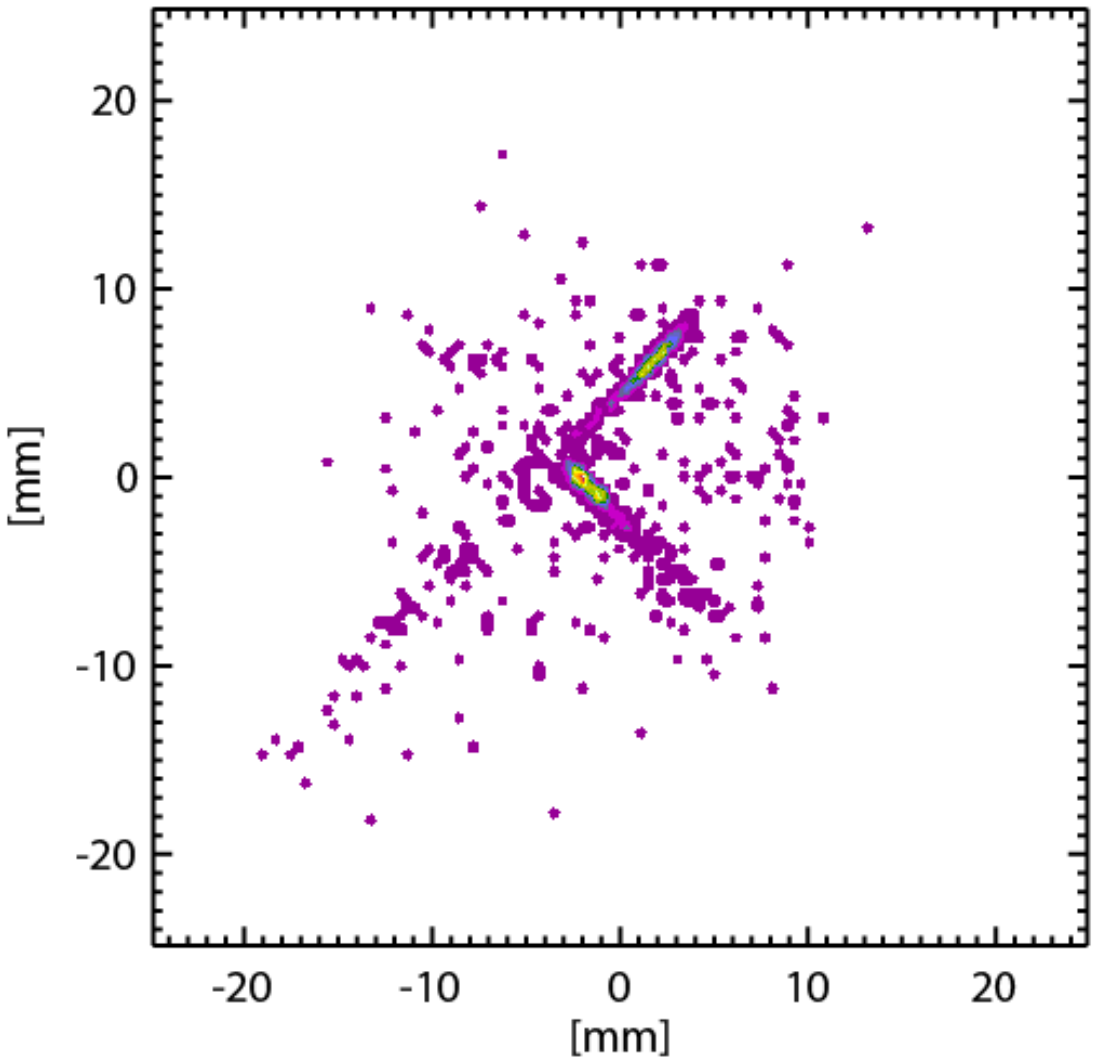

Figure 5.3. QXDL image of the relative positions of the prompt and delayed emission products.

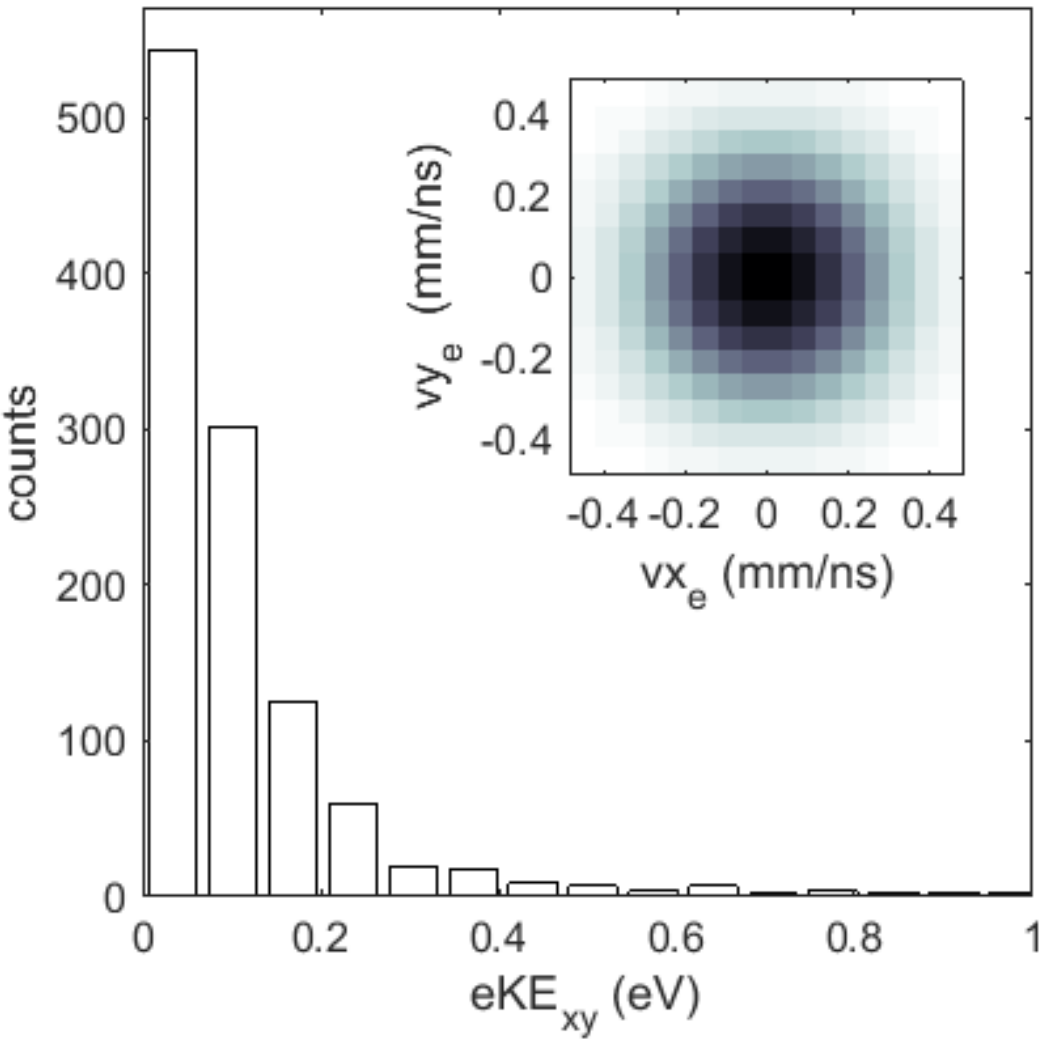

Figure 5.4. Photoelectron spectrum of delayed detachment events. Inset: isotropic angular distribution of photoelectron velocities in the detector plane with respect to the linear laser polarization in the y direction.

Although the uncertainty in the delayed emission time prevents 3D imaging of the photoelectron velocity, the photoelectron velocity in the 2D plane of the detector can be measured.[23] Figure 5.4 shows the photoelectron spectrum, extracted from the 2D photoelectron velocity distribution in the detector plane, shown in the figure inset. The photoelectron spectrum is peaked at zero electron kinetic energy, eKE, with ~95% percentile observed at eKE < 250 meV, as can be expected for delayed emission. The isotropic angular distribution seen in the inset for Figure 5.4 (with respect to the laser polarization along the vertical axis) is in agreement with the expected loss of alignment due to molecular rotation on the picosecond time scale before the delayed emission event takes place. When examining the different possible states that are accessible and may lead to autodetachment for the stable species, the most likely candidate is a dipole bound state (DBS) built on the zwitterionic singlet oxyallyl diradical core, as discussed further below. While there is the low-lying $^2B_1$ anion excited state, optical excitation of this valence state would likely induce fluorescence or coupling to the dipole bound state.

Involvement of a dipole bound state with the singlet diradical core is likely for a number of reasons. From previous studies of the photodetachment of the oxyallyl anion in the ultraviolet, it is known that both the triplet and singlet states of the oxyallyl diradical have good Franck-Condon overlap with the ground state anion.[13, 18] It is also known that the singlet state is a transition state with an estimated 170 fs lifetime and can undergo a barrier-free isomerization toward the stable cyclopropanone neutral state.[13] As the C-C-C bond angle decreases, the neutral states drop below the anion resonance prepared at 1.60 eV, leading to delayed autodetachment from an incipient metastable cyclopropanone anion, resulting in the production of stable cyclopropanone. While the neutral product of delayed

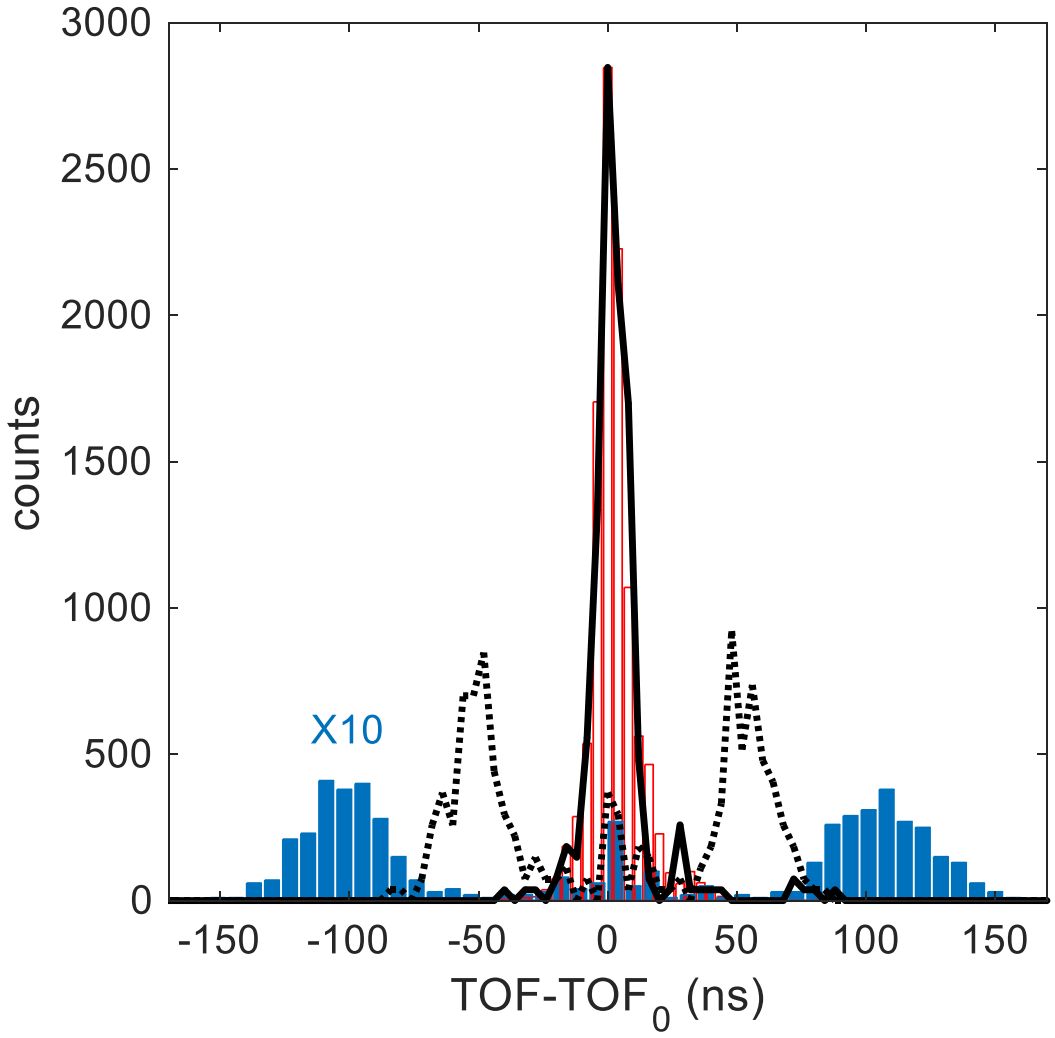

Figure 5.5. TOF of single neutral hits (empty red bars) along with TOF of two coincident neutral hits (full blue bars). Center of mass TOF of these dissociation events are presented– assuming a symmetric breakup (solid line) and an alternative asymmetric C_2H_2O + CH_2 dissociation channel (dotted line).

emission is expected to be highly vibrationally excited, the level of excitation with a single 1.60 eV photon is insufficient to overcome the ~1.5 eV calculated barrier between the neutral cyclopropanone and dissociation on the calculated neutral potential energy surface, resulting in a single neutral product in coincidence with the delayed low energy electron.

Unlike the delayed emission observed in coincidence with a single neutral product, prompt photoelectrons are observed in coincidence with two neutral fragments. Momentum conservation in the center of mass frame of the parent anion identifies the prompt channel products as $CO + C_2H_4 + e^-$. Figure 5.5 presents the measured time-of-flight distributions corresponding to a single neutral (empty red) or two neutral fragments (full blue) detected in coincidence with a photoelectron. Considering an estimated ~30% detection efficiency, we estimate a $\geq$ 15% branching ratio for the dissociative channel. Coincidence detection allows calculating the TOF of the center of mass of each dissociation event by assuming dissociation into one of the possible product channels. The full curve shows the center of mass time-of-flight distribution assuming a $CO + C_2H_4$ breakup, scaled to the single neutral time-of-flight distribution to emphasize the perfect agreement with the 8 ns spread. In contrast, other breakup channels such as $CCH_2O + CH_2$, however likely given the initial geometry, can be excluded based on momentum conservation, as shown by the dotted line. Since the oxyallyl diradical has no symmetric bond, the equal mass breakup implies to rearrangement of the system to cyclopropanone prior to dissociation into $CO + C_2H_4$.

Figure 5.1 illustrates that the 1.60 eV photon energy used in this experiment is lower than the 1.94 eV adiabatic detachment energy. Nevertheless, the observed prompt

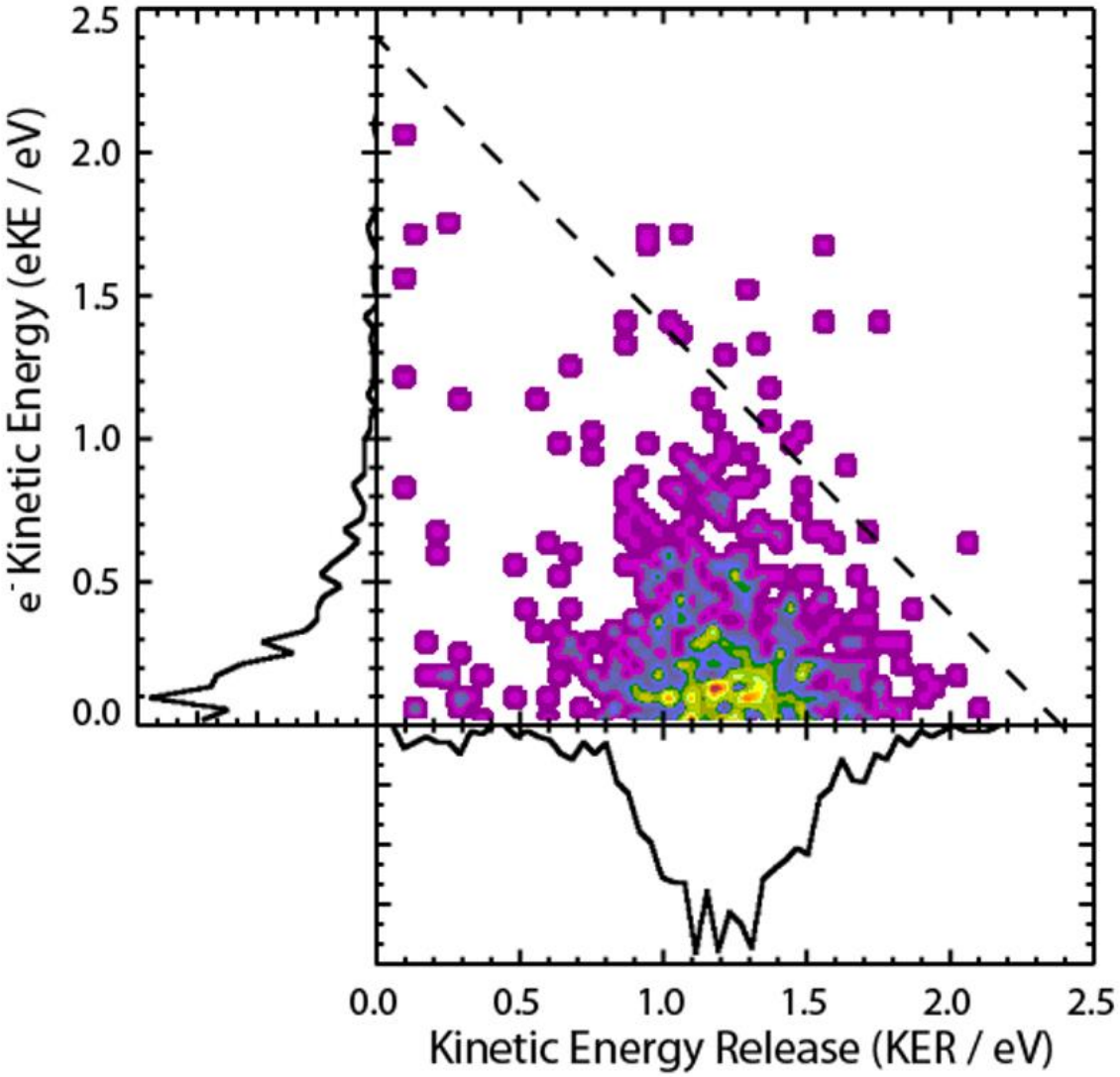

Figure 5.6. Photoelectron-photofragment coincidence spectrum of the kinetic energy partitioning in the two-photon dissociative photodetachment channel. The dashed line indicates the kinetic energy maximum (KE_{max}) at ~2.4 eV.

photoelectrons exhibit significant eKE of up to 1 eV, though peaked at low photoelectron energies. Figure 5.6 shows the measured coincidence spectrum of the prompt dissociative channel, illustrating how translational energy is partitioned between the electron and neutral photofragments. The large and broad kinetic energy release, peaked at ~1.4 eV and extending up to ~2.4 eV is consistent with concerted elimination over a significant barrier. The prompt dissociative photodetachment channel is therefore attributed to the absorption of one photon to form the intermediate dipole bound state and then a second photon of E_{hv}=1.60 eV within the 1.2 ps laser pulse, before delayed autodetachment occurs.[18]

The dipole bound state formed with the $^1A_1$ neutral state core is the most plausible explanation for this phenomenon. The $^1A_1$ neutral state has been calculated to have a dipole moment of 4.2 Debye resulting from the strong zwitterionic character for this type of diradical. [10] The geometries for these states have been calculated and reported by the Krylov group, at the CCSD-UHF/6-311(+,+)G(2df, 2pd) level of theory. Using these optimized geometries, the dipole moment for each of the anion and neutral states were calculated at the CCSD/6-311G level of theory. As seen in Table 5.1, the $^1A_1$ open ring neutral state had a significantly larger dipole moment than the other geometries. A dipole bound state requires dipole moments larger than ~2.5 Debye to bind a diffuse excess electron.[24-26] While these states often have electron binding energies of <100 cm^{-1}, up to 0.40 eV binding energies have been observed in structures such as glycine with large dipole moments.[25, 27, 28] These diffuse anion states have similar geometries and thus excellent Franck-Condon overlap with the corresponding neutral states. The $^1A_1$ open ring neutral structure is also known to have good Franck-Condon overlap with the anion,

Table 5.1. Optimized geometries at the CCSD/6-311(+,+)G(2df, 2pd) level of theory by Krylov and co-workers.[13] Dipole moments were calculated from optimized geometries at the CCSD/6-311G level of theory.

Geometry	CO length	CC length	CCC angle	Dipole Moment (Debye)
$^2A_2$	1.27210	1.42504	113.72	2.9599
$^2B_1$	1.34483	1.38320	124.631	3.4996
$^3B_2$	1.25450	1.43425	121.310	2.7579
$^3B_1$	1.33444	1.38326	123.693	2.7110
$^1A_1$ (TS)	1.20544	1.46082	110.440	4.1784

inducing vibrational excitation in C-C-C bending mode and the symmetric stretching mode.[13]

This internal excitation in the dipole bound state is expected to promote motion along the C-C-C reaction coordinate for ring closure. Absorption of a second photon in the 1.2 ps pulse, as the system is undergoing ring closure but prior to autodetachment would provide sufficient excitation on an excited singlet state to surmount the barrier towards dissociation, 1.54 eV above the cyclopropanone ground state. Thus, in addition to promoting delayed detachment in this small molecular anion, the strongly bound dipole bound state built on the singlet core of the oxyallyl diradical also mediates a two-photon dissociation process leading to the concerted elimination of closed shell molecular products CO + C_2H_4, a non-Franck-Condon allowed process.

5.4. Conclusion

In summary, photoexcitation of cold $C_3H_4O^-$ anions with E_{hv}=1.60 eV, 0.3 eV below the vertical detachment energy, was found to produce a long-lived resonance resulting in two distinct product channels. In one case, delayed emission is observed with a lifetime greater than 10 ns, producing a stable neutral product. In the second case, prompt dissociative photodetachment is observed when the long-lived resonance absorbs a second photon within the same 1.2 ps laser pulse. The second photon probes the structural rearrangement mediated by the barrier-free relaxation of the $^1A_1$ diradical core of the intermediate dipole bound state along the reaction path for ring closure to form cyclopropanone, promoting the CO + C_2H_4 + e^- dissociative photodetachment product channel. In contrast to the ubiquitous observation of delayed emission from hot anionic

species successfully described by statistical models, the present study is initiated from a cold parent anion with internal excitation governed by Franck-Condon overlap followed by significant structural rearrangement.[1-3] Other trimethylenemethane derivatives could provide further examples of diradicals that exhibit dipole bound anion states that can be used to manipulate the reactivity on the neutral surface. Quantum chemistry studies and ultrafast time-resolved pump-probe experiments will be valuable for further understanding the chemical dynamics of photoexcited long-lived anion resonances in small molecular anions.

This chapter is adapted from the following publication, in which the dissertation author is one of the primary authors and the dissertation advisor is one of the corresponding authors. Albeck, Y., Lunny, K. G., Benitez, Y., Shin, A. J., Strasser, D., Continetti. R. E., "Resonance-Mediated Below-Threshold Delayed Photoemission and Non-Franck-Condon Photodissociation of Cold Oxyallyl Anions", *Angewandte Chemie International Edition,* 2019, 58, 5312.

5.5. References

1. Anderson, J. U.; Bonderup, E.; Hansen, K., Thermionic Emission from Clusters. *J. Phys. B: Mol. Opt. Phys.* **2002,** *35*, 1-30.

2. Bragg, A. E.; Verlet, J. R. R.; Kammrath, A.; Cheshnovsky, O.; Neumark, D. M., Electronic Relaxation Dynamics of Water Cluster Anions. *J. Am. Chem. Soc.* **2005,** *127* (43), 15283-15295.

3. Aviv, O.; Toker, Y.; Rajput, J.; Strasser, D.; Heber, O.; Schwalm, D.; Zajfman, D.; Anderson, L. H., Search for Dimer Emission from Photoexcited Al_4^-. *Phys. Rev. A* **2010,** *82*, 035201.

4. Stanley, L. H.; Anstoter, C. S.; Verlet, J. R. R., Resonances of the Anthracenyl Anion Probed by Frequency-Resolved Photoelectron Imaging of Collision-Induced Dissociated Anthracene Carboxylic Acid. *Chem. Sci.* **2017,** *8*, 3054-3061.

5. Bjorn, L. O.; Forsberg, A. S., Imaging by Delayed Emission (Phytoluminography) as a Method for Detecting Damage to Photosynthetic System. *Physiol. Plant.* **1979,** *47*, 215-222.

6. Frontera, F.; Amati, L.; Costa, E.; Muller, J. M.; Pian, E.; Piro, L.; Soffitta, P.; Tavani, M.; Castro-Trado, A.; Dal Fiume, D.; Feroci, M.; Heise, J.; Masetti, N.; Nicastro, L.; Orlandini, M.; Palazzi, E.; Sari, R., Prompt and Delayed Emission Properties of Gamma-Ray Bursts Observed with *BeppoSAX The Astrophysical Journal Supplement Series* **2000,** *127*, 59-78.

7. Abdo, A. A.; Ackermann, M.; Ajello, M.; Asano, K.; Atwood, W. B.; Axelsson, M.; Baldini, L.; Ballet, J.; Barbiellini, G.; Baring, M. G.; Bastieri, D.; Bechtol, K.; Bellazzini, R.; Berenji, B.; Bhat, P. N.; Bissaldi, E.; Blandford, R. D.; Bloom, E. D.; Bonamente, E.; Borgland, A. W.; Bouvier, A.; Bregeon, J.; Brez, A.; Briggs, M. S.; Brigida, M.; Bruel, P.; Burgess, J. M.; Burrows, D. N.; Buson, S.; Caliandro, G. A.; Cameron, R. A.; Caraveo, P. A.; Casandjian, J. M.; Cecchi, C.; Çelik, Ö.; Chekhtman, A.; Cheung, C. C.; Chiang, J.; Ciprini, S.; Claus, R.; Cohen-Tanugi, J.; Cominsky, L. R.; Connaughton, V.; Conrad, J.; Cutini, S.; d'Elia, V.; Dermer, C. D.; de Angelis, A.; de Palma, F.; Digel, S. W.; Dingus, B. L.; Silva, E. do Couto e.; Drell, P. S.; Dubois, R.; Dumora, D.; Farnier, C.; Favuzzi, C.; Fegan, S. J.; Finke, J.; Fishman, G.; Focke, W. B.; Fortin, P.; Frailis, M.; Fukazawa, Y.; Funk, S.; Fusco, P.; Gargano, F.; Gehrels, N.; Germani, S.; Giavitto, G.; Giebels, B.; Giglietto, N.; Giordano, F.; Glanzman, T.; Godfrey, G.; Goldstein, A.; Granot, J.; Greiner, J.; Grenier, I. A.; Grove, J. E.; Guillemot, L.; Guiriec, S.; Hanabata, Y.; Harding, A. K.; Hayashida, M.; Hays, E.; Horan, D.; Hughes, R. E.; Jackson, M. S.; Jóhannesson, G.; Johnson, A. S.; Johnson, R. P.; Johnson, W. N.; Kamae, T.; Katagiri, H.; Kataoka, J.; Kawai, N.; Kerr, M.; Kippen, R. M.; Knödlseder, J.; Kocevski, D.; Komin, N.; Kouveliotou, C.; Kuss, M.; Lande, J.; Latronico, L.; Lemoine-Goumard, M.; Longo, F.; Loparco, F.; Lott, B.; Lovellette, M. N.; Lubrano, P.; Madejski, G. M.; Makeev, A.; Mazziotta, M. N.; McBreen, S.; McEnery, J. E.; McGlynn, S.; Meegan, C.; Mészáros, P.; Meurer, C.; Michelson, P. F.; Mitthumsiri, W.; Mizuno, T.; Moiseev, A. A.; Monte, C.; Monzani, M. E.; Moretti, E.; Morselli, A.; Moskalenko, I. V.; Murgia, S.; Nakamori, T.; Nolan, P. L.; Norris, J. P.; Nuss, E.; Ohno, M.; Ohsugi, T.; Omodei, N.; Orlando, E.; Ormes, J. F.; Paciesas, W. S.; Paneque, D.; Panetta, J. H.; Pelassa, V.; Pepe, M.; Pesce-Rollins, M.; Petrosian, V.; Piron, F.; Porter, T. A.; Preece, R.; Rainò, S.; Rando, R.; Rau, A.; Razzano, M.; Razzaque, S.; Reimer, A.; Reimer, O.; Reposeur, T.; Ritz, S.; Rochester, L. S.; Rodriguez, A. Y.; Roming, P. W. A.; Roth, M.; Ryde, F.; Sadrozinski, H. F.-W.; Sanchez, D.; Sander, A.; Saz Parkinson, P. M.; Scargle, J. D.; Schalk, T. L.; Sgrò, C.; Siskind, E. J.; Smith, P. D.; Spinelli, P.; Stamatikos, M.; Stecker, F. W.; Stratta, G.; Strickman, M. S.; Suson, D. J.; Swenson, C. A.; Tajima, H.; Takahashi, H.; Tanaka, T.; Thayer, J. B.; Thayer, J. G.; Thompson, D. J.; Tibaldo, L.; Torres, D. F.; Tosti, G.; Tramacere, A.; Uchiyama, Y.; Uehara, T.; Usher, T. L.; van der Horst, A. J.; Vasileiou, V.; Vilchez, N.; Vitale, V.; von Kienlin, A.; Waite, A. P.; Wang, P.; Wilson-Hodge, C.; Winer, B. L.; Wood, K. S.; Yamazaki, R.; Ylinen, T.; Ziegler, M. FERMI Observations of GRB 090902B: A

Distinct Spectral Component in the Prompt and Delayed Emission. *The Astrophysical Journal* **2009,** *706*, L138-L144.

8. Borden, W. T., *Diradicals*. John Wiley and Sons Inc: New York, 1982.

9. Salem, L.; Rowland, C., The Electronic Properties of Diradicals. *Angew. Chem. Int. Ed.* **1972,** *11* (2), 92-111.

10. Wenthold, P. G.; Hu, J.; Squires, R. R.; Lineberger, W. C., Photoelectron Spectroscopy of the Trimethylenemethane Negative Ion. *J. Am. Soc. Mass. Spectrom.* **1999,** *10*, 800-809.

11. Slipchenko, L. V.; Krylov, A. I., Electronic Structure of the Trimethylenemethane Diradical in its Ground and Electronically Excited States: Bonding, Equilibrium Geometries, and Vibrational Frequencies. *J. Chem. Phys.* **2003,** *118* (15), 6874-6883.

12. Schalley, C. A.; Blanksby, S.; Harvey, J. N.; Schroder, D.; Zummack, W.; Bowie, J. H.; Schwarz, H., A Combined Neutralization-Reionization Mass Spectrometric and Theoretical Study of Oxyallyl and Other Elusive Neutrals. *Eur. J. Org. Chem.* **1998,** *1998* (6), 987-1009.

13. Mozhayskiy, V.; Goebbert, D.; Velarde, L.; Sanov, A.; Krylov, A., Electronic Structure and Spectroscopy of Oxyallyl: A Theoretical Study. *J. Phys. Chem. A* **2010,** *114*.

14. Osamura, Y.; Borden, W. T.; Morokuma, K., Structure and Stability of Oxyallyl. An MCSCF Study. *J. Am. Chem. Soc.* **1983,** *106*, 5112-5115.

15. Hess, B. A.; Smentek, L., On the Relative Stabilities of Singlet and Triplet Oxyallyl and Cyclopropanone: A Density Functional Study. *Eur. J. Org. Chem.* **1999**, 3363-3367.

16. Coolidge, M. B.; Yamashita, K.; Morokima, K.; Borden, W. T., Ab Initio MCSCF and CI Calculations of the Singlet-Triplet Energy Differences in Oxyallyl and in Dimethyloxyallyl. *J. Am. Chem. Soc.* **1990,** *112* (5), 1751-1754.

17. Ichino, T.; Villano, S.; Gianola, A.; Goebbert, D.; Velarde, L.; Sanov, A.; Blanksby, S.; Zhou, X.; Hrovat, D.; Borden, W. T.; Lineberger, W. C., The Lowest Singlet and Triplet States of the Oxyallyl Diradical. *Angew. Chem. Int. Ed.* **2009,** *48*.

18. Ichino, T.; Villano, S.; Gianola, A.; Goebbert, D.; Velarde, L.; Sanov, A.; Blanksby, S.; Zhou, X.; Hrovat, D.; Borden, W. T.; Lineberger, W. C., Photoelectron Spectroscopic Study of the Oxyallyl Diradical. *J. Phys. Chem. A* **2011,** *115*, 1634.

19. Lunny, K. G.; Benitez, Y.; Albeck, Y.; Strasser, D.; Stanton, J. F.; Continetti, R. E., Spectroscopy of Ethylenedione and Ethynediolide: A Reinvestigation. *Angew. Chem. Int. Ed.* **2018,** *57* (18), 5394-5397.

20. Shen, B.; Benitez, Y.; Lunny, K. G.; Continetti, R. E., Internal Energy Dependence of the Photodissociation Dynamics of O_3^- Using Cryogenic Photoelectron-Photofragment Coincidence Spectroscopy. *J. Chem. Phys.* **2017,** *147*, 094307.

21. Johnson, C. J.; Shen, B. B.; Poad, B. L. J.; Continetti, R. E., Photoelectron-Photofragment Coincidence Spectroscopy in a Cryogenically Cooled Linear Electrostatic Ion Beam Trap. *Rev. Sci. Instrum.* **2011,** *82*, 105105.

22. Dixon, A.; Xue, T.; Sanov, A., Spectroscopy of Ethylenedione. *Angew. Chem. Int. Ed.* **2015,** *54* (127), 8764-8767.

23. Eppink, A. T. J. B.; Parker, David H., Velocity Map Imaging of Ions and Electrons using Electrostatic Lenses: Application in Photoelectron and Photofragment Ion Imaging of Molecular Oxygen *Rev. Sci. Instrum.* **1997,** *68* (9), 3477-3484.

24. Brinkman, E., A.; Berger, S.; Marks, J.; Brauman, J. I., Molecular Rotation and the Observation of Dipole-Bound States of Anions. *J. Chem. Phys.* **1993,** *99* (10), 7586-7594.

25. Dessent, C. E. H.; Bailey, C. G.; Johnson, M. A., Observation of the Dipole-Bound Excited State of the I^- Acetone Ion-Molecule Complex. *J. Chem. Phys.* **1995,** *102* (15), 6335.

26. Yandell, M. A.; King, S. B.; Neumark, D. M., Decay Dynamic of Nascent Acetonitrile and Nitromethane Dipole-Bound Anions Produced by Intracluster Charge-Transfer. *J. Chem. Phys.* **2014,** *140*, 184317.

27. Gutowski, M.; Skurski, P.; Simons, J., Dipole-Bound Anions of Glycine Based on the Zwitterion and Neutral Structures. *J. Am. Chem. Soc.* **2000,** *122*, 10159-10162.

28. Sawicka, A.; Anusiewicz, I.; Skurski, P.; Simons, J., Dipole-Bound Anions Supported by Charge-Transfer Interaction: Anionic States of $H_nF_{3-n}N$ --> BH_3 and H_3N --> BH_nF_{3-n} (n=0,1,2,3). *Int. J. Q. Chem.* **2003,** *92* (4), 367-375.

Chapter 6: Photodynamics of $N_2O_2^-$ in the Near UV: Photodissociation and Autodetachment of NO^-

6.1. Introduction

Nitrogen and oxygen containing species such as NO and N_2O play an important role as intermediates in atmospheric processes, and are key components in the production of ozone.[1-3] Because of their critical role in the ozone cycle, it is important to understand the energetics of these systems individually as well as in small molecular clusters.[4, 5] Unlike larger clusters, the nitric oxide dimer $(NO)_2$ has been determined to have bound states for both the neutral and anion through experimental[6-10] and theoretical[11-13] studies, with NO and N_2O observed as dominant dissociation products. In the present study, the photodissociation of $N_2O_2^-$ has been examined in the near ultraviolet (388 nm, 3.20 eV), revealing photodissociation pathways that provide new insights into the anion energetics and dissociation dynamics for this system. The observed products include a mass-symmetric NO ($^2\Pi_g$) + $NO^-(^3\Sigma^-)$ channel, as well as a mass-asymmetric photodissociation N_2O ($^1\Sigma$) + $O^-(^2P)$ channel. Photodissociation producing vibrationally excited $NO^-(^3\Sigma^-)$ states was observed, followed by autodetachment of NO^-. Photoelectron-photofragment coincidence measurements of the autodetachment process revealed the coupling of vibrational and rotational excitation of these short-lived product states.

Posey and Johnson were the first to identify three distinct $N_2O_2^-$ anions using anion photoelectron spectroscopy.[6] The isomers were formed through different precursor preparation methods and were characterized as an $O_2^-(N_2)$ cluster, a C_{2v}-$N_2O_2^-$ anion, and a *cis/trans*-$ONNO^-$ anion. At photon energies of 2.33 eV and 3.50 eV, photodissociation

was the only mechanism observed for the C_{2v} anion and the *cis/trans* isomers.[6] Snis and Panas studied these anion states theoretically and predicted *trans* anion to be 0.35 eV lower in energy than C_{2v}-$N_2O_2^-$ anion and thus the ground state structure of the anion.[11] Infrared spectra of $N_2O_2^-$ anions in argon were able to isolate the *cis* and *trans* isomers with stretching modes in agreement with the theoretical predictions.[14-16] These relative anion energetics have also been supported by other theoretical and experimental studies.[17-19] Hiraoka *et al*. contested the assignment, finding the C_{2v} state as the lowest energy isomer, but more recent experimental and theoretical studies are more consistent with the calculations of Snis and Panas.[12]

Further studies of the photodetachment of $N_2O_2^-$ have also been carried out using anion photoelectron spectroscopy.[4,7,10] Using photon energies of 4.66 and 5.82 eV, Arnold and Neumark assigned the photoelectron spectra to photodetachment of the C_{2v} anion to the $^3A_2$ and $^3A_1$ states of the neutral molecule.[7] The higher photon energies were necessary to access these states, because the neutral N_2O_2 is higher in energy than the photodissociation channels by almost 2 eV.[8] These results also claimed that the C_{2v} structure of the anion is the ground state.[7, 12] Pichugin *et al*. also measured the photoelectron spectrum and reported that the C_{2v} anion was the dominant anion formed, but made no predictions about the relative anion stabilities.[10] Photodissociation to $N_2O + O^-$ with a second photon photodetaching O^- was observed at 3.49 eV and photodetachment to neutral N_2O_2 was observed at 4.66 eV.[10] The neutral states examined in these studies are inaccessible at the photon energy of 3.20 eV that was used in the present work, where only photodissociation processes were observed.

Photofragment translational spectroscopy measurements of the photodissociation of $N_2O_2^-$ were carried out by Osborn *et al.* using photon energies from 2.18 to 2.48 eV and also observed mass-symmetric and mass-asymmetric dissociation pathways, $NO^-(v>0)$ + NO and O^- + N_2O.[8] These results were interpreted in the context of the C_{2v} anion isomer.[8] These photodissociation pathways were in agreement with the photoelectron spectra of Posey and Johnson.[6] Osborn *et al.* determined that while Posey and Johnson's photoelectron spectra only observed photodetachment of NO^- in its ground vibrational state from the *cis/trans* anion, it was very possible that vibrationally excited NO^- was also being produced, but not observed due to the low energy cutoff of their spectrometer.[8] The asymmetric photodissociation has been reproduced by multiple studies and assigned to the C_{2v} anion.[8,10,16]

Photodissociation experiments have also been conducted on neutral N_2O_2, resulting in the observation of highly rotationally excited products.[20,21] These experiments observed photodissociation to both NO($X^2\Pi$, v=0,1) and NO($A^2\Sigma^+$, v=0,1), with significant rotational excitation.[20,21] The high levels of rotational excitation indicated that the photodissociation dynamics partitioned large amounts of energy into internal excitation. A kinematic model was applied and it was determined that at high rotational states, corotating or counterrotating in-plane dissociation occurred depending on the rotational state accessed.[20] Because of the instability of NO^-, comparable levels of rotational excitation have not been previously observed.[22]

Photoelectron spectroscopy studies have determined that NO has an adiabatic electron affinity of 0.026 eV.[10, 23] The first six vibrational states of the ground state neutral are produced in a Franck-Condon distribution by photodetachment, due to the significant

geometry change between NO^- and its corresponding neutral (1.27 Å vs 1.15 Å, respectively).[22, 23] Photodetachment has not been observed from vibrationally excited NO^- due to the short lifetimes prior to autodetachment.[22-24] Vibrationally excited NO^- states have been observed through electron scattering experiments as long-lived autodetaching Feshbach resonances.[22, 25, 26] Electron scattering studies found the first six vibrational levels of the NO^- anion to be ~0.16 eV apart.[25, 27, 28] However, in an electron scattering study on NO clusters, Chu *et al.* observed vibrational structure ~0.19 eV apart.[29] Because of the short lifetime of free vibrationally excited NO^-, it was asserted that an intermediate, tentatively assigned to $N_2O_2^-$, was contributing to the stabilization of the NO anion states.[29] Ion beam infrared (IR) photodestruction measurements have been used to observe the fundamental autodetachment resonance of $NO^-(v=0) \rightarrow NO^-(v=1)$, with the width indicating a lifetime of 350 fs for $NO^-(^3\sum^-, v=1)$ in the temperature range of 300-500 K. In more recent IR photodestruction measurements of rotationally colder jet-cooled NO, the lifetime of $NO^-(^3\sum^-, v=3)$ was found to be ~220 fs, with much shorter lifetimes for the $NO^-(v=4,5)$ and $NO^-(^1\Delta, v=0)$ states.[22, 30]

Photoelectron-photofragment coincidence (PPC) spectroscopy is a technique that combines photoelectron spectroscopy with photofragment translational spectroscopy to provide a kinematically complete measurement of the dynamics occurring in dissociative photodetachment and some ionic photodissociation processes. $N_2O_2^-$ has been studied previously using PPC spectroscopy at a photon energy of 4.66 eV with mass-symmetric and mass-asymmetric dissociation pathways observed (henceforth referred to as symmetric and asymmetric, respectively).[9] Both the C_{2v} and the *trans*-$ONNO^-$ anions were reported as precursors for the asymmetric and symmetric dissociation pathways, respectively.[9] The

present study uses PPC spectroscopy at a lower photon energy of 3.20 eV, below the photodetachment threshold, resulting in the observation of ionic photodissociation followed by either autodetachment or photodetachment of anion product states. The implementation of a cryogenic octopole accumulation trap (COAT) has given greater control over the precursor anions produced, an important consideration for a system with many low-lying anion isomers.[31]

6.2. Experimental Methods

In an attempt to form a variety of anion precursors, glyoxal, HOCCOH, was seeded in neat nitrous oxide.[32] The glyoxal solution (Acros Organics, Inc., 40 wt. % in water) was chilled to 4° C for 18 hours while being dehydrated with 3 Å molecular sieves in a 1:1 ratio. The extracted liquid was then placed in a sample holder heated to 45° C and seeded with N_2O at 35 psi. This created nitrogen oxide anions and carbon-based anions that were then either photodetached or photofragmented. Sample preparation of isopropanol seeded in neat nitrous oxide was also observed to result in similar precursors.

The PPC spectrometer has been previously described in detail.[31, 33, 34] Anions were generated in a pulsed supersonic expansion with a pulsed discharge at 10 Hz and crossed with a 1 keV electron beam. The anions produced were then focused into the cryogenic octopole accumulation trap (COAT) using a Wiley-McLaren time-of-flight spectrometer.[35] The anions were collisionally cooled at 17 K with buffer gas (80:20 He/H_2 mix) for 40 ms inside COAT. The ion packet was accelerated to 7 keV before being re-referenced to ground with a potential switch and separated by time-of-flight.

The ion packet was then injected into a cryogenic electrostatic ion beam trap (EIBT) where it oscillates for 100 ms while being crossed with a 1037 Hz picosecond pulsed Ti:Sapphire regenerative amplifier (Clark-MXR CPA-2000) at a photon energy of 3.20 eV.[33] These measurements were carried out using a 0.5 m focal length lens for high power measurements ($2x10^{11}$ W/cm^2) and a 2.5:1 telescope for the low power measurements ($2x10^9$ W/cm^2) to confirm two-photon events. Photoelectrons were extracted orthogonal to the ion beam and focused using velocity map imaging. A time-and position-sensitive detector was used to measure the electron kinetic energy (eKE) of the photoelectrons. The neutral particles, no longer held by the potential of the EIBT, were then collected in coincidence with the electrons at a multi-particle time-and position-sensitive detector in line with the original ion beam 1.31 m from the interaction region. The time and position data from the neutrals allowed calculation of the kinetic energy release (KER) of the fragmentation. The electron detector was calibrated using O_2^- giving a resolution of ΔeKE/eKE ~4% and the neutral detector was calibrated using O_4^- giving a resolution of ΔKER/KER ~10%.

Historically, PPC spectroscopy has been used on a single precursor anion mass, but because each of these particles are measured in coincidence, multiple anions with a range of mass-to-charge ratios can be collected simultaneously.[36] Multi-mass collection is possible due to the high resolution anion mass separation that is achieved by using the electrostatic ion beam trap (EIBT).[37] Both stable and dissociative channels can be distinguished from the different species collected in multi-mass mode. Using the coincidence detection of the neutral photoproducts or photofragments to disentangle the different photoelectron spectra for each species. In the experiments reported here, the anion

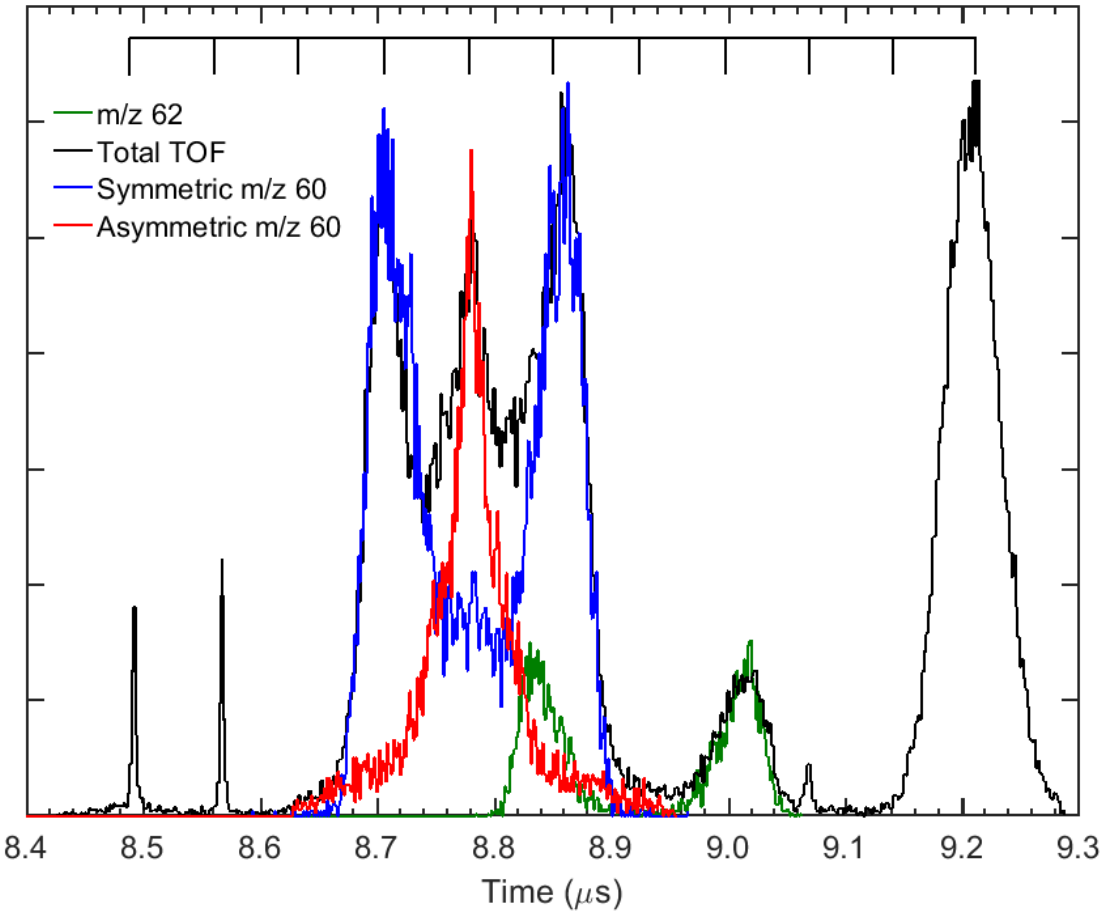

Figure 6.1. Neutral particle time of flight for the six different species measured in this study. The highest intensity distribution is attributed to 60 amu, N_2O_2. The blue trace indicates the symmetric dissociation, while the red trace shows the asymmetric dissociation for 60 amu. The data for 62 amu has been disentangled from the 60 amu data, and can be seen in green.

source produced six different singly charged anions in the range of 56-66 amu. The six different species that were observed are shown in the time-of-flight spectrum for the neutral fragments in Figure 6.1 where the mass-to-charge ratio of the anion is determined by the neutral flight time from the interaction region to the multi-particle time and position sensitive neutral detector given the 7 keV beam energy. The first two stable neutral products, mass 56 and 57, have been determined to arise from photodetachment of the oxyallyl anion, $C_3H_4O^-$, and the acetone enolate anion, $C_3H_5O^-$, respectively and were discussed in a previous publication.[38] The most intense signal, centered at 60 amu, arises from the photodissociation of $N_2O_2^-$. The data at 62, 64 and 66 amu were also observed after photodetachment or photofragmentation and are the result of other nitrogen oxide species that will be expanded upon in later publications.

6.3. Results

Figure 6.2 shows the mass distribution of the neutral products centered at 60 amu after photofragmentation. This indicates that at least two product channels exist, a high intensity symmetric dissociation as well as a lower intensity asymmetric dissociation. Unfortunately, the mass resolution for the photofragments is unable to distinguish nearby product channels, such as 16/44 (O/N_2O) vs. 14/46 (N/NO_2). The asymmetric dissociation has been attributed to $N_2O + O$ based on the energetics for this system, and the observation of the photodetachment of O^- in the coincidence photoelectron spectrum. Figure 6.3(a) shows the total photoelectron spectrum collected for $N_2O_2^-$ at 3.20 eV. Each electron is measure in coincidence with its neutral photofragments and represented in a coincidence spectrum. The coincidence spectra are resolved based on the mass distribution from Figure 6.2 as either symmetric dissociation, shown in Figure 6.4, or asymmetric dissociation, as

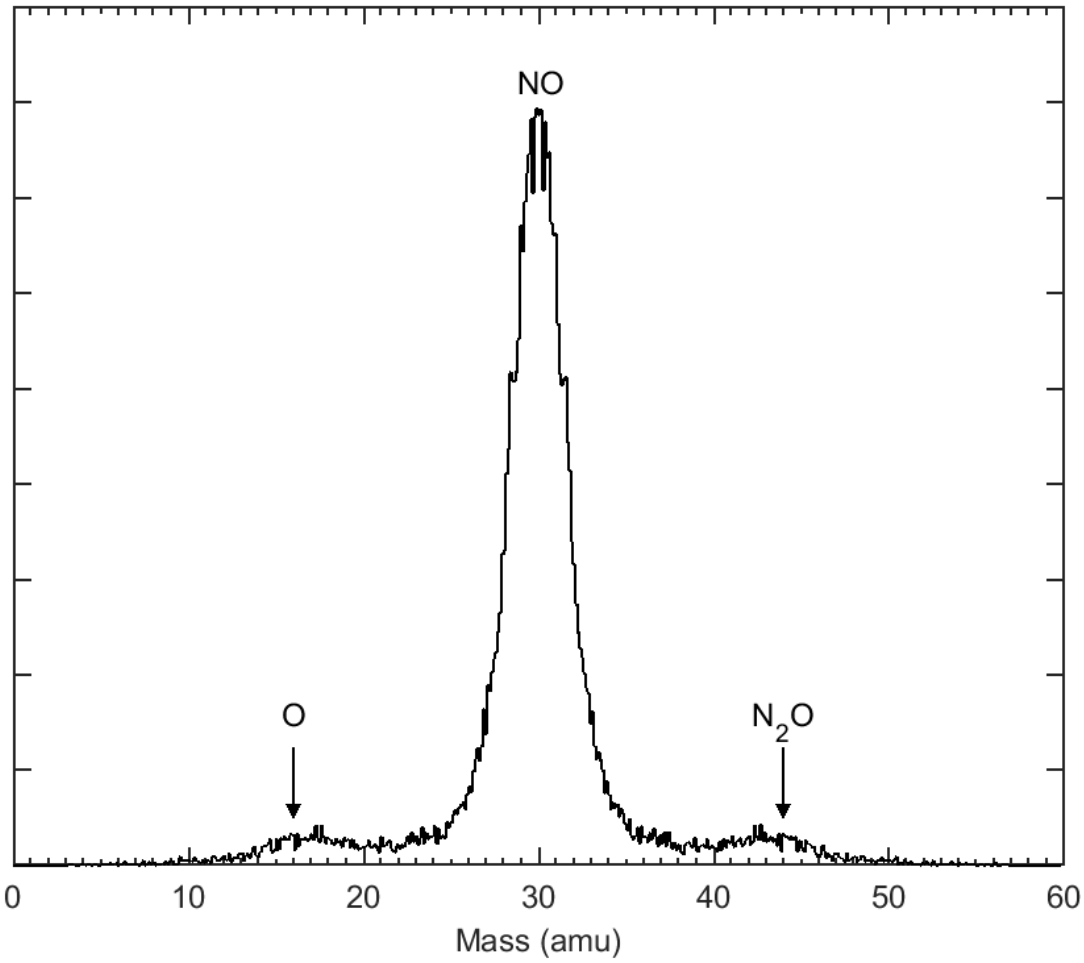

Figure 6.2. Mass spectrum showing the neutral particle product distribution for 60 amu. This is dominated by symmetric dissociation, assigned to NO + NO, but asymmetric channels, assigned to O + N_2O respectively, were also observed. The asymmetric channel in the mass spectrum relies on the photodetachment of O^- by a second photon for detection, and thus is much lower than expected from the time-of-flight spectrum in Figure 6.1.

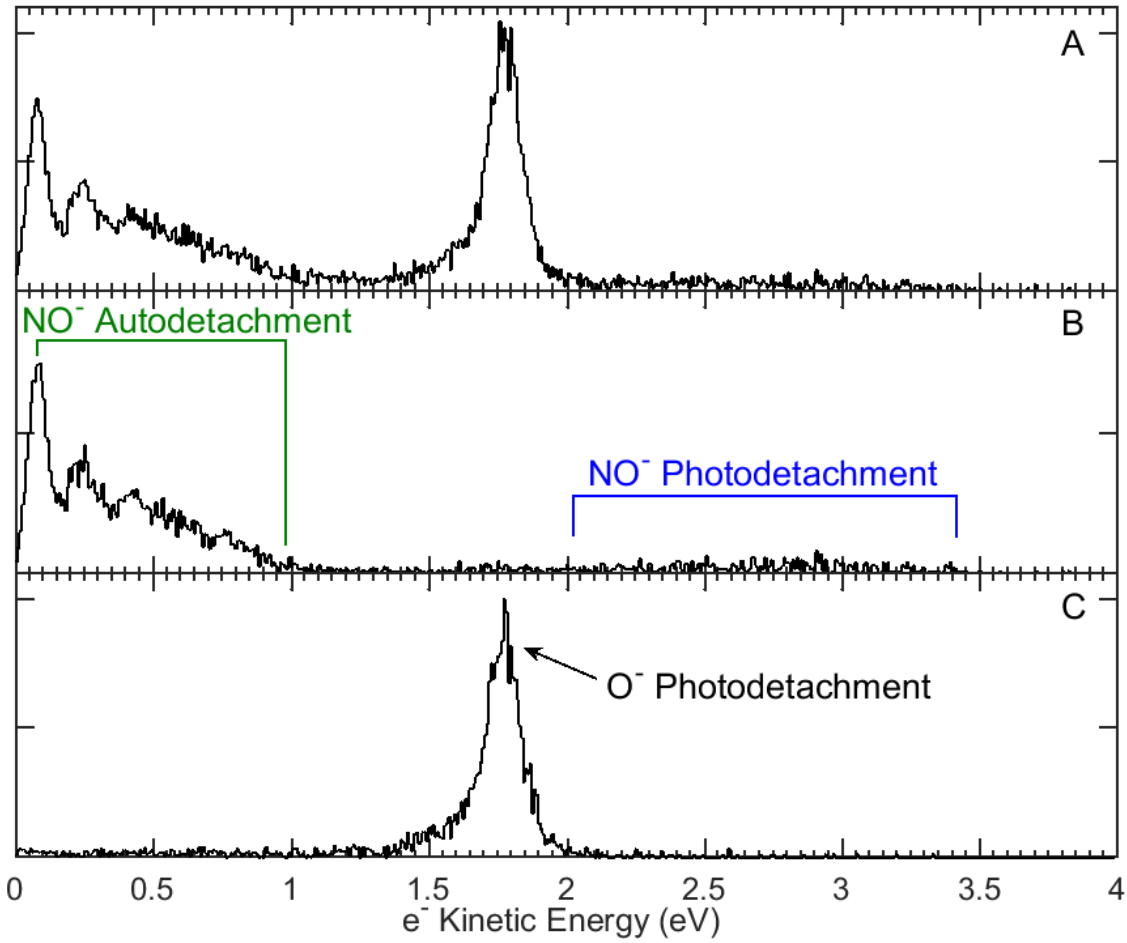

Figure 6.3. A.) Total photoelectron spectrum for the three dissociation channels at $E_{h\nu}$ = 3.20 eV. B.) Photoelectron spectrum for the symmetric dissociation. C.) Photoelectron spectrum for asymmetric dissociation.

seen in Figure 6.5. Three individual photodissociation channels were observed in this study, (A), symmetric photodissociation and autodetachment of $N_2O_2^-(^2A_u) + h\nu \rightarrow NO(^2\Pi_g) + NO^-(^3\Sigma^-)$ $(v>0) \rightarrow NO(^2\Pi_g) + NO(^2\Pi_g) + e^-$, (B) a symmetric photodissociation and sequential photodetachment of $N_2O_2^-(^2A_u) + h\nu \rightarrow NO(^2\Pi_g) + NO^-(^3\Sigma^-)$ $(v=0) + h\nu \rightarrow NO(^2\Pi_g) + NO(^2\Pi_g) + e^-$, and (C) an asymmetric photodissociation and sequential photodetachment of $N_2O_2^-(^2A_u) + h\nu \rightarrow N_2O(^1\Sigma) + O^-(^2P) + h\nu \rightarrow N_2O(^1\Sigma) + O(^3P) + e^-$.

6.3.1. Symmetric Photodissociation and Autodetachment

The dominant signal in the symmetric photoelectron spectrum can be seen below 1 eV in Figure 6.3(b). Because a symmetric dissociation was observed to result in, $NO^-(v=0)$, (discussed in Section 6.3.2) as well as $NO^-(v>0)$, this photodissociation was attributed to *trans*-ONNO $\rightarrow NO(^2\Pi_g) + NO^-(^3\Sigma^-, v>0)$. In the photoelectron spectrum, Figure 6.3(b), the peaks observed are attributed to $NO^-(v=1,2,3)$ autodetachment. A continuum can be seen to span the energy range of $NO^-(^3\Sigma^-, v=4\text{-}7)$, indicating that these states may also be accessed, but were not resolved due to a combination of anion electronic states accessible. The $NO^-(^3\Sigma^-, v=5)$, has previously been observed to be nearly degenerate with the $NO^-(^1\Delta, v=0)$, so the involvement of electronically excited NO^- also cannot be ruled out.[30] The short-lived vibrational states of the NO^- anion undergo spontaneous electron ejection in order to reach the more energetically stable NO neutral due to the small electron affinity of NO in relation to the energy of these vibrational states. A large KER from dissociation was seen in coincidence with the vibrational progression below 1 eV in the photoelectron spectrum, as seen in the coincidence plot in Figure 6.4, consistent with a direct photodissociation on a repulsive excited state. These autodetachment features are seen as horizontal bands in the coincidence plot. A kinetic energy maximum (KE_{max}) can

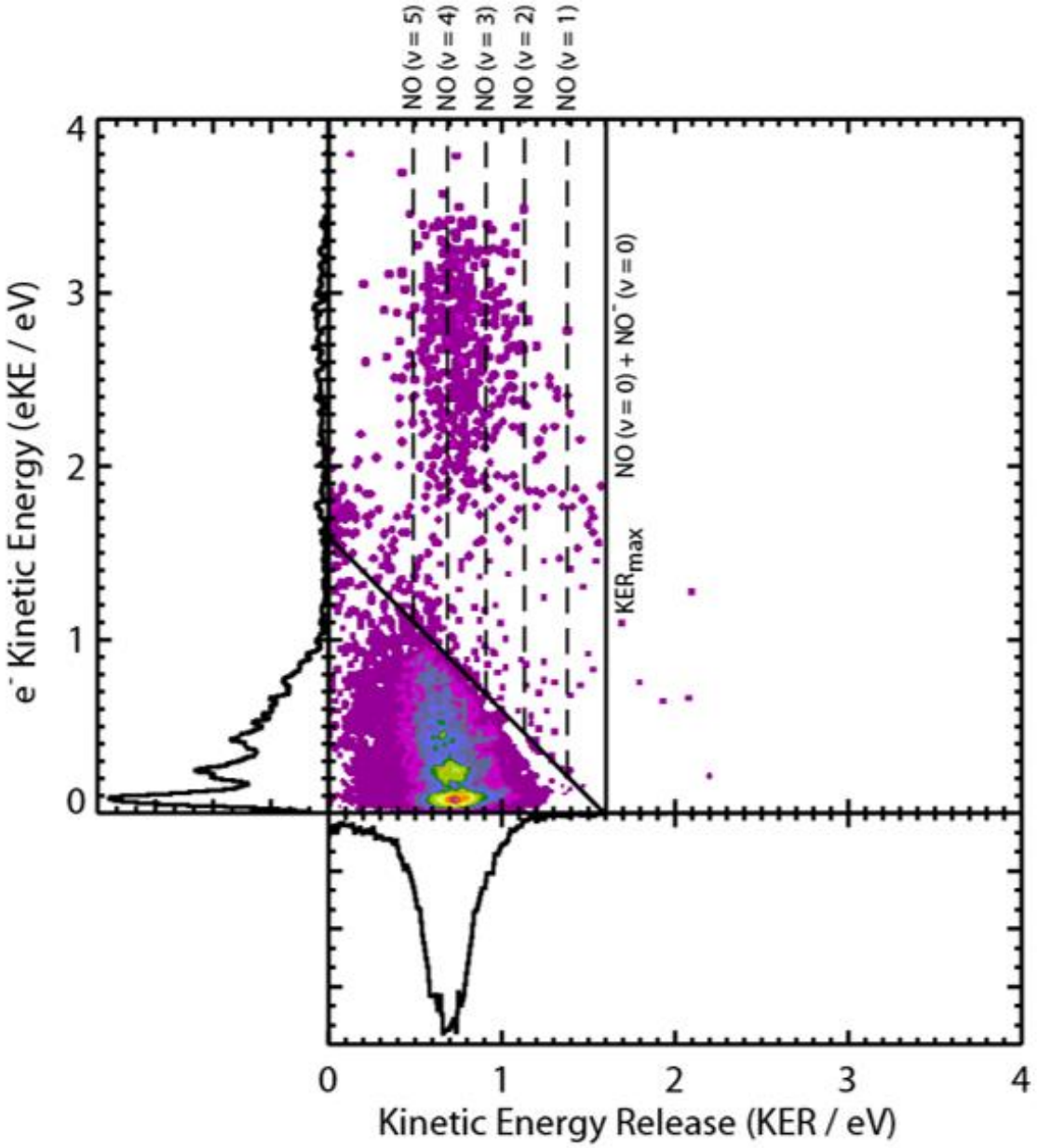

Figure 6.4. Coincidence plot for $N_2O_2^-$ + hν → NO + NO^- + hν → NO + NO + e^- dissociation channel. The kinetic energy release maximum (KER_{max}) associated with the photodissociation of $N_2O_2^-$ is shown for the ground state NO anion channel. The vibration levels of NO are shown as dashed lines. A diagonal line indicates the kinetic energy maximum for the autodetachment channel.

be seen at 1.6 eV in Figure 6.4. This indicates that the autodetached products are all reaching the same final neutral state. This KE_{max} corresponds to the NO(v=0, J=0) + NO(v=0, J=0) + e^- product state. Figure 6.5 shows the Gaussian fits be seen at 1.6 eV in Figure 6.4. This indicates that the for the first five autodetachment features, with the centers, widths and amplitudes given in Table 6.1. These autodetachment features are in reasonable agreement with previous measurements of NO^- autodetachment in electron scattering experiments and are the first observation of the dissociation dynamics for this symmetric photodissociation-autodetachment channel.[26-29]

The coincidence spectrum shows that the features at lower eKE increasingly deviate from the KE_{max}, indicating that in the lower $NO^-(v)$ states a dynamical constraint prevents the formation of products with no internal excitation. However, the higher vibrational autodetachment states do match this KE_{max}, indicating the final product state for these autodetachment features is NO(v=0) + NO(v=0) and that the that unaccounted for energy in the lower autodetachment peaks is due to either rotational or vibrational excitation. Unambiguous evidence for rotational excitation is most strongly observed in $NO^-(v=1)$ feature, which is seen as the slight increase in eKE at high KER. This is attributed to high rotational excitation in NO^- fragments with lower KER. The eKE for the autodetachment features decrease as the rotational state increases because the difference in rotational constants causes $NO^-(v=1, J) \rightarrow NO(v=0, J+1, J-1) + e^-$ transition to decrease in energy as J increases. This phenomenon is seen most dramatically in v=1, but was also observed in v=2,3 as an increasing slope in the vibrational bands at higher KER.

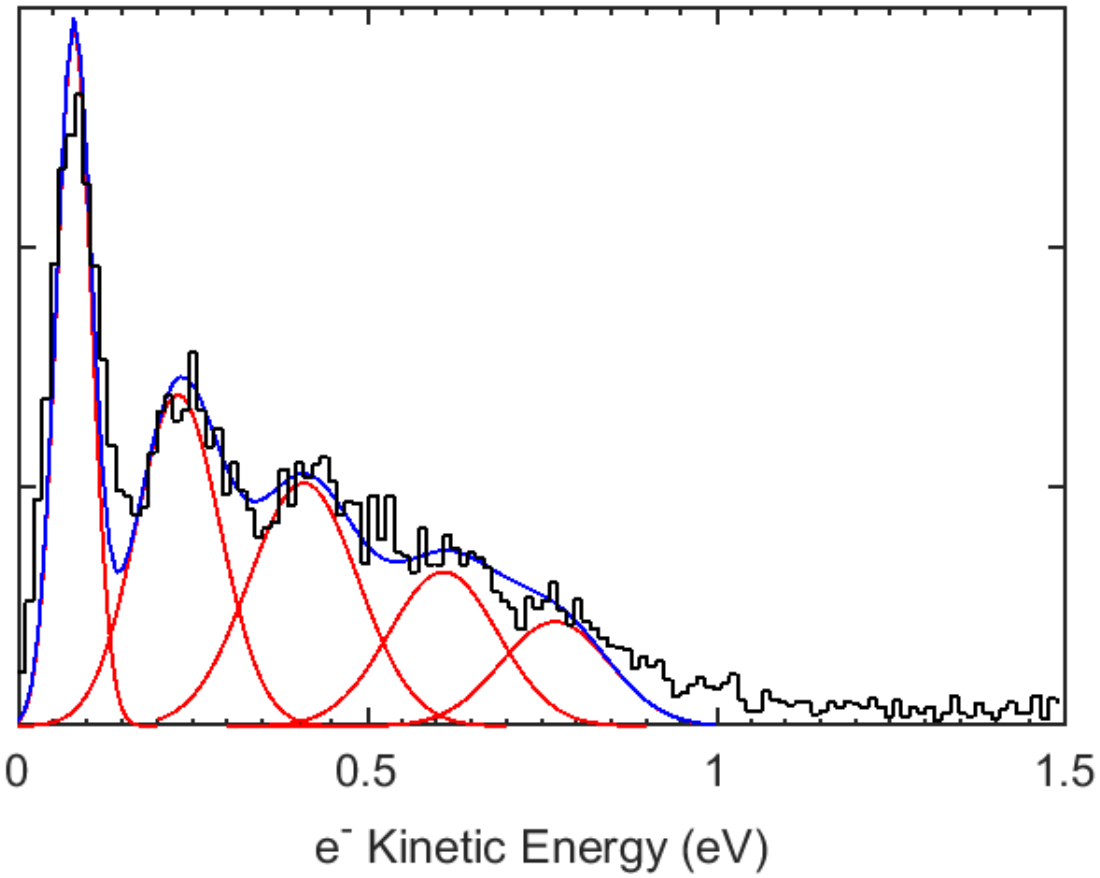

Figure 6.5. The autodetachment peaks in the photoelectron spectrum with Gaussian fits for the different vibrational states

Table 6.1. The values for the Gaussian fits to the autodetachment peaks. The amplitudes are given in arbitrary units for fitting the counts in the experimental spectrum.

v	Center (eV)	Amplitude	FWHM (eV)
1	0.081	1449	0.085
2	0.230	692	0.200
3	0.410	508	0.256
4	0.610	322	0.259
5	0.770	218	0.259

6.3.2. Symmetric Photodissociation and Sequential Photodetachment

The symmetric photodissociation in channel A can also result in $NO^-(v=0) + NO(v)$ products. Because there is a significant geometry change from the anion to the neutral, vibrational excitation is favored in the products, and the $NO^-(v=0)$ channel has significantly lower intensity. The NO^- anion in the ground vibrational and rotational state is stable relative to photodetachment by 0.026 eV, requiring a two photon process to photodetach to the neutral state.[23] The focusing of the laser was changed to reduce the power density by two orders of magnitude, and this channel was suppressed, confirming this as a sequential photodetachment process. In Figure 6.3(b), this signal is observed in the photoelectron spectrum above 2 eV. This channel spans the same energy as the photodetachment of free NO^- anion although the vibrational progression normally resolved for NO^- is not observed due to the low signal from this channel. In photodissociation followed by sequential photodetachment, a KER_{max} is observed as a vertical limit. Sequential photodetachment indicates that the $NO^-(v=0)$ is formed, therefore deviations from the KER_{max} must be the result of internal (vibrational and rotational) excitation in the neutral NO fragment. For a system such as NO where the vibrational states are well studied[23,39], the KER limits can be plotted for each vibrational transition, as seen in the coincidence plot in Figure 6.4. Qualitatively, assuming no rotational excitation, the distribution indicates that the states accessed in this process are $NO(v=2,3,4) + NO^-(v=0)$. The experimental KER_{max}, is also consistent with this dissociation originating from photodissociation of the *trans*-$ONNO^-$ anion ground state.

6.3.3. Asymmetric Photodissociation and Sequential Photodetachment

An asymmetric photodissociation into $N_2O(^1\Sigma) + O^-(^2P)$ was also observed. This channel is detected in the PPC spectrometer by sequential photodetachment of the O^- anion, forming the neutral product state $N_2O(^1\Sigma) + O(^3P)$. A large KER distribution was observed, reaching the KER_{max} at 1.05 eV in Figure 6.6, however, the distribution is observed to peak near 0 eV, a property often associated with statistical dissociation of excited ground state molecules. This asymmetric dissociation is observed in the photoelectron spectrum, Figure 6.3(c), as a strong signal at 1.74 eV, corresponding to the photodetachment of O^- at a photon energy of 3.20 eV. The focusing of the laser was changed so that the power density was two orders of magnitude lower, and the features attributed to this asymmetric dissociation were suppressed, confirming the two-photon process. The neutral channel $N_2O(^1\Sigma) + O(^3P)$ is slightly above threshold for the photon energy of 3.20 eV, as seen in the energetic diagram in Figure 6.7, resulting in a second photon being required to photodetach to the neutral state.

At low eKE, signal can be seen below 1 eV in the asymmetric coincidence plot (Figure 6.6). This is possibly attributed to the $N + NO_2^-$ channel, which would be energetically accessible, but require significant rearrangement from the *trans*-$ONNO^-$ isomer. The low eKE signal matches well with the KER_{max} that would be expected from this channel (as seen in Figure 6.7) as well as the electron affinity, but without a more significant signal, this cannot be definitively assigned. Li *et al.* saw possible evidence for this channel with PPC spectroscopy, but were also inconclusive in their assignment of this less favored product channel.[9]

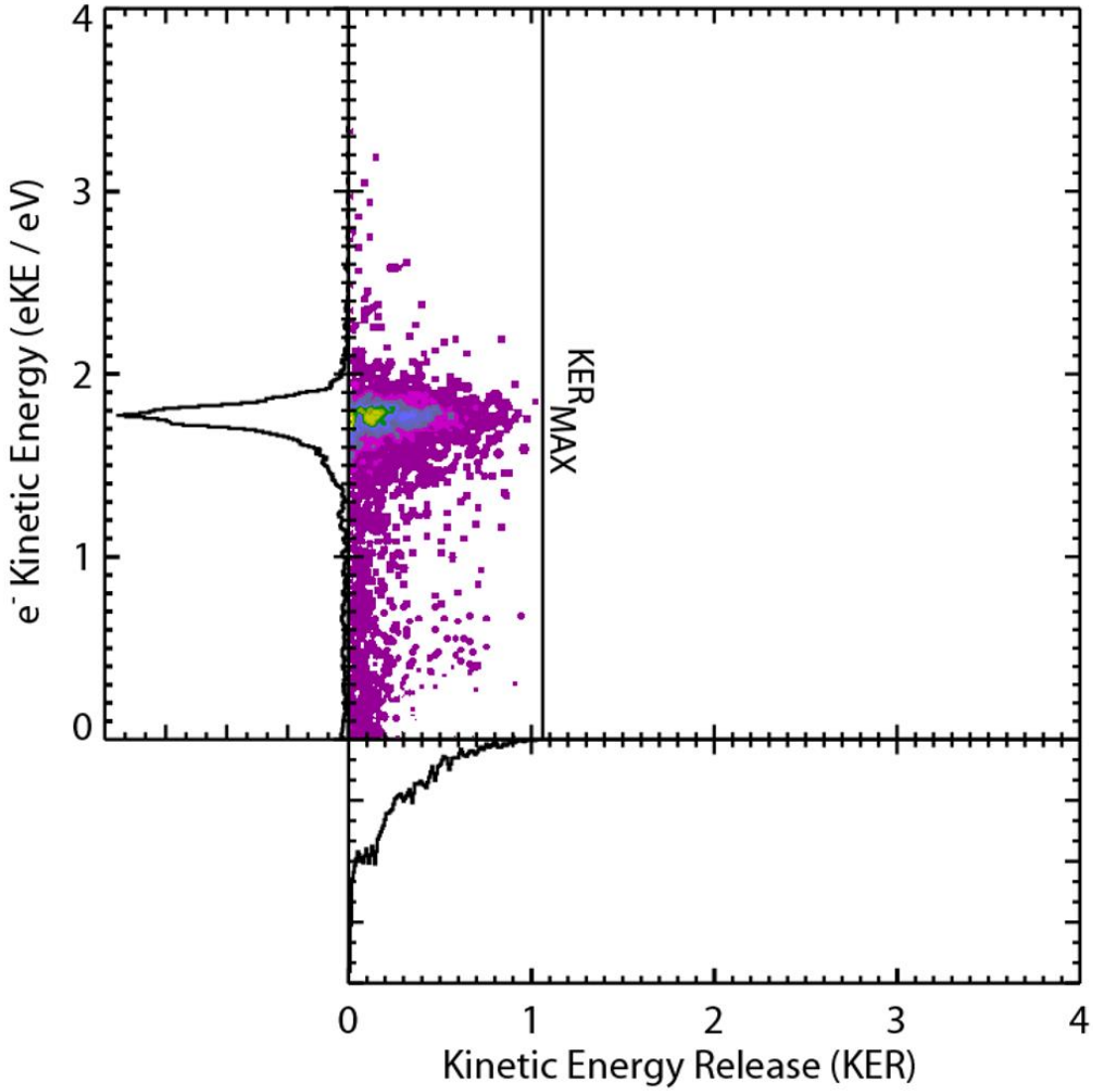

Figure 6.6. Coincidence plot for $N_2O_2^- + h\nu \rightarrow N_2O + O^- + h\nu \rightarrow N_2O + O + e^-$ dissociation channel. The kinetic energy release maximum (KER_{max}) associated with the photodissociation of $N_2O_2^-$ is shown.

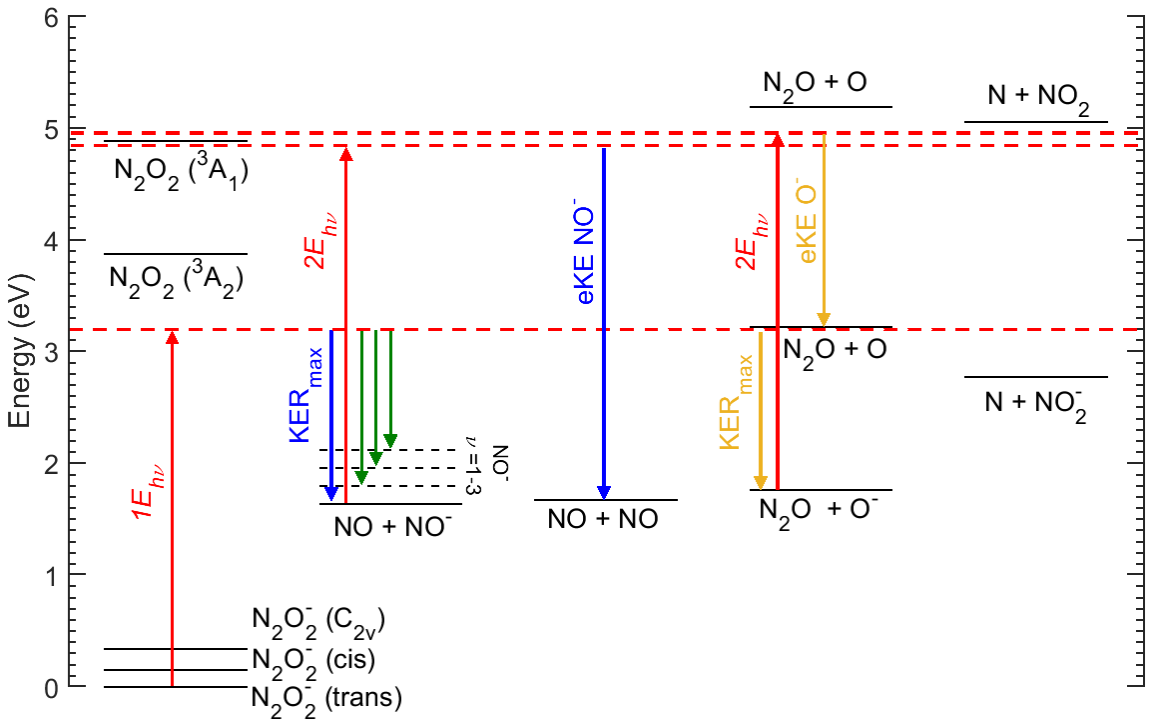

Figure 6.7. Energetics for $N_2O_2/N_2O_2^-$ system, including the neutral states and the photodissociation product channels accessible at $E_{h\nu}$ = 3.20 eV. Channel A is represented in green, channel B in blue and C in yellow.[7-9,11,22]

6.4. Discussion

Due to the experimental KE_{max} and KER_{max}, as well as the relative anion energetics from Snis and Panas, the photodissociation processes observed in this study are assigned to the ground state *trans*-$ONNO^-$ anion, as shown in the energetics in Figure 6.7.[11] This is contrary to previous observations that indicate the C_{2v}-$N_2O_2^-$ anion is made from neat N_2O.[6,7,8] However, these anions have been observed to undergo rearrangement with isotope scrambling, which could result in the lower energy anions being produced through rearrangement.[40] A cryogenic octopole accumulation trap is used in this study to cool anions to their most stable states, a process that could have facilitated rearrangement.[31] The *trans*-$ONNO^-$ anion has been calculated to be more stable than the C_{2v} state by 0.35 eV and has been associated previously with both symmetric and asymmetric dissociation channels.[6, 9, 11] The *trans*-$ONNO^-$ anion is the only isomer that has been observed to undergo symmetric dissociation resulting in $NO^-(v=0)$, further supporting the precursor anion assignment.[8] Previous studies have claimed to observe the higher energy C_{2v} anion more frequently, however, no specific evidence for this isomer was observed in this study.[8,11]

Previous studies of this system have had some debate over the bond dissociation energy of the C_{2v} anion. Osborn *et al.* and Arnold *et al.* both agree that the C_{2v} anion is about 1.40 eV more stable than the dissociation channel of NO + NO^-. [7,8] Li *et al.* who reported that this dissociation is closer to 1.01 eV.[9] The bond dissociation energy of the *trans* anion was determined by Li *et al.* to be 1.70 eV, which was supported by calculations from Snis and Panas.[9,11] While Arnold *et al.* assumed that the C_{2v} anion was the ground state, Osborn *et al.* calculated that the *trans* anion was ~0.05 eV below the C_{2v} state

separated by an unknown barrier.[7,8] While it is possible that the C_{2v} isomer was accessed in the earlier photodissociation experiments, no comparison to photodissociation of the other isomers was reported.[8] The symmetric and asymmetric photodissociation channels from this study are in agreement with the predictions from Li *et al.*, however due to a lack of observation of the C_{2v} isomer in the current study, the discrepancy in the relative energy of the C_{2v} anion remains open for debate.

6.4.1. Symmetric Photodissociation and Autodetachment

Within the NO^- electron kinetic energy (eKE) spectrum, Figure 6.5, a vibrational progression can be seen with broadening observed in higher vibrational levels before autodetachment. This is expected to be a result of the shorter lifetimes of these vibrational states. A continuum is observed after the $NO^-(v=3)$ peak and spans the energy range for $NO^-(^3\Sigma^-, v=4\text{-}7)$. In the coincidence plot, the resolved autodetachment peaks exhibit a slight increase in eKE at high kinetic energy release (KER). Conservation of energy forbids an increase in both the eKE and the KER simultaneously, indicating that significant rotational excitation must be present in products at lower KER, (0.6 eV-0.8 eV). Above 0.8 eV, the eKE begins to slightly increase. For a given set of product vibrational states, energy conservation dictates that this region corresponds to decreasing rotational excitation. As discussed below, this shift to higher eKE is a result of the larger rotational constant of NO compared to NO^-. This is most clearly observed in the $NO^-(v=1)$ feature and can also be seen in the $NO^-(v=2)$ products.

The rotational states for each of the autodetachment vibrations has been calculated using known rotational constants and can be seen in Figure 6.8. For the eKE, the energy

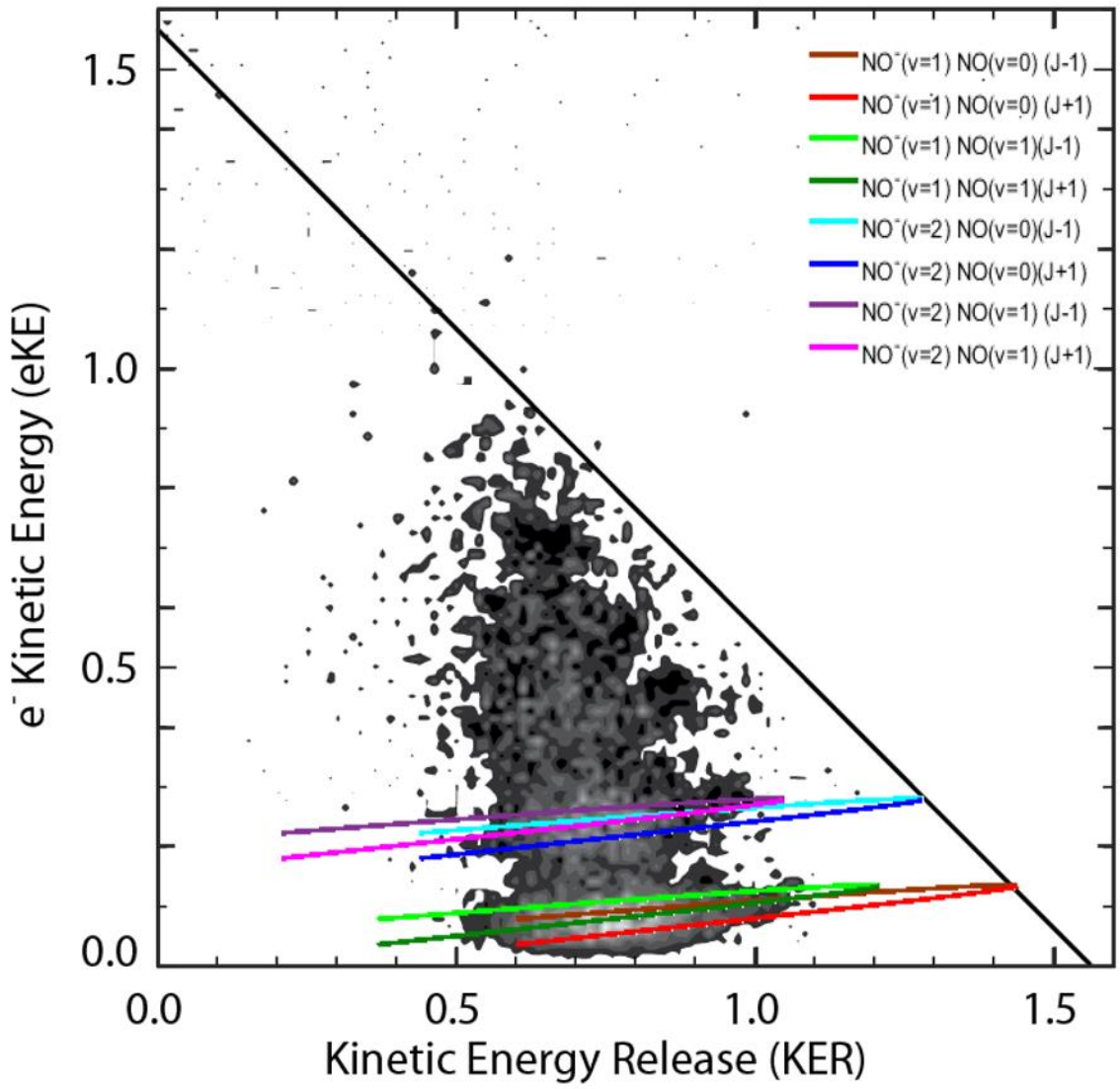

Figure 6.8. The coincidence plot for the autodetachment channel with rotational calculations. For the eKE, both J+1 and J-1 were calculated for the anion state. In the KER, it was assumed that J=J. These were calculated for both $NO^-(v=x)$ + $NO(v = 0)$ and $NO^-(v=x)$ + $NO(v = 1)$.

autodetaching vibrational state. Demyanenko *et al.* were able to show in neutral ONNO that for high rotational levels an in-plane dissociation occurred, therefore it was also assumed that L is negligible and (J=J) for the two NO fragments in the KER.[20] Vibrational partitioned into rotation was calculated for both $NO^-(J+1)$ or $NO^-(J-1)$ transitions for each energy partitioned into the spectator fragment was also considered, therefore $NO^-(J+1, J-1)$ + NO(v=0) as well as the $NO^-(J+1, J-1)$ + NO(v=1) transitions are shown for $NO^-(v=1,2)$ in Figure 6.8. These considerations are consistent with the population of either $NO^-(v=1)$ + NO(v=0) rotational states greater than J = 20 or $NO^-(v=2)$ + NO(v=0) rotational states greater than J = 15.[41, 42] Angular momentum constraints in the dissociation prevent the formation of lower energy rotational states, resulting in the signal in the coincidence spectrum deviating away from and below the KE_{max} as eKE approaches zero. Due to the energy resolution of the coincidence plot, it is possible $NO^-(v=1, 2, J+1, J-1)$ + NO(v=0) as well as the $NO^-(v=1, 2, J+1, J-1)$ + NO(v=1) are all populated, though from the KE_{max} observed, it is most likely that the final product states of both NO fragments are in their ground vibrational state. Highly rotationally excited products are supported by the impulse model for dissociation of the *trans* anion, which will be discussed further below.[43,44]

An impulse model has been used to predict the energy partitioning in dissociation processes into translational, vibrational and rotational energy based on the bond angle of the molecule, and the total energy available.[43,44] Using the bond angle of 111.4˚, calculated by Snis and Panas, and the experimental KE_{max} as the total energy, when 0.75 eV of energy is partitioned into translation, 0.37 eV would be partitioned to rotational energy in a single fragment.[11] The remaining energy, 0.05 eV, would be partitioned into vibration. As

mentioned previously, an increase in eKE is not observed from 0.6-0.8 eV in the KER, indicating that significant rotational excitation is present in this range. This rotational excitation is expected at low eKE and KER due to the large amount of energy available from the $N_2O_2^-$ photodissociation. Higher vibrational excitation can be seen to match well with the experimental KE_{max}, indicating that the rotational energy contribution becomes negligible.

The separation of the autodetachment peaks was observed to be ~0.15-0.20 eV, which is consistent with previously measured NO^- anion vibrationally excited states. Spence and Schulz were able to measure the vibrational levels (v=1-7) of NO^- using elastic scattering experiments and observed a separation of ~0.16 eV.[27] The discrepancy between these values and the vibrations observed in this study can be attributed to the broadening and shifting from the extensive rotational excitation. The NO^- (v=1-3) autodetachment peaks at lower KER in the coincidence spectrum are shifted to slightly lower eKE as a result of product rotational excitation. A shift of the same magnitude is not possible for the higher NO^- (v) autodetachment peaks as more of the energy is partitioned into vibration. While the first three autodetachment peaks are clearly seen, a continuum is observed above NO^-(v=3). While NO^-(v=3) is nearly degenerate with the NO(v=2) state of the neutral, NO^- ($^3\Sigma^-$v=5) are interspersed with the excited NO^- ($^1\Delta$) states that may be produced.[25, 27, 30] The NO^-(v=1) vibrational state has been observed to have a lifetime of 350 fs at 300-500 K, which is too short for a second photon event to photodetach before autodetachment occurs. This has been cited previously as the reason that hot bands for photodetachment of NO^- have never been reported.[23] Other studies with colder ion sources have observed lifetimes of tens of femtoseconds for higher vibrational states.[30]

Because the higher vibrational states are more unstable with respect to the possible neutral transitions, the lifetimes begin to decrease. This can be seen in Figure 6.5, where peak broadening occurs above NO^-(v=2). While a significant change in peak width can be seen in Table 6.1 to occur between NO^- v=1 and 2, the FWHM of the higher vibrational states stays consistent, indicating that these vibrational states have a similar, and very short lifetime. This inference is limited, however, by the fact that these features are unresolved, owing to the broadening in the lower vibrational states from the rotational contributions. Therefore a quantitative lifetime cannot be assigned to these features. The autodetachment channel was observed in the photofragment translational spectroscopy study of Osborn *et al.*, where it was assigned to originate from the C_{2v} anion precursor, based on the use of sample preparation methods reported by Posey and Johnson.[6] However, Osborn *et al*. were not able to reproduce the preparation of the *trans*-$ONNO^-$ from the work of Posey and Johnson.[6,8] It can be difficult to insure the production of various ionic isomers in different ion sources, and in any case, the present results are best explained by production of the ground state *trans*-$ONNO^-$ anion.

6.4.2. Symmetric Photodissociation and Sequential Photodetachment

The same KER distribution can be seen in the NO^-(v=0) data at high electron kinetic energy. As the coincidence spectrum in Figure 6.4 shows, this channel has the same KE_{max} as the lower eKE distribution, meaning that the final NO + NO product distribution that is being accessed is the same. The photoelectron spectrum for this higher energy distribution spans the same energy range as the photodetachment of free NO^- anion, but due to low signal, the NO bands are not resolved. Reduction in the laser fluence suppressed this channel, indicating that is it the result of an overall two-photon process where the NO^-

anion is photodetached after photodissociation of the $N_2O_2^-$ anion. This channel is significantly lower in amplitude since vibrationally excited products are more likely to occur.

While Osborn *et al.* also observed this symmetric photodissociation, they did not see any evidence for the $NO^-(v=0)$ observed here. Using buffer gas cooling in COAT internally cools precursor anions before photodissociation (less than 17K as shown in the recent study of O_3^-)[31,34], possibly explaining the observation of lower excitation in the photoproducts in the present work. As noted earlier, the KER for $NO^-(v=0)$ product channel has a KER that is indistinguishable from that of NO^- ($v>0$), given the signal-to-noise in the data. This shows that the NO neutral vibrations produced in coincidence with $NO^-(v=0)$ span a significant range as noted by the KER limits for states annotated on Figure 6.4.[23] These results agree well with the energetics in Figure 6.7.

6.4.3. Asymmetric Photodissociation and Sequential Photodetachment

The asymmetric dissociation from the *trans* anion was first reported by Posey and Johnson.[6] While the asymmetric dissociation was observed in their study at 3.50 eV, it was not seen at 2.33 eV. This channel has also been previously assigned to originating from the C_{2v} $N_2O_2^-$ isomer.[8,9,10] There is a discrepancy of 0.4 eV between the observed 1.05 eV KE_{max} and the predicted 1.45 eV KE_{max} from *trans*-$ONNO^-(^2A_u) \rightarrow N_2O(^1\Sigma) + O(^3P)$. This energy is likely partitioned to vibrational excitation of N_2O during photodissociation. While the *trans*-$ONNO^-$ anion is predicted to have a bond angle of 111.4˚, neutral N_2O is a linear molecule.[10, 45, 46] This large geometry change would result in significant excitation of the ν_2 bending mode of N_2O. Due to the dissociation of the terminal oxygen, the ν_1

stretching mode could also be excited, which is known to have an energy of ~0.27 eV.[45, 46] A combination of these modes could result in the 0.4 eV discrepancy. While this dissociation has been observed from both the *trans* and C_{2v} isomer, photodissociation of the C_{2v} isomer would result in almost 0.8 eV of internal excitation. This is counterintuitive given the lack of symmetric dissociation observed from this higher energy isomer. Based on this information, it would appear that the asymmetric photodissociation is also the result of the *trans* anion isomer, though this assignment is more tentative.

A second asymmetric dissociation is also energetically accessible, as seen in Figure 6.7. This photodissociation channel would result in $N(^4S) + NO_2^-(^1A_1)$ and reach $N(^4S) + NO_2(^2A_1)$ via photodetachment by a second photon. The KER_{max} for this dissociation channel would be about 0.5 eV, which matches well with the low signal data below 1.0 eV in the photoelectron spectrum, as see in Figure 6.6.[9] Signal below 1.0 eV in the photoelectron spectrum is consistent with the electron affinity of NO_2 (EA = 2.27 eV) at this photon energy.[47] Given the low amount of signal and the lack of high-resolution mass separation for different photofragment channels, this assignment cannot conclusively be made.

6.5. Conclusion

The photodissociation of $N_2O_2^-$ was studied at E_{hv} = 3.20 eV with three channels observed; symmetric photodissociation and autodetachment, symmetric photodissociation and sequential photodetachment and asymmetric photodissociation with sequential photodissociation. These distinct dissociations were analyzed separately, giving spectra specific to each of the individual channels. The results are consistent with the existing

dissociation channels observed for this system from the ground state *trans* anion. The implementation of COAT internally cools these precursor anions to their ground states, an explanation for this less studied anion being dominant in this study. These results agree well with the previously assigned photodissociation states that have been observed at different photon energies and from higher energy anion precursors, as well as the theory that exists for this system. This is the first recorded coincidence measurements of $NO^-(v=0)$ photodissociation and provides insight into autodetachment of the highly excited vibrationally and rotationally NO^- anion products.

Chapter six is being prepared for publication, in which the dissertation author is the primary author and the dissertation advisor is the corresponding author. Lunny, K. G., Benitez, Y., Albeck, Y., Strasser, D., Continetti. R. E., "Photodynamics of $N_2O_2^-$ in the Near UV: Photodissociation and Autodetachment of NO^-"

6.6. References

1. Crutzen, P. J., The Influence of Nitrogen Oxides on the Atmospheric Ozone Content. *Quart. J. R. Met. Soc.* **1970,** *96,* 320-325.

2. Logan, J. A., Nitrogen Oxides in the Troposphere: Global and Regional Budgets. *J. Geo. Res.* **1983,** *88* (15), 10785-10807.

3. Ryden, J. C., N_2O Exchange between a Grassland Soil and the Atmosphere. *Nature* **1981,** *292,* 235-237.

4. Tsukuda, T.; Saeki, M.; Zhu, L.; Nagata, T., Formation of $N_3O_3^-$ Anion in $(NO)_n^-$: Photoelectron Spectroscopy and Ab Initio Calculations. *Chem. Phys. Lett.* **1998,** *295*, 416.

5. Tsukuda, T.; Zhu, L.; Saeki, M.; Nagata, T., Photochemistry of $(NO)_n^-$ as Studied by Photofragment Mass Spectrometry. *Int. J. Mass. Spectrom.* **2002,** *220,* 137.

6. Posey, L. A.; Johnson, M. A., Pulsed Photoelectron Spectroscopy of Negative Cluster Ions: Isolation of Three Distinguishable Forms of $N_2O_2^-$. *J. Chem. Phys.* **1988,** *88,* 5383.

7. Arnold, D. W.; Neumark, D. M., Study of N_2O_2 by Photoelectron Spectroscopy of $N_2O_2^-$. *J. Chem. Phys.* **1995,** *102*, 7035.

8. Osborn, D. L.; Leahy, D. J.; Cyr, D. R.; Neumark, D. M., Photodissociation Spectroscopy and Dynamics of the $N_2O_2^-$ Anion. *J. Chem. Phys.* **1995,** *104*, 5026.

9. Li, R.; Continetti, R. E., Studies of the Excited State Dynamics of N_2O_2 by Dissociative Photodetachment of $N_2O_2^-$. *J. Phys. Chem. A* **2002,** *106*, 1183-1189.

10. Pichugin, K.; Grumbling, E.; Velarde, L.; Sanov, A., Solvation-Induced Cluster Anion Core Switching from $NNO_2^-(N_2O)_{n-1}$ to $O^-(N_2O)_n$. *J. Chem. Phys.* **2008,** *129*, 044311.

11. Snis, A.; Panas, I., N_2O_2, $N_2O_2^-$ and $N_2O_2^{2-}$: Structures, Energetics and N-N Bonding. *Chem. Phys.* **1997,** *221*, 1-10.

12. Hiraoka, K.; Fujimaki, S.; Aruga, K., Gas-Phase Clustering Reactions of O_2^-, NO^-, and O^- with N_2O: Isomeric Structures for $(NO\text{-}N_2O)^-$ *J. Phys. Chem.* **1994,** *98*, 8295-8301.

13. Valiev, M.; Lymar, S. V., Structural and Mechanistic Analysis through Electronic Spectra: Aqueous Hyponitrite Radical ($N_2O_2^-$) and Nitrosyl Hyponitrite Anion ($N_3O_3^-$). *J. Phys. Chem. A* **2011,** *115*, 12004-12010.

14. Andrews, L.; Zhou, M.; Willson, S. P.; Kushto, G. P.; Snis, A.; Panas, I., Infrared Spectra of Cis and Trans $(NO)_2^-$ Anions in Solid Argon. *J. Chem. Phys.* **1998,** *109* (1), 177-185.

15. Lugez, C. L.; Thompson, W. E.; Jacox, M. E.; Snis, A.; Panas, I., Infrared Spectra of NO_2^+ NO_2^- and NO_3^- Trapped in Solid Neon. *J. Chem. Phys.* **1999,** *110* (21), 10345-10358.

16. Andrews, L.; Zhou, M., Infrared Spectra of NO_2^- and NO_2^+ Isomers Trapped in Solid Neon. *J. Chem. Phys.* **1999,** *111* (13), 6036-6041.

17. Thompson, M. C.; Weber, J. M., Infrared Spectroscopic Studies on the Cluster Size Dependence of Charge Carrier Structure in Nitrous Oxide Cluster Anions. *J. Chem. Phys.* **2016,** *144*, 104302.

18. Fuster, F.; Dezarnaud-Dadine, C.; Chevreau, H.; Sevin, A., A Theoretical Study of the Bonding in NO NO_2 NO_2^- and NO_2^{2-} using a Topological Analysis of the Electron Localization Function. *Phys. Chem. Chem. Phys.* **2004,** *6*, 3228-3234.

19. Zakharov, I. I.; Anufrienko, V. F.; Zakharova, O. I.; Yashnik, S. A.; Ismaguilov, Z. R., Ab Initio Calculation of Nitrogen Oxide Dimer Structure and its Anion Radical. *J. Struc. Chem.* **2005,** *46* (2), 213-219.

20. Demyanenko, A. V.; Potter, A. B.; Dribinski, V.; Reisler, H., NO Angular Distributions in the Photodissociation of $(NO)_2$ at 213 nm: Deviations from Axial Recoil. *J. Chem. Phys.* **2002,** *117* (6), 2568-2577.

21. Potter, A. B.; Dribinski, V.; Demyanenko, A. V.; Reisler, H., Exit Channel Dynamics in the Ultraviolet Photodissociation of the NO dimer: $(NO)_2$ --> $NO(A^2\sum^+)$ + $NO(x^2\Pi)$. *J. Chem. Phys.* **2003,** *119* (14), 7197-7205.

22. Maricq, M. M.; Tanguay, N. A.; O'Brien, J. C.; Rodday, S., M.; Rinden, E., Vibrational Autodetachment of NO^-. *J. Chem. Phys.* **1988,** *90* (6), 3136-3144.

23. Travers, M. J.; Cowles, D. C.; Ellison, G. B., Reinvestigation of the Electron Affinities of O_2 and NO. *Chem. Phys. Lett.* **1989,** *164* (5).

24. Velarde, L.; Habteyes, T.; Grumbling, E. R.; Pichugin, K.; Sanov, A., Solvent Resonance Effect on the Anisotropy of $NO^-(N_2O)_n$ Cluster Anion Photodetachment. *J. Chem. Phys.* **2007,** *127*, 084302.

25. Randell, J.; Lunt, S. L.; Mrotzek, G.; Field, D.; Ziesel, J. P., Low-Energy Negative-Ion States of NO at High Electron Energy Resolution. *Chem. Phys. Lett.* **1996,** *252*, 253-257.

26. Senn, G.; Muigg, D.; Denifl, G.; Stamatovic, A.; Scheier, P.; Mark, T. D., Electron Attachment to Nitric Oxide Clusters and Electron Impact Ionization of Carbon Monoxide Clusters. *Eur. Phys. J. D.* **1999,** *9*, 159-162.

27. Spence, D.; Schulz, G. J., Vibrational Excitation and Compound States in NO. *Physical Review A* **1971,** *3* (6).

28. Zecca, A.; Lazzizzera, I.; Krauss, M.; Kuyatt, C. E., Electron Scattering from NO and N_2O below 10 eV. *J. Chem. Phys.* **1974,** *61* (11), 4560-4566.

29. Chu, Y.; Senn, G.; Matejcik, S.; Scheier, P.; Stampfli, P.; Stamatovic, A.; Illenberger, E.; Mark, T. D., Formation of NO^- Following Electron Attachment to NO Clusters. *Chem. Phys. Lett.* **1998,** *289*, 521-526.

30. Otto, R.; Ray, A. W.; Daluz, J. S.; Continetti, R. E., Direct IR Excitation in a Fast Ion Beam: Application to NO^- Photodetachment Cross Sections. *EPJT* **2014,** *1*, 3.

31. Shen, B.; Benitez, Y.; Lunny, K. G.; Continetti, R. E., Internal Energy Dependence of the Photodissociation Dynamics of O_3^- Using Cryogenic Photoelectron-Photofragment Coincidence Spectroscopy. *J. Chem. Phys.* **2017,** *147*, 094307.

32. Dixon, A.; Xue, T.; Sanov, A., Spectroscopy of Ethylenedione. *Angew. Chem. Int. Ed.* **2015,** *54* (127), 8764-8767.

33. Johnson, C. J.; Shen, B. B.; Poad, B. L. J.; Continetti, R. E., Photoelectron-Photofragment Coincidence Spectroscopy in a Cryogenically Cooled Linear Electrostatic Ion Beam Trap. *Rev. Sci. Instrum.* **2011,** *82*, 105105.

34. Shen, B. B.; Lunny, K. G.; Benitez, Y.; Continetti, R. E., Photoelectron-Photofragment Coincidence Spectroscopy with Ions Prepared in a Cryogenic Octopole Accumulation Trap: Collisional Excitation and Buffer Gas Cooling. *Front. Chem.* **2019,** *7*, 295.

35. Wiley, W. C.; McLaren, I. H., Time-of-Flight Mass Spectrometer with Improved Resolution. *Rev. Sci. Instrum.* **1955,** *26*, 1150-1157.

36. Poad, B. L. J.; Johnson, C. J.; Continetti, R. E., Photoelectron-Photofragment Coincidence Studies of NO^--X clusters (X = H_2O, CD_4). *Faraday Discussions* **2011,** (150).

37. Zajfman, D.; Rudich, Y.; Sagi, I.; Strasser, D.; Savin, D. W.; Goldberg, S.; Rappaport, M.; Heber, O., High Resolution Mass Spectrometry Using a Linear Electrostatic Ion Beam Trap. *Int. J. Mass. Spectrom.* **2003,** *229*, 55-60.

38. Lunny, K. G.; Benitez, Y.; Albeck, Y.; Strasser, D.; Stanton, J. F.; Continetti, R. E., Spectroscopy of Ethylenedione and Ethynediolide: A Reinvestigation. *Angew. Chem. Int. Ed.* **2018,** *57* (18), 5394-5397.

39. Arrington, C. A.; Dunning, T. H.; Woon, D. E., Electron Affinity of NO. *J. Phys. Chem. A* **2007,** *111*, 11185-11188.

40. Barlow, S. E.; Bierbaum, V. M., Reactions of O^-+ N_2O at 300 K: The Totally Labeled Experiments. *J. Chem. Phys.* **1990,** *92*, 3448.

41. Siegel, M. W.; Celotta, R. J.; Hall, J. L.; Levine, J.; Bennett, R. A., Molecular Photodetachment Spectrometry. I. The Electron Affinity of Nitric Oxide and the Molecular Constants of NO-. *Phys. Rev. A* **1972,** *6* (2), 607-631.

42. Johns, J. W. C.; Reid, J., The Vibration-Rotation Fundamental of NO. *J. Mol. Spec.* **1977,** *65*, 155-162.

43. Busch, G., E.; Wilson, K. R., Triatomic photofragmet spectra I. Energy Partitioning in NO_2 Photodissociation. *J. Chem. Phys.* **1972,** *56* (7), 3626-3638.

44. Trentelman, K. A.; Kable, S. H.; Moss, D. B.; Houston, P. L., Photodissociation Dynamics of Acetone at 193 nm: Photofragment Internal and Translational Energy Distributions. *J. Chem. Phys.* **1989,** (91), 7498.

45. Eggers, D. F.; Crawford, B. L., Vibrational Intensities. III. Carbon Dioxide and Nitrous Oxide. *J. Chem. Phys.* **1951,** *19* (12), 1554-1561.

46. Chou, J. Z.; Hewitt, S. A.; Hershberger, J. F.; Flynn, G. W., Diode Laser Probing of the Low Frequency Vibrational Modes of Baths of CO_2 and N_2O Excited by Relaxation of Highly Excited NO_2. *J. Chem. Phys.* **1990,** *93* (12), 8474-8481.

47. Ervin, K. M.; Ho, J.; Lineberger, W. C., Ultraviolet Photoelectron Spectrum of NO_2^-. *J. Phys. Chem.* **1988,** *92*, 5405-5412.

Chapter 7: Photodissociation of the Peroxynitrite Anion

7.1. Introduction

NO_3 is an atmospherically relevant system that has been studied extensively both experimentally and theoretically.[1-15] It plays an important role in acid precipitation in the stratosphere and troposphere and is produced in the reaction of NO_2 with ozone.[16] Because NO_3 can be photolyzed by sunlight, it is the dominant oxidant found in the atmosphere at night.[7] Due to this significant importance in the atmosphere, the NO_3 system has been studied using a variety of methods, including photodissociation experiments, as well as photoelectron spectroscopy.[6, 10] These have revealed a system with many photodissociation pathways, as well as low lying electronic states on both the anion and the neutral surfaces.[6, 11, 13, 14] Photoelectron-photofragment coincidence spectroscopy is able to combine these techniques in order to correlate photodissociation products with photodetached electrons, providing insight into the vibrational excitation partitioning within the system.

Multiple studies have been conducted on the neutral NO_3 surface, including fluorescence studies,[1-3] cavity ringdown spectroscopy,[4, 5] photodissociation experiments,[6] and photoelectron spectroscopy of the NO_3^- anion.[10] Using photofragmentation translational spectroscopy, two photodissociation channels of neutral NO_3 were observed.[6] These were determined to be photodissociation to NO_2 + O and NO + O_2. While a significant barrier to dissociation was predicted, The NO ($^2\Pi$) + O_2 ($^3\Sigma^-_g$) was determined to be only ~0.11 eV above NO3 ($^2A_2$').[6] While many theoretical studies have been conducted on the NO_3 system, there remains debate about the multiple low-lying electronic states on the neutral surface.[7,8,9] The $^2A_2$' ground state, as well as the ^2E'' and ^2E' excited

states have been observed though photoelectron spectroscopy with an adiabatic electron affinity (AEA) of 3.937 eV.[10] Photodetachment of the D_{3h} anion allowed for the first observation of the $^2E''$ state, as this is a forbidden transition for optical excitation from the ground state neutral.[10]

While multiple theoretical and experimental studies have been carried out on neutral NO_3, less is known about the anion surface. Theoretical simulations of the observed vibrational spectra allowed isolation of three distinct isomers, the D_{3h} isomer, a cis isomer and a trans isomer.[11] The peroxynitrite cis/trans anions are high energy isomers that are known to have biological relevance.[13, 14] These anions are formed through reactions with hydrogen peroxide and nitrite.[17] Infrared spectra of the cis and trans peroxynitrite anion have been reported with calculated structures.[18] The peroxynitrite anion has been studied more extensively in liquid phase and is stable in basic solutions. In biological systems, peroxynitrite can interfere with the role of lipids, DNA and proteins. This can cause major damage in cells, leading to strokes and heart failure.[17] Because of these significant impacts, it is important to understand the overall reactions and dissociation dynamics that of this system.

Photoelectron-photofragment coincidence (PPC) spectroscopy provides an approach to studying stable molecular anions using photoelectron spectroscopy and photofragment translational spectroscopy in coincidence, providing insight into the electron detachment and fragmentation dynamics of the neutral products. The addition of a cryogenic octopole accumulation trap has increased the variety of anions that can be stabilized, allowing for high energy species such as the peroxynitrite anion to be studied.[19] Photodissociation of the peroxynitrite anion has resulted in the observation of two distinct

channels: $NO^-(^3\Sigma^-, v>0)$ + $O_2(^3\Sigma_g^-)$ and $NO(^2\Pi)$ + $O_2^-(^2\Pi_g)$, followed by sequential photodetachment of O_2^- . Both of these channels were observed with vibrationally excited products. By measuring both the electron kinetic energy (eKE) as well as the kinetic energy release (KER) of the neutrals, the levels of vibrational excitation induced in the NO- and O2- photoproducts can qualitatively be assigned.

7.2. Experimental Methods

Anions were generated using neat N_2O as a carrier gas for dried glyoxal (heated to 45˚ C). The glyoxal was dried for 18 hours at 4˚ C with 3 Å molecular sieves in a 1:1 ratio. Ions are formed by a pulsed supersonic expansion at 10 Hz being crossed with a 1 keV electron beam. Significant structural rearrangement of the glyoxal precursor resulted in the formation of a range of molecular anions and clusters, including nitrogen oxides.[20] The ions were then extracted with a Wiley-McLaren time of flight spectrometer. The pulsed value is mounted on a vertically adjustable mount, allowing for the distance of the pulsed valve to the Wiley-McLaren plates to be adjusted. By decreasing this distance, less time is given for collisional cooling and high energy isomers are produced. These high energy species can then be stabilized in a cryogenic octopole accumulation trap (COAT). The ions are collisionally cooled for 40 ms at 18k with 80:20 He/H_2 buffer gas. Once extracted from COAT, the ion packet is accelerated to 7 keV before being re-referenced to ground with a potential switch. The packet is then separated by time-of-flight and injected into a cryogenic electrostatic ion beam trap (EIBT).

Once inside the EIBT, different masses are separated based on their oscillation frequency within the trap.[21] This is a more sensitive separation and allows for masses with

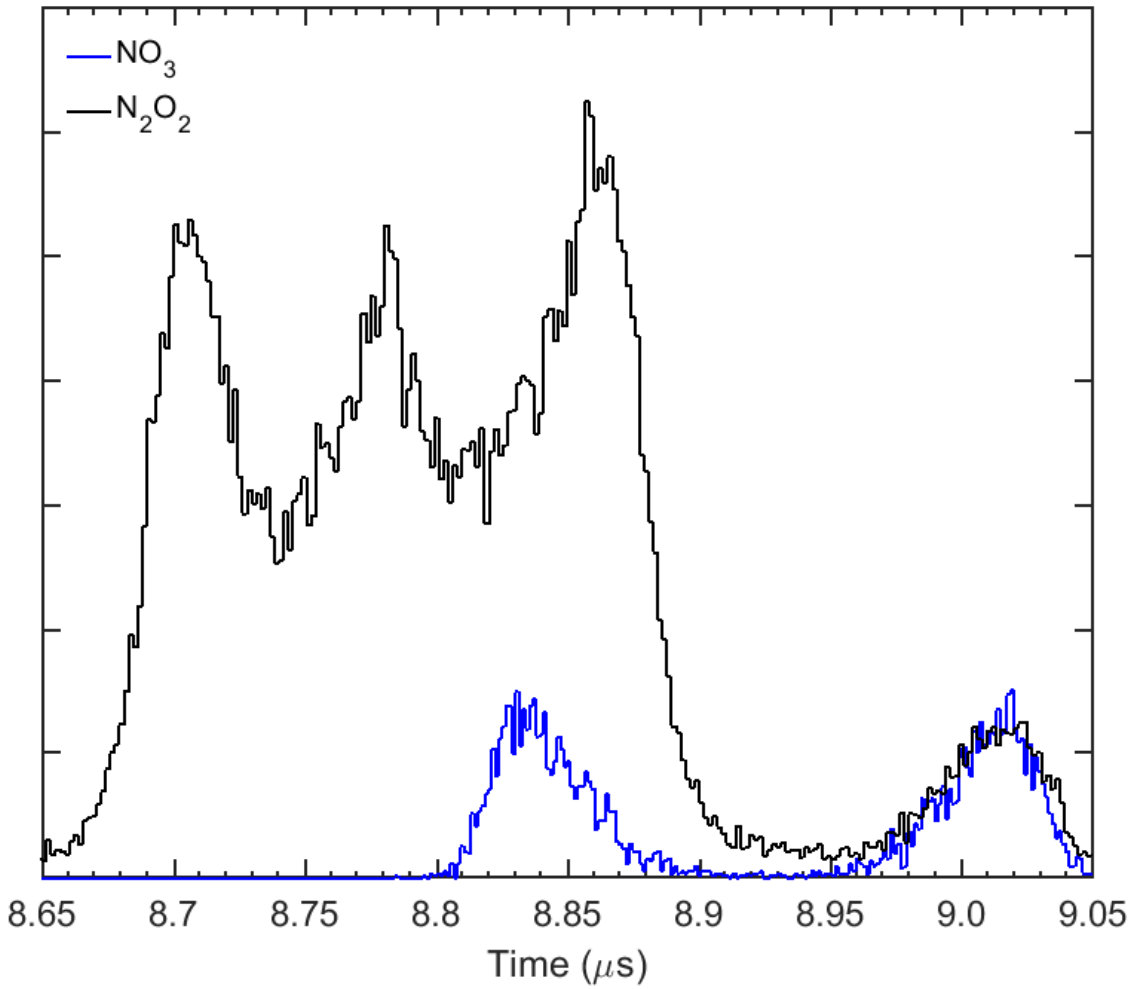

Figure 7.1. The time of arrival on the neutral detector. Multiple masses were collected, including 62 amu, seen in blue, which is discussed in this chapter. The data at 60 amu can also be seen in black, and has been expanded upon in a previous chapter.

as little as 1 amu difference to be collected simultaneously and resolved in the analysis. Within the EIBT the packet is interrogated with a 3.20 eV, 1037 Hz picosecond pulsed Ti:Sapphire regenerative amplifier (Clark-MXR CPA 2000, 1.2 ps, 400 μJ/pulse). Velocity map imaging is employed orthogonal to the ion beam to focus the photoelectrons on a time and position sensitive detector. The electron detector was calibrated with O_2^- and has a resolution of ΔeKE/eKE 4%. The resulting neutral products, which continue along the ion beam path, are collected on a multi-particle time and position sensitive detector 1.31 m from the interaction region. The neutral detector was calibrated with O_4^- and ΔKER/KER was found to be 10%.

7.3. Results and Discussion

Figure 7.1 shows the neutral product time-of-arrival distributions. The data at 62 amu, in blue, displays fully-resolved forward and backward scattered components centered at 8.84 and 9.02 μs, around the nominal time-of-arrival of the center of mass of the system at 8.93 μs. This is due to the photofragment recoil velocities in the center-of-mass frame, and shows that the data at 62 amu has a large kinetic energy release. For 62 amu, the fragments that arrive earlier are imbedded in the 60 amu data. By finding the center of mass for dissociation of both the 60 amu anion ($N_2O_2^-$) and the 62 amu anion (NO_3^-), this time-of-arrival peaks can be resolved by extracting the momentum-matched events from the data set. The photoelectron spectrum for NO_3^- is shown in Figure 7.2. The effective laser fluence was changed from $2x10^{11}$ W/cm^2 to $2x10^9$ W/cm^2 in order to differentiate one photon and two photon events, which can be seen in the two traces. From this, it was determined that the signal spanning the energy range of 1-3 eV was a two-photon process, while the signal below 1 eV was a one-photon process. Momentum partitioning in both of

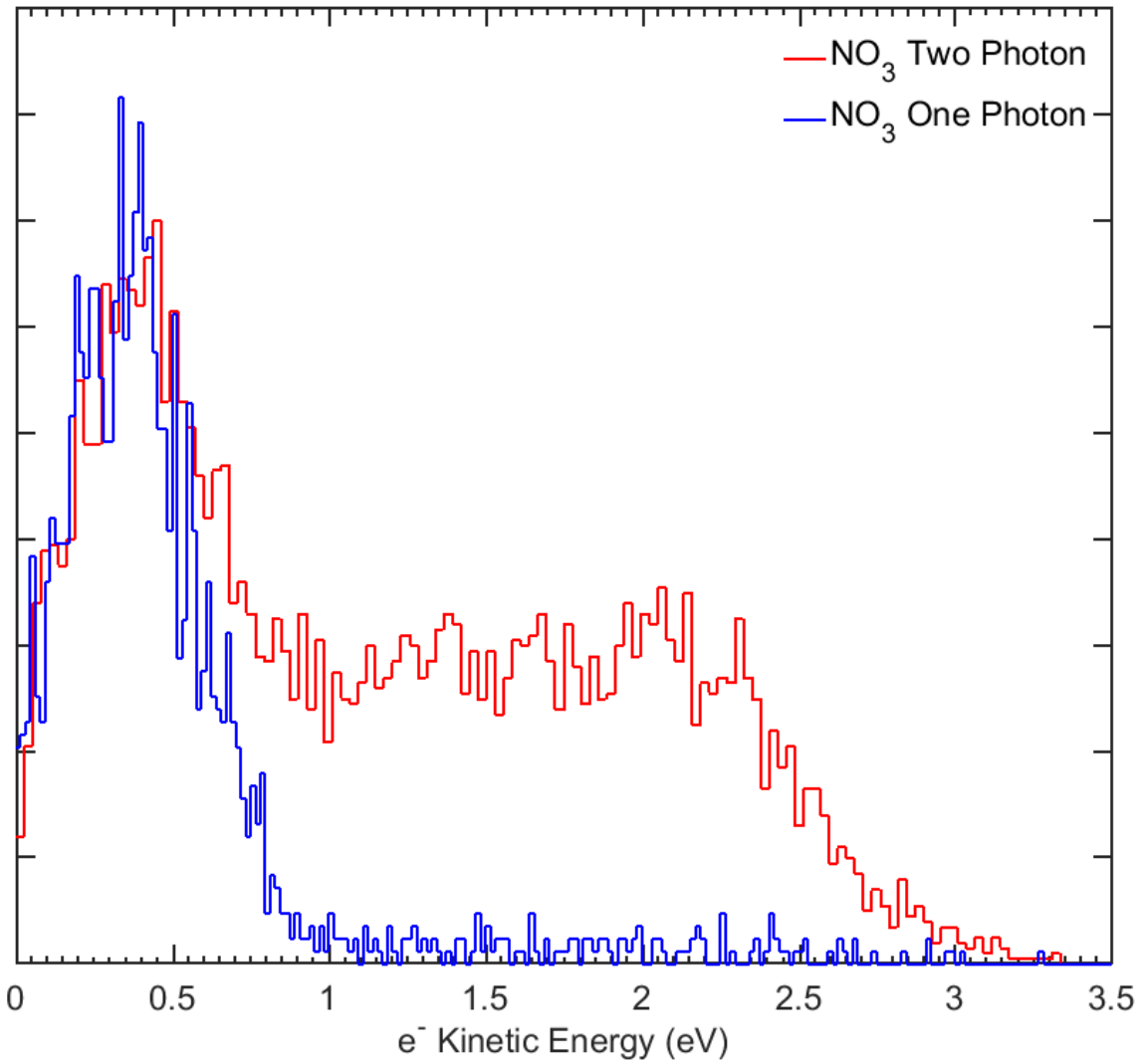

Figure 7.2. The photoelectron spectra for NO_3^- comparing the effective laser fluence. The channel observed to span 1-3 eV is shown to be the result of a two-photon process.

these channels were found to be consistent with a nearly symmetric dissociation, indicating that the dissociation channels being accessed ultimately produced neutral O_2 + NO. The two low-lying ionic photodissociation pathways that would be consistent with this was found to be the photodissociation of $NO^-(^3\Sigma^-) + O_2(^3\Sigma_g^-)$ with vibrationally excited NO anions undergoing autodetachment, and photodissociation of $NO(^2\Pi) + O_2^-(^2\Pi_g)$, followed by sequential photodetachment of O_2^- via a two-photon process.

7.3.1. Photodissociation and Autodetachment

The autodetachment of NO^- has been observed and discussed in the context of the mass 60 data, where $N_2O_2^-$ undergoes photodissociation to NO + NO^- in Chapter 6 of this thesis. Due to the small electron affinity of NO^- (0.026 eV), vibrationally excited anions undergo spontaneous electron ejection to reach the neutral surface.[22, 23] For $N_2O_2^-$, the first three vibrational states of NO^- were observed at the highest intensity, and correlate well with the low electron kinetic energy from this data. In $N_2O_2^-$, the ν=1 of NO^- is heavily favored over ν=2,3, while for NO_3^- photodissociation, ν=3 has the highest contribution. Above ν=4, a combination of anion electronic states results in less resolved transitions.[23,24]

The cis structure of the peroxynitrite anion has been calculated to have a NO bond length of 1.22 Å, while the $N_2O_2^-$ anion is calculated to have a bond length of 1.265 Å.[11, 25] Because the peroxynitrite anion has a significantly larger geometry change to reach the NO^- anion bond length of 1.271 Å, more excitation is expected in the dissociative products.[22, 26] The O_2 bond length in cis NO_3^- has been calculated to be 1.38 Å, which is also a significant geometry change to the 1.2075 Å equilibrium bond length of ground state neutral O_2.[11, 27] This geometry change indicates that vibrational excitation could be favored

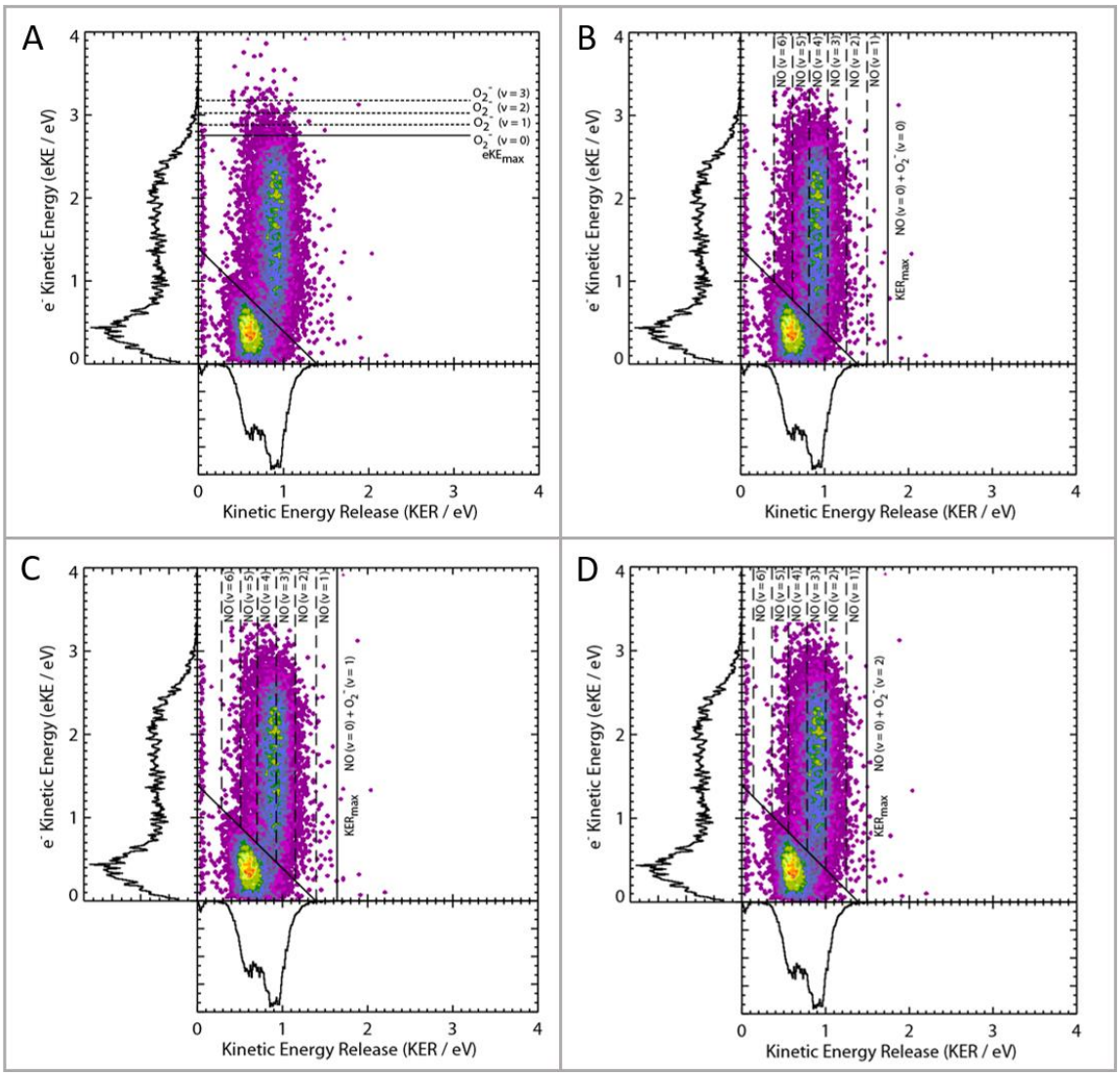

Figure 7.3. The coincidence spectrum for NO_3^- photodissociation. Panel A: The eKE_{max} for each vibrational state of O_2^- is shown, as well as the KE_{max} for the autodetachment channel. Panel B-D: The vibrational states of NO are overplotted with the data in order to show the possible energy partitioning. Each panel shows energy partitioned into O_2^- v=0-2, and the corresponding NO neutral energetics, respectively.

in the either fragment. The photodissociation of NO^- ($^3\Sigma^-$) + O_2 ($^3\Sigma_g^-$), followed by autodetachment of vibrationally excited NO anions is assigned to the low eKE signal, and can be seen in the coincidence spectrum in Figure 7.3 below the diagonal KE_{max} annotation.

The assignment of these states is further complicated that the separation between the cis and trans isomers of the NO_3^- anion have a similar energy separation to vibrations in both neutral O_2 and NO. In the present case we have assigned this photodissociation /autodetachment pathway to the more stable cis isomer. As mentioned previously, the geometry change of the O_2 bond length resulting from this photodissociation channel could favor excitation. It is unclear from the present study if vibrational excitation is partitioned into the O_2 neutral fragment, but more likely than the formation of the trans isomer due to the use of the cryogenic octopole accumulation trap.

The kinetic energy maximum (KE_{max}) for this channel was observed to be 1.4 eV. This is in excellent agreement with the relative energies of the cis isomer of the NO_3^- anion and the NO($^2\Pi$) + O_2($^3\Sigma_g^-$) photodissociation channel, as seen in Figure 7.4. If this photodissociation resulted in $NO^-(v=0)$ + O_2, a two photon process would be required for sequential photodetachment of the NO anion. While it is possible that the NO_3^- photodissociation would result in NO anions in their ground vibrational state, it is unlikely due to the large geometry change between the NO_3^- anion and NO^- anion bond length. The photodissociation of NO_3^- resulted in the population of higher vibrational states of NO^- as compared to the photodissociation of $N_2O_2^-$, due to the larger geometry change. In $N_2O_2^-$, photodissociation to $NO^-(v=0)$ was weakly favored as compared to $NO^-(v>0)$. Because the autodetachment of the lower vibrational states of $NO^-(v=1,2)$ is observed in lower intensity in the photodissociation of NO_3^-, it would be expected that $NO^-(v=0)$ would also be

suppressed. The higher energy, two-photon signal spans the same energy regime as the photodetachment of $NO^-(v=0)$, so it is unclear, but unlikely that this mechanism is occurring. However, photodissociation to $NO^-(v=0)$ followed by sequential photodetachment cannot be ruled out. As a result, the first channel observed is assigned to photodissociation of cis $NO_3^- \rightarrow NO^- (^3\Sigma^-) + O_2 (^3\Sigma_g^-)$, followed by autodetachment of the NO^- anion.

7.3.2 Photodissociation and Sequential Photodetachment

The second nearly symmetric dissociation observed is seen at higher eKE in the coincidence spectrum as shown in Figure 7.3. The signal from 1-3 eV in the photoelectron spectrum is observed to have a significant Kinetic Energy Release (KER), with a strong horizontal KER_{max} and KER_{min}, an indication of a two-photon process. The photoelectron spectrum for this signal spans the same energy range as free O_2^- photodetachment, but due to low signal, the multiple vibrational and electronic transitions usually observed are not seen here.[28] When a system undergoes photodissociation followed by sequential photodetachment of one of the resulting anion fragments, the eKE and KER are decoupled, resulting in horizontal and vertical features in a coincidence plot, rather than the diagonal energy limits that are seen in dissociative photodetachment. Because of this, the KER_{max} that is observed is a direct measure of the dissociation energy of the anion and is in excellent agreement with the energetic separation of the cis NO_3^- isomer and vibrationally excited NO $(^2\Pi) + O_2^- (^2\Pi_g)$ product channel.

Vibrational excitation in both products was considered. The change in geometry from the cis NO_3^- anion to the NO neutral bond length is 1.22 Å to 1.151 Å.[11, 29] It is also

possible that the O_2^- (v=1,2) is populated due to the geometry change between cis NO_3^- and O_2^-, (1.38 Å vs 1.348 Å, respectively).[11, 27] The different eKE_{max} can be seen in Figure 7.3(a) for each of the vibrational states of O_2^- that could be populated. The low electron affinity of O_2^- (0.448 eV) as compared to the vibrational excitation indicates that higher excited states are not stable.[27] Autodetachment will occur at vibrational states higher than v=4, so if these are populated, they are not contributing to the photodissociation channel.[30-32] These eKE_{max} indicate that O_2^- (v=0,1) are the most favored with some O_2^- (v=2) possibly observed. However, it was determined that the NO neutral vibrations accounted for more of the energy discrepancy from the $NO(^2\Pi, v=0) + O_2(^3\Sigma_g^-, v=0)$ KER_{max} than the O_2^- vibrations.

Given the well-known vibrational spacing on the NO neutral surface, as seen in Figure 7.4, the energy partitioning could be compared for each of these channels. Figure 7.3(b-d) show the potential NO vibrational transitions overlaid on the coincidence spectrum for each of the O_2^- (v=0,1,2) vibrations. A clear KER_{min} is also observed, indicating the highest vibrational modes populated. For O_2^-, a single vibration has been observed to be ~0.13 eV, while NO vibrational states are ~0.26 eV, indicating that transitions of O_2^- (v=0) and O_2^- (v=2) would have very similar experimental KER_{max} and KER_{min}.[26, 27] Figure 7.3(b) and Figure 7.3(d), show the possible NO vibrations populated for each of the respective O_2^- vibrations. More vibrational excitation in O_2^- would result in lower NO vibrational states populated, which would not be expected given the significant geometry change induced by the shortening of the NO bond following photodissociation. Due to this, as well as the lack of population of O_2^- (v=2) in the eKE_{max}, it is assumed that the ground state O_2^- is more favored in this photodissociation channel. When O_2^- is in its

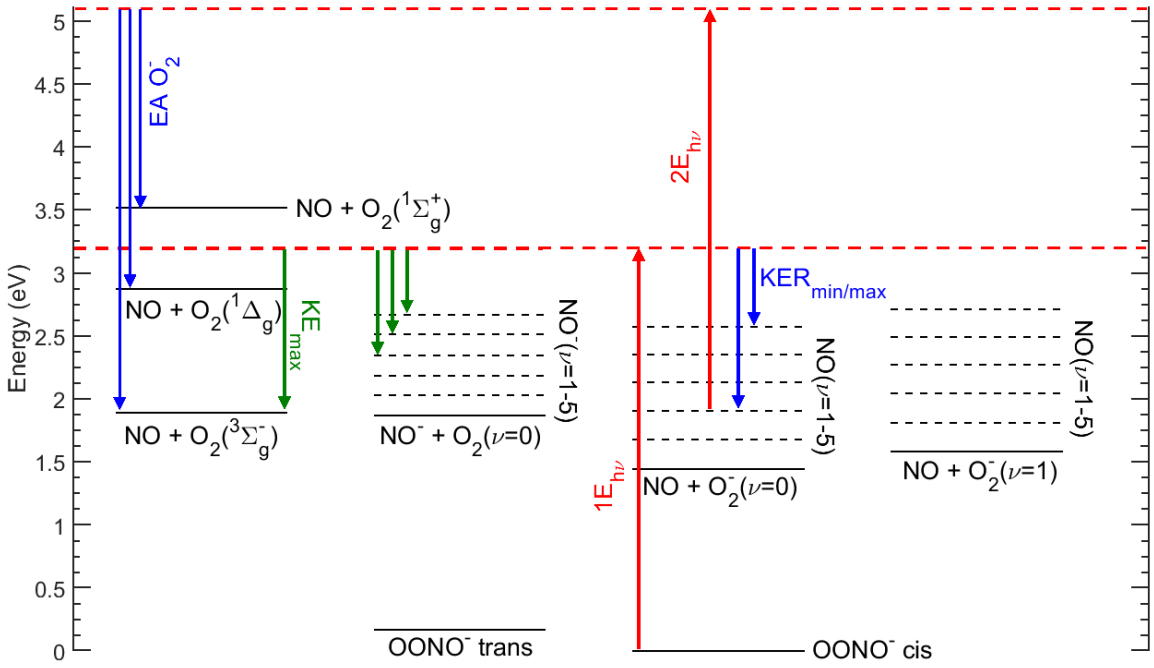

Figure 7.4. The relative energetics of the NO_3 system. The vibrational spacing for both NO^- and O_2^- are shown, as well as the corresponding neutral product energies, which have been previously reported.[6, 10, 22, 26, 27] The isomers of the peroxynitrite anion were calculated in relation to the D_{3h} isomer (not shown).

ground vibrational state, NO (ν=2-5) would be populated in the energy span observed, as seen in Figure 7.3(b). If the O_2^- (ν=1) is populated, the NO neutral states ν=2-4 would have be observed, which can be seen in Figure 7.3(c). Due to the limited resolution of the experiment, it cannot be ruled out that a combination of these transitions is most likely. As a result, the second channel observed is assigned to photodissociation of cis NO_3^- → $NO(^2\Pi)$ + $O_2^-(^2\Pi_g)$ with sequential photodetachment of O_2^- to the three low-lying electronic states of O_2 neutral.

7.4. Conclusion

The first observation of the photodissociation of peroxynitrite anion is in excellent agreement with theoretical predictions for vibrationally excited products, as well as the known dissociation states of the anion and neutral system. The observation of two distinct dissociation channels from the cis peroxynitrite isomer adds to the overall understanding of this high-energy isomer to the energetics of this system. These results prove that the implementation of the cryogenic octopole accumulation trap has not only allowed for anions to be studied in their ground vibrational state, but has also contributed to stabilizing exotic anion isomers that have not been favored previously.

Chapter seven is being prepared for publication, in which the dissertation author is the primary author and the dissertation advisor is the corresponding author. Lunny, K. G., Albeck, Y., Benitez, Y., Strasser, D., Stanton, J. F., Continetti, R. E., "Photodissociation of the Peroxynitrite Anion"

7.5. References

1. Nelson, H. H.; Pasternack, L.; McDonald, J. R., Laser-Induced Excitation and Emission Spectra of NO_3. *J. Phys. Chem.* **1983,** *87*, 1286-1288.

2. Ishiwata, T.; Fujiwara, I.; Naruge, Y.; Obi, K.; Tanaka, I., Study of NO_3 by Laser-Induced Fluorescence. *J. Phys. Chem.* **1983,** *87*, 1349-1352.

3. Kim, B.; Hunter, P. L.; Johnston, H. S., NO_3 Radical Studied by Laser-Induced Fluorescence. *J. Chem. Phys.* **1992,** *96*, 4057.

4. Deev, A.; Sommar, J.; Okumura, M., Cavity Ringdown Spectrum of the Forbidden A^2E'' <-- X^2A_2' Transition of NO_3: Evidence for Static Jahn-Teller Distortion in the A State. *J. Chem. Phys.* **2005,** *122*, 224305.

5. Okumura, M.; Stanton, J. F.; Deev, A.; Sommar, J., New Insights into the Jahn-Teller Effect in NO_3 Via the Dark A^2E'' State. *Phys. Scr.* **2006,** *73*, C64-C70.

6. David, H. F.; Kim, B.; Johnston, H. S.; T., L. Y., Dissociation Energy and Photochemistry of NO_3. *J. Phys. Chem.* **1993,** *97*, 2172-2180.

7. Stanton, J. F., On the Vibronic Level Structure in the NO_3 Radical. I. The Ground Electronic State. *J. Chem. Phys.* **2007,** *126*, 134309.

8. Stanton, J. F., On the Vibronic Level Structure in the NO_3 Radical: II. Adiabatic Calculation of the Infrared Spectrum. *Mol. Phys.* **2009,** *107*, 1059-1075.

9. Stanton, J. F.; Okumura, M., On the Vibronic Level Structure in the NO_3 Radical: III. *Phys. Chem. Chem. Phys.* **2009,** *11*, 4742-4744.

10. Weaver, A.; Arnold, D. W.; Bradforth, S. E.; M., N. D., Examination of the $^2A_2'$ and $^2E'$ states of NO_3 by Ultraviolet Photoelectron Spectroscopy of NO_3^-. *J. Chem. Phys.* **1991,** *94* (3), 1740-1751.

11. Relph, R. A.; Bopp, J. C.; Johnson, M. A.; Viggiano, A. A., Argon Cluster-Mediated Isolation and Vibrational Spectra of Peroxy and Nominally D_{3h} Isomers of CO_3^- and NO_3^-. *J. Chem. Phys.* **2008,** *129*, 064305.

12. Lugez, C. L.; Thompson, W. E.; Jacox, M. E.; Snis, A.; Panas, I., Infrared Spectra of NO_2^+ NO_2^- and NO_3^- Trapped in Solid Neon. *J. Chem. Phys.* **1999,** *110* (21), 10345-10358.

13. Tsai, J.-H. M.; Harrison, J., G.; Martin, J. C.; Hamilton, T. P.; Woerd, M. v. d.; Jablonsky, M. J.; Beckman, J. S., Role of Conformation of Peroxynitrite Anion ($ONOO^-$) in Its Stability and Toxicity. *J. Am. Chem. Soc.* **1994,** *116*, 4115-4116.

14. Tsai, H.-H.; Hamilton, T. P.; Tsai, J.-H. M.; Woerd, M. v. d.; Harrison, J. G.; Jablonsky, M. J.; Beckman, J. S.; Koppenol, W. H., Ab Initio and NMR Study of Peroxynitrite and Peroxynitrous Acid: Important Biological Oxidants. *J. Phys. Chem.* **1996,** *100*, 15087-15095.

15. Liang, B.; Andrews, L., Infrared Spectra of cis- and trans-Peroxynitrite Anion, $OONO^-$, in Solid Argon. *J. Am. Chem. Soc.* **2001,** *123*, 9848-9854.

16. Schwartz, S. E., Acid Deposition: Unraveling a Regional Phenomenon. *Science* **1989,** *243* (4892), 753-763.

17. Pacher, P.; Beckman, J. S.; Liaudet, L., Nitric Oxide and Peroxynitrite in Health and Disease. *Physiol. Rev.* **2007,** *81* (1), 315-424.

18. Andrews, L.; Zhou, M.; Willson, S. P.; Kushto, G. P.; Snis, A.; Panas, I., Infrared Spectra of Cis and Trans $(NO)_2^-$ Anions in Solid Argon. *J. Chem. Phys.* **1998,** *109* (1), 177-185.

19. Shen, B. B.; Lunny, K. G.; Benitez, Y.; Continetti, R. E., Photoelectron-Photofragment Coincidence Spectroscopy with Ions Prepared in a Cryogenic Octopole Accumulation Trap: Collisional Excitation and Buffer Gas Cooling. *Front. Chem.* **2019,** *7*, 295.

20. Shen, B.; Benitez, Y.; Lunny, K. G.; Continetti, R. E., Internal Energy Dependence of the Photodissociation Dynamics of O_3^- Using Cryogenic Photoelectron-Photofragment Coincidence Spectroscopy. *J. Chem. Phys.* **2017,** *147*, 094307.

21. Poad, B. L. J.; Johnson, C. J.; Continetti, R. E., Photoelectron-Photofragment Coincidence Studies of NO^--X clusters (X = H_2O, CD_4). *Faraday Discussions* **2011,** *150*, 481-492.

22. Maricq, M. M.; Tanguay, N. A.; O'Brien, J. C.; Rodday, S., M.; Rinden, E., Vibrational Autodetachment of NO^-. *J. Chem. Phys.* **1988,** *90* (6), 3136-3144.

23. Spence, D.; Schulz, G. J., Vibrational Excitation and Compound States in NO. *Physical Review A* **1971,** *3* (6).

24. Randell, J.; Lunt, S. L.; Mrotzek, G.; Field, D.; Ziesel, J. P., Low-Energy Negative-Ion States of NO at High Electron Energy Resolution. *Chem. Phys. Lett.* **1996,** *252*, 253-257.

25. Snis, A.; Panas, I., N_2O_2, $N_2O_2^-$ and $N_2O_2^{2-}$: Structures, Energetics and N-N Bonding. *Chem. Phys.* **1997,** *221*, 1-10.

26. Travers, M. J.; Cowles, D. C.; Ellison, G. B., Reinvestigation of the Electron Affinities of O_2 and NO. *Chem. Phys. Lett.* **1989,** *164* (5).

27. Ervin, K. M.; Anusiewicz, I.; Skurski, P.; Simmons, J.; Lineberger, W. C., The Only Stable State of O_2^- Is the $X^2\Pi_g$ Ground State and It (Still!) Has an Adiabatic Electron Detachment Energy of 0.45 eV. *J. Phys. Chem. A* **2003,** *107*, 8521-8529.

28. Ervin, K. M.; Ho, J.; Lineberger, W. C., Ultraviolet Photoelectron Spectrum of NO_2^-. *J. Phys. Chem.* **1988,** *92*, 5405-5412.

29. Sette, F.; Stohr, J.; Hitchcock, A. P., Determination of Intramolecular Bond Lengths in Gas Phase Molecules from K Shell Shape Resonances. *J. Chem. Phys.* **1984,** *81*, 4906.

30. Boesl, U.; BaBmann, C.; Kasmeier, R., Time-of-Flight Mass Analyzer for Anion Mass Spectrometry and Anion Photoelectron Spectroscopy. *Int. J. Mass. Spec.* **2000,** *206*, 231-244.

31. Schiedt, J.; Weinkauf, R., Spin-Orbit Coupling in the O_2^- Anion. *Z. Naturforsch.* **1995,** *50a*, 1041-1044.

32. Corderman, R. R.; Engelking, P. C.; Lineberger, W. C., Laser Photoelectron Spectroscopy Measurement of Characteristic Electronic and Vibrational Temperatures of Sputtered Negative Ions. *Appl. Phys. Lett.* **1980,** *36* (7), 533-535.